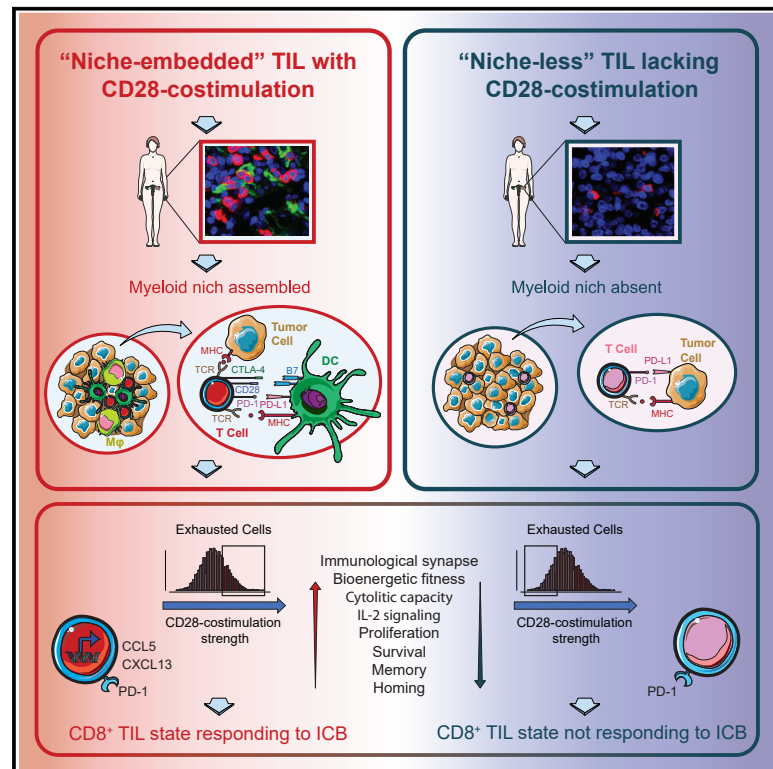


# Cancer Cell

## Myeloid antigen-presenting cell niches sustain antitumor T cells and license PD-1 blockade via CD28 costimulation

### Graphical abstract



### Authors

Jaikumar Duraiswamy,  
Riccardo Turrini, Aspram Minasyan, ...,  
Marie-Agnès Doucey,  
Denarda Dangaj Laniti, George Coukos

### Correspondence

george.coukos@chuv.ch

### In brief

Duraiswamy et al. characterize tumor-specific CD8<sup>+</sup> lymphocytes infiltrating high-grade serous epithelial ovarian cancer and note their close association with intraepithelial myeloid APC niches *in situ*. Intraepithelial myeloid APC niches support tumor-infiltrating lymphocytes with CD28 costimulation *in situ*, sustaining antitumor immune attack and enabling response to PD-1 blockade.

### Highlights

- Ovarian islets are enriched in activated tumor-specific lymphocytes
- Intraepithelial myeloid APC niches harbor polyfunctional TIL with increased fitness
- TIL activation on  $\alpha$ PD-1 depends on CD28 costimulation catered by myeloid APCs *in situ*
- $\alpha$ PD-1 is enhanced *in situ* by  $\alpha$ CTLA-4 through CD28 or by CD40L via APC activation



## Article

# Myeloid antigen-presenting cell niches sustain antitumor T cells and license PD-1 blockade via CD28 costimulation

Jaikumar Duraiswamy,<sup>1,13</sup> Riccardo Turrini,<sup>2,13</sup> Aspram Minasyan,<sup>2,13</sup> David Barras,<sup>2,3</sup> Isaac Crespo,<sup>2</sup> Alizée J. Grimm,<sup>2</sup> Julia Casado,<sup>4</sup> Raphael Genolet,<sup>2</sup> Fabrizio Benedetti,<sup>2</sup> Alexandre Wicky,<sup>5</sup> Kalliopi Ioannidou,<sup>2</sup> Wilson Castro,<sup>2</sup> Christopher Neal,<sup>2</sup> Amandine Moriot,<sup>2</sup> Stéphanie Renaud-Tissot,<sup>2,6</sup> Victor Anstett,<sup>2</sup> Noémie Fahr,<sup>2</sup> Janos L. Tanyi,<sup>1</sup> Monika A. Eiva,<sup>1,7</sup> Connor A. Jacobson,<sup>8</sup> Kathleen T. Montone,<sup>7</sup> Marie Christine Wulff Westergaard,<sup>9</sup> Inge Marie Svane,<sup>9</sup> Lana E. Kandalaf,<sup>2,6</sup> Mauro Delorenzi,<sup>3,10</sup> Peter K. Sorger,<sup>8</sup> Anniina Färkkilä,<sup>4,11</sup> Olivier Michielin,<sup>5</sup> Vincent Zoete,<sup>2</sup> Santiago J. Carmona,<sup>2</sup> Periklis G. Foukas,<sup>12</sup> Daniel J. Powell, Jr.,<sup>1,7</sup> Sylvie Rusakiewicz,<sup>2,6</sup> Marie-Agnès Doucey,<sup>2</sup> Denarda Dangaj Laniti,<sup>2</sup> and George Coukos<sup>2,14,\*</sup>

<sup>1</sup>Ovarian Cancer Research Center, University of Pennsylvania, Philadelphia, PA 19104, USA

<sup>2</sup>Ludwig Institute for Cancer Research, Lausanne Branch, Department of Oncology, University of Lausanne (UNIL) and Lausanne University Hospital (CHUV), 1011 Lausanne, Switzerland

<sup>3</sup>Bioinformatics Core Facility, Swiss Institute of Bioinformatics, 1015 Lausanne, Switzerland

<sup>4</sup>Research Program of Systems Oncology, University of Helsinki, 00014 Helsinki, Finland

<sup>5</sup>Center for Precision Oncology, Department of Oncology, CHUV, 1011 Lausanne, Switzerland

<sup>6</sup>Center of Experimental Therapeutics, Department of Oncology, CHUV, 1011 Lausanne, Switzerland

<sup>7</sup>Department of Pathology and Laboratory Medicine, University of Pennsylvania, Philadelphia, PA 19104, USA

<sup>8</sup>Harvard Ludwig Center, Laboratory of Systems Pharmacology, Harvard Medical School, Boston, MA 02115, USA

<sup>9</sup>National Center for Cancer Immune Therapy, Copenhagen University Hospital, 2730 Herlev, Denmark

<sup>10</sup>Department of Oncology, UNIL, 1011 Lausanne, Switzerland

<sup>11</sup>Department of Obstetrics and Gynecology, Helsinki University Hospital, 00014 Helsinki, Finland

<sup>12</sup>2nd Department of Pathology, National and Kapodistrian University of Athens, 15771 Athens, Greece

<sup>13</sup>These authors contributed equally

<sup>14</sup>Lead contact

\*Correspondence: [george.coukos@chuv.ch](mailto:george.coukos@chuv.ch)

<https://doi.org/10.1016/j.ccell.2021.10.008>

## SUMMARY

The mechanisms regulating exhaustion of tumor-infiltrating lymphocytes (TIL) and responsiveness to PD-1 blockade remain partly unknown. In human ovarian cancer, we show that tumor-specific CD8<sup>+</sup> TIL accumulate in tumor islets, where they engage antigen and upregulate PD-1, which restrains their functions. Intraepithelial PD-1<sup>+</sup>CD8<sup>+</sup> TIL can be, however, polyfunctional. PD-1<sup>+</sup> TIL indeed exhibit a continuum of exhaustion states, with variable levels of CD28 costimulation, which is provided by antigen-presenting cells (APC) in intraepithelial tumor myeloid niches. CD28 costimulation is associated with improved effector fitness of exhausted CD8<sup>+</sup> TIL and is required for their activation upon PD-1 blockade, which also requires tumor myeloid APC. Exhausted TIL lacking proper CD28 costimulation *in situ* fail to respond to PD-1 blockade, and their response may be rescued by local CTLA-4 blockade and tumor APC stimulation via CD40L.

## INTRODUCTION

CD8<sup>+</sup> T cells are major immune mediators of tumor rejection. Tumor-infiltrating lymphocytes (TIL) exhibit a remarkable diversity *in situ*, with a continuum of phenotypes or molecular states ranging from naive to effector cytolytic cells (van der Leun et al., 2020). Recent studies have shed light on “dysfunctional” or “exhausted” CD8<sup>+</sup> cells that populate melanoma (Sade-Feldman et al., 2018; Tirosh et al., 2016) and other solid tumors (Kim et al., 2020; Wagner et al., 2019; Zheng et al., 2017). PD1<sup>+</sup>CD8<sup>+</sup> TIL exhibit increased expression of coinhibitory receptors and limited effector functions (Baitsch et al., 2011; Sade-Feldman

et al., 2019), analogous to those in chronic viral infections (Blackburn et al., 2008). TIL exhaustion is interpreted as a dynamic state of progressive functional restriction/loss, mediated by transcriptional and epigenetic programs (Chu and Zehn, 2020) and driven by antigen persistence and conditions in the tumor microenvironment (TME) (Guo et al., 2018). However, how TME ecosystems regulate this dynamic population remains largely unknown.

Immune checkpoint blockade (ICB) reinvigorates immune responses especially in TIL-positive tumors (Herbst et al., 2014; Tumei et al., 2014), but the underlying molecular and cellular mechanisms are only partly understood. Response to ICB has



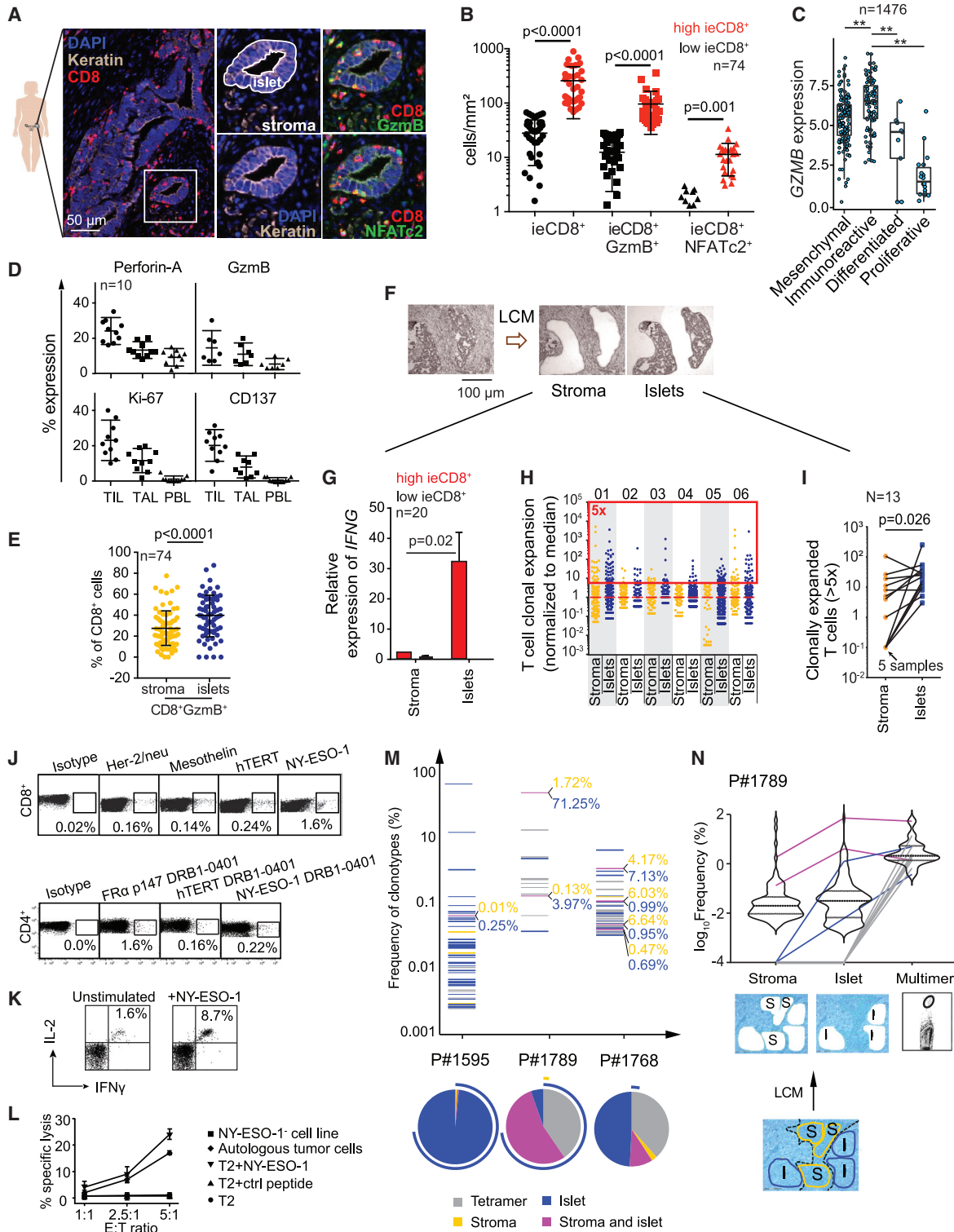


**Figure 1. Ovarian intraepithelial TIL are activated and exhibit markers of TCR engagement *in situ***

(A and B) Representative images (A) and frequency (B) of CD8<sup>+</sup> TIL expressing nuclear (n)NFATc2 or cytoplasmic GzmB in HGSOc.

(C) GZMB expression in four HGSOc molecular subtypes presented as box (median; first and third quartiles) and whisker (extreme value), ANOVA followed by post hoc Tukey test.

(D) Fluorescence-activated cell sorting (FACS) analysis of activation markers in CD8<sup>+</sup> TIL, tumor-associated lymphocytes (TALs) from ascites, and peripheral blood lymphocytes (PBLs) from HGSOc patients.

(legend continued on next page)

been associated with pre-existing immune activation (Ayers et al., 2017; Daud et al., 2016; Riaz et al., 2017) and with the abundance of PD-1<sup>high</sup> TIL in lung cancer (Thommen et al., 2018), or clonally expanded effector T cells within tumors, normal adjacent tissue, and blood (Wu et al., 2020b). In mice, PD-1 blockade activates pre-existing exhausted TIL (Miller et al., 2019) and requires the presence of precursor-exhausted T cells (Siddiqui et al., 2019). Additionally, dendritic cells (DC) (Mayoux et al., 2020; Salmon et al., 2016) critically affect the response to PD-1 blockade. A recently documented molecular interaction between CD28 and PD-1 (Wang et al., 2018; Xu et al., 2020) explains the dependency of PD-1 blockade on CD28 costimulation (Wei et al., 2018) and suggests a key role for DC, but these interactions would purportedly occur within lymph nodes. Whether local intratumoral mechanisms are also involved remains unknown.

In high-grade serous epithelial ovarian cancer (HGSOC), intra-epithelial (ie)TIL—T cells that specifically infiltrate tumor islets—are detected in many patients and correlate with longer survival (Zhang et al., 2003), suggesting tumor immune reactivity. However, despite promising preclinical data (Duraiswamy et al., 2013; Huang et al., 2017), response to PD-1 blockade has been disappointing in the clinic (Matulonis et al., 2019), although somewhat improved by the addition of CTLA-4 blockade (Zamarin et al., 2020). Here, we investigated TIL in HGSOC to help us understand exhaustion mechanisms and the response to ICB.

## RESULTS

### Ovarian islets are enriched in tumor-specific T lymphocytes

While it has long been hypothesized that many ieTIL are tumor-specific cells executing a tumor-rejection program, direct evidence is still lacking. The engraftment of ieCD8<sup>+</sup> TIL within tumor islets requires interferon- $\gamma$  (IFN $\gamma$ )-induced CXCL9, implying recognition of tumor antigen *in situ* (Dangaj et al., 2019). To shed more light, we analyzed 74 advanced chemotherapy-naive HGSOCs (Table S1) by multispectral immunofluorescence microscopy (mlF). Approximately half of the tumors (35/74) harbored ieCD8<sup>+</sup> TIL. Using nuclear localization of (n)NFATc2 and expression of granzyme-B (GzmB) as markers of T cell receptor (TCR) activation and tumor specificity (Figure 1A), we detected nNFATc2<sup>+</sup>GzmB<sup>+</sup>CD8<sup>+</sup> TIL almost exclusively in tumors harboring ieTIL (Figure 1B). Interestingly, *GZMB* (and *CD8A*) overexpression was specific to HGSOC classified as immunoreactive by gene signature, and was associated with significantly

longer survival (Figures 1C, S1A, and S1B). TIL purified from the above tumors with ieTIL exhibited effector-memory (T<sub>EM</sub>) or terminally differentiated (T<sub>EMRA</sub>) phenotypes (Figures S1C and S1D), and, revealing TCR engagement *in situ*, 5%–40% of them expressed perforin-A, GzmB, Ki-67, or CD137, in addition to CD45RO, CD38, HLA-DR, and occasionally CD127 (Figures 1D, S1E, and S1F).

We saw preferential accumulation of GzmB<sup>+</sup>CD8<sup>+</sup> TIL in tumor islets relative to adjacent stroma (Figure 1E), and detected *IFNG* and interleukin-2 (*IL-2*) (Figures 1G and S1G) mainly in laser-capture microdissected tumor islets of ieCD8<sup>+</sup> tumors, while expression was low to absent in the adjacent stroma; and near absent in tumors lacking ieCD8<sup>+</sup> TIL (n = 10; Figure 1F). By TCR $\beta$  sequencing, we found more clonally expanded TIL (ceTIL), a hallmark of tumor specificity (Scheper et al., 2019), in microdissected islets from 13 tumors with ieTIL compared with their adjacent stroma (Figures 1H, 1I, and S1H), indicating that tumor-specific TIL accumulate within islets.

We next looked for antigen-specific TIL in 35 HLA-A2<sup>+</sup> patients with ieCD8<sup>+</sup> tumors. Although ovarian TIL recognize private tumor neoepitopes (Bobisse et al., 2018), here we focused on shared tumor-associated antigens (TAAs) to harmonize observations across patients. For each TAA epitope, we detected 0.14%–1.6% specific CD8<sup>+</sup> and CD4<sup>+</sup> TIL at the steady state, along with IFN $\gamma$  and IL-2 upregulation *ex vivo* in response to cognate TAA peptides (Figures 1J and 1K). Furthermore, sorted TAA-specific CD8<sup>+</sup> TIL recognizing NY-ESO-1, HER2, or hTERT could kill autologous tumor cells (Figure 1L). Importantly, we localized them by sequencing TCR $\beta$  of sorted TAA-specific cells and tracking these TCR $\beta$  sequences in DNA from microdissected islet-stroma pairs: the majority of TCRs from sorted TAA-specific TIL were detected in tumor islets, while only few clonotypes—and at markedly lower frequency—were detected in the adjacent stroma around these islets (Figures 1M, 1N, and S1I). Thus, tumor-specific TCR-activated polyfunctional cytotoxic TIL accumulate mainly in tumor islets in HGSOC, explaining the consistent association of ieCD8<sup>+</sup> TIL with better survival (Goode et al., 2017).

### Tumor-specific iePD-1<sup>+</sup> TIL are activated at the steady state but restricted by PD-1

PD-1 often is a specific feature of tumor-reactive TIL in mouse (Xiong et al., 2019) and human tumors (Gros et al., 2014). Accordingly, ovarian TIL were enriched in PD-1<sup>+</sup> cells, especially within tumor islets (Figures S2A and S2B). Over 60% of TCR-activated (GzmB<sup>+</sup> and/or nNFATc2<sup>+</sup>) ieCD8<sup>+</sup> TIL expressed

(E) Frequency of CD8<sup>+</sup>GzmB<sup>+</sup> cells in stroma and islets of HGSOC (10 or more randomly selected regions, 10%–20% of the tumor section).

(F–I) Laser-capture microdissection (F) and analysis of *IFNG* expression in stroma and islets (G). (H) Relative expansion of individual T cell receptors (TCRs) identified in microdissected stroma or islets by TCR $\beta$  sequencing. A frequency >5-fold relative to the median is considered oligoclonal expansion (red box). See Figure S1H for details. (I) Summary of TCR clonal expansion per tumor compartment (dots show total number of oligoclonal TCRs; lines connect matched stroma and islet from the same tumor; two-tailed Wilcoxon test).

(J) Tetramer stain of CD8<sup>+</sup> and CD4<sup>+</sup> TIL from HGSOC.

(K) Intracellular IFN $\gamma$  and IL-2 in CD8<sup>+</sup> TIL in ovarian tumor-digest cultures.

(L) Sorted NY-ESO-1-specific TIL kill autologous tumor (chromium release assay).

(M) Individual (bar) and cumulative (pie) frequencies of the top 50 clonotypes, with their localization indicated by color, in TAA-specific TIL from islet-stroma pairs in three different patients. The dominant clonotype (top bar) for each patient is shown by an arc surrounding the pie charts.

(N) Violin plot of all clonotypes of patient P#1789 from panel M matched (lines) with the top 50 TCRs from TAA-specific cells sorted by multimer from the same tumor. Internal lines indicate median and first and third quartiles.

Statistical tests: mean  $\pm$  SD, t test or as indicated. See also Figure S1 and Table S1.

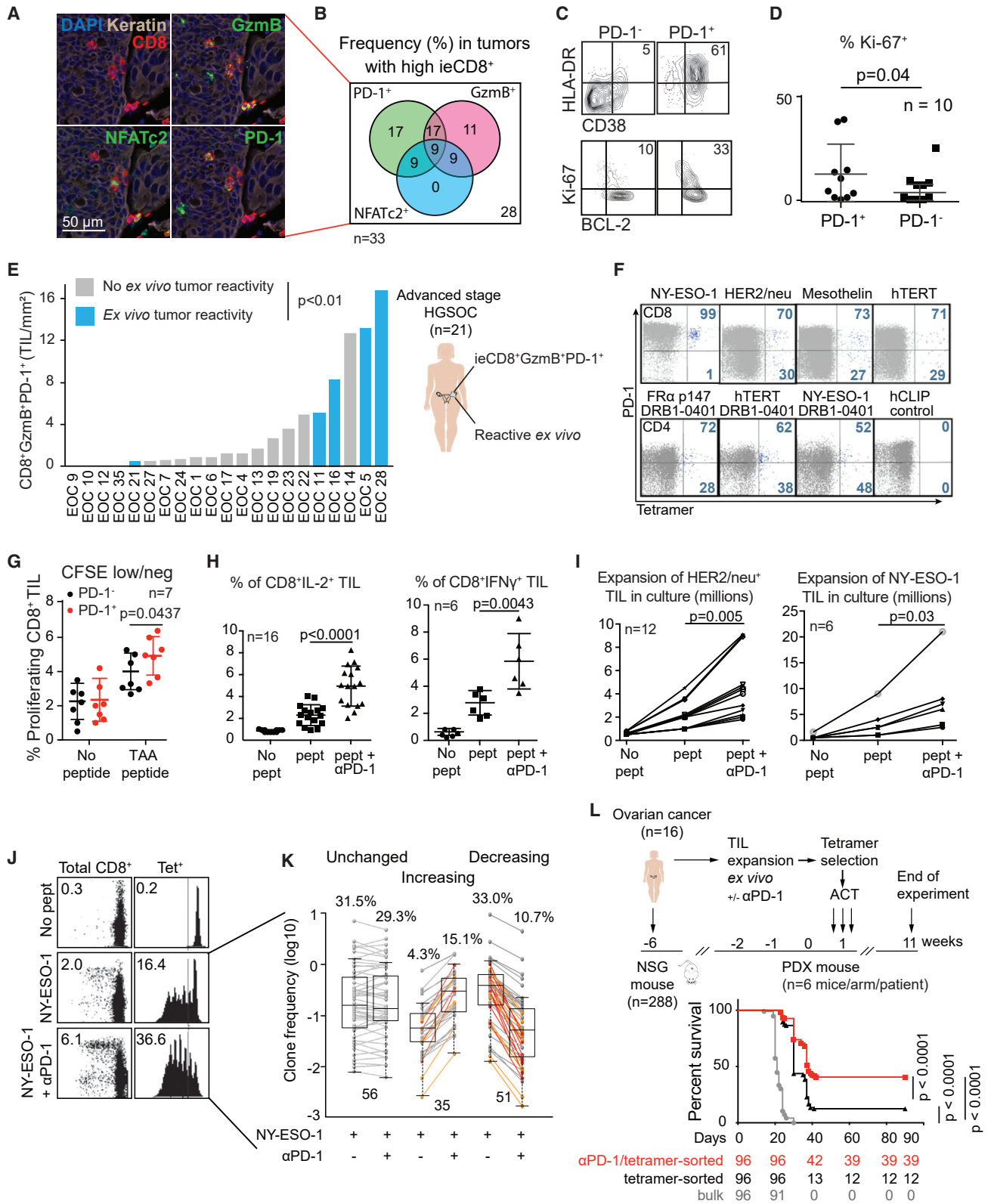


**Figure 2. Tumor-reactive TIL upregulate PD-1, whose blockade reinvigorates their function *in situ***

(A and B) Representative image (A) and Venn diagram with average frequency (B) of intraepithelial (ie)CD8<sup>+</sup>TIL expressing PD-1, GzmB, and/or nuclear NFATc2 in tumors.

(legend continued on next page)

PD-1, while two-thirds of iePD-1<sup>+</sup>CD8<sup>+</sup> TIL expressed GzmB and/or nNFATc2 (Figures 2A and 2B). T<sub>EMRA</sub> CD8<sup>+</sup> TIL were especially enriched in PD-1<sup>+</sup> cells, which were likely to express also GzmB, CCR5, CD38, or HLA-DR (Figures S2C–S2E). Strikingly, a large fraction of the PD-1<sup>+</sup>CD8<sup>+</sup> TIL at the steady state expressed CD27 and BCL-2 (Figures 2C and S2D), a marker associated with memory and polyfunctional T<sub>EM</sub> cells (Dunkle et al., 2013). A fraction of these also expressed Ki-67, which was notably higher in PD-1<sup>+</sup> than PD-1<sup>−</sup>CD8<sup>+</sup> TIL (Figures 2C and 2D).

Intraepithelial CD8<sup>+</sup>PD-1<sup>+</sup>GzmB<sup>+</sup> cells were more frequent in tumors containing tumor-reactive TIL, documented by *ex vivo* IFN $\gamma$ -based reactivity against autologous tumor cell lines (Figure 2E). Indeed, a substantial fraction of TAA-specific CD8<sup>+</sup> (70%–99%) or CD4<sup>+</sup> (52%–72%) TIL were PD-1<sup>+</sup> at the steady state (Figure 2F). In fact, PD-1 was upregulated in ovarian TIL in response to recognition of cognate antigen in fresh tumor-digest cultures, where TIL were stimulated by exogenous class I TAA peptides. Following 3- to 5-day stimulation, we found more proliferating cells in PD-1<sup>+</sup> versus PD-1<sup>−</sup>CD8<sup>+</sup> cells (Figure 2G). Thus, PD-1<sup>+</sup>CD8<sup>+</sup> TIL are tumor-reactive TIL recognizing cognate antigen *in situ* and may be proliferation competent and polyfunctional.

However, PD-1 upregulation may restrict TIL function. In agreement, anti-( $\alpha$ )PD-1 and/or  $\alpha$ PD-L1/2 antibodies enhanced TIL polyfunctionality in response to TAA peptide in tumor-digest cultures, as evidenced by IFN $\gamma$ , IL-2 production, and CD8<sup>+</sup> TIL proliferation (Figures 2H, 2I, and S2F–S2I). Importantly, the fraction of proliferating cells upon PD-1 blockade correlated with the intensity on a per-cell basis of PD-1 expression by input CD8<sup>+</sup> TIL (Figure S2J).

To date it remains unclear whether PD-1 blockade acts on tumor-resident or circulating T cell populations (van der Leun et al., 2020), since TIL clonal replacement has been reported following successful ICB (Yost et al., 2019), and PD-1 blockade may mobilize PD-1<sup>+</sup> T cells in the tumor draining lymph nodes (Dammeyer et al., 2020). We therefore sought to determine whether and how  $\alpha$ PD-1 reinvigorates tumor-specific TIL in the above conditions *in situ*. By tetramer analysis, we noted a variable proliferation of TAA-specific cells *in vitro*, with select expansion or loss of TCR $\beta$  clones (Figures 2J and 2K; STAR Methods), indicating that TIL respond differently to  $\alpha$ PD-1, some proliferating while others are depleted.

We tested the function of TAA-specific cells emerging following PD-1 blockade, by adoptively transferring cells into mice bearing autologous patient-derived xenograft (PDX) tumors. Sorted and expanded TAA-specific TIL, previously activated *ex vivo* with  $\alpha$ PD-1, rejected autologous tumors more efficiently than TAA-specific TIL that had not been exposed to

$\alpha$ PD-1 (control bulk autologous TIL were ineffective, Figures 2L and S3A). Thus, PD-1 blockade can reinvigorate pre-existing exhausted tumor-specific CD8<sup>+</sup> TIL. We confirmed that these are hosted in tumor islets by tracking TAA-specific clonotypes in regressing PDX tumors and finding that the immunodominant clones rejecting PDX tumors in mice originated from the islet compartment (but not stroma) of the original autologous tumors (Figure S3B).

### Polyfunctional PD-1<sup>+</sup>CD8<sup>+</sup> TIL are located in intraepithelial myeloid APC niches

We next sought to understand the milieu of PD-1<sup>+</sup>CD8<sup>+</sup> TIL in tumor islets *in situ*. By mIF, we found frequent iePD-1<sup>+</sup>CD8<sup>+</sup> TIL clustering with iePD-L1<sup>+</sup>CD11c<sup>+</sup> DC, which comprised also iePD-L1<sup>+</sup>CD68<sup>+</sup> macrophages (Figures 3A and S3D). *PDCD1* (PD-1) and *CD274* (PD-L1) gene expression correlated with *CD8A* in ovarian data from The Cancer Genome Atlas (TCGA) (Figure S3C), while mIF frequency of ieCD8<sup>+</sup> TIL correlated with that of iePD-L1<sup>+</sup>CD11c<sup>+</sup> DCs or iePD-L1<sup>+</sup>CD68<sup>+</sup> macrophages, but not PD-L1<sup>+</sup> tumor cells (Figures S3D–S3G). Strikingly, such myeloid clusters were observed within tumor islets (Figures 3A and 3B), where iePD-1<sup>+</sup>CD8<sup>+</sup>TIL were simultaneously in contact with tumor cells and with DC and/or macrophages, while T cells and DC displayed intimate membrane interfaces suggestive of functional immune synapses (Figure S4). These data suggest a role for TIL-myeloid crosstalk while TIL also engage tumor cells.

Tumors with higher frequency of TIL-APC clusters exhibited significantly higher frequency of polyfunctional ieCD8<sup>+</sup>PD-1<sup>+</sup> TIL expressing GzmB and nNFATc2 relative to tumors with low cluster frequency (70% versus 6%), and significantly longer survival (Figures 3C and 3D). Thus, immune attack by polyfunctional effector CD8<sup>+</sup> cells appears to be coordinated with myeloid cells, which infiltrate tumor islets together with tumor-reactive CD8<sup>+</sup> TIL.

To determine whether myeloid clusters are directly involved in supporting polyfunctional TIL, we used high-resolution tissue-based cyclic immunofluorescence (tCyCIF) to compare the neighborhoods and phenotypes of ieCD8<sup>+</sup> cells that were either in intimate contact with DC/macrophages or distant from them (Figures 3E, 3F, and S5A; STAR Methods). We found that intimate encounters were frequent, and over half of ieCD8<sup>+</sup> TIL were engaged in clusters involving ieCD11c<sup>high</sup> DC, ieCD11b<sup>−</sup>CD11c<sup>+</sup>, and/or ieCD163<sup>+</sup>CD11c<sup>+</sup> macrophages (Figures 3G, 3H, and S5B). ieCD8<sup>+</sup> TIL embedded in such myeloid niches expressed significantly higher levels of activation markers and had a higher polyfunctional score (Figures 3I, 3J, and S5C) relative to their “niche-less” counterparts. These data suggest a significant

(C and D) Representative marker expression (C) and Ki-67<sup>+</sup> frequency (D) in PD-1<sup>+</sup> and PD-1<sup>−</sup>CD8<sup>+</sup> TIL (FACS).

(E) The density of polyfunctional ieCD8<sup>+</sup>PD-1<sup>+</sup>GzmB<sup>+</sup> TIL *in situ* is associated with the detection of tumor-reactive TIL *ex vivo* (chi-square,  $p < 0.01$ ).

(F) PD-1 expression in CD8<sup>+</sup> and CD4<sup>+</sup> TIL specific to tumor-associated antigens (FACS). Top: HLA-A2 restricted epitopes; bottom: class II restricted epitopes.

(G) Frequency of proliferating (carboxyfluorescein diacetate succinimidyl ester [CFSE] dilution, FACS) TIL upon *ex vivo* exposure to cognate TAAs.

(H–K) Response of TIL to cognate TAA peptides  $\pm$   $\alpha$ PD-1 in tumor-digest cultures. (H) Baseline (end of culture) frequency of IL-2<sup>+</sup> and IFN $\gamma$ <sup>+</sup>CD8<sup>+</sup> TIL (peptide: NY-ESO-1). (I) Fold expansion of HER2/neu- or NY-ESO-1-specific TIL in response to peptide (tetramer staining). (J) TIL proliferation (CFSE dilution) of total CD8<sup>+</sup>

(left) and tetramer<sup>+</sup> (right) cells. (H–J) FACS analysis. (K) Frequency comparison of individual tetramer-positive clonotypes (from J, >5-fold, orange; >10-fold, red) after *ex vivo* exposure to NY-ESO-1 and  $\alpha$ PD-1. Boxes represent median and first and third quartiles, and whiskers show quartile  $\pm 1.5 \times$  interquartile range.

(L) Experimental design (top) and Kaplan-Meier survival (bottom) of NSG mice bearing patient-derived xenograft (PDX) tumors and treated with adoptive cell therapy of multimer-sorted NY-ESO-1-specific TIL following exposure *ex vivo* to  $\alpha$ PD-1 (red) or not (black) or bulk unselected TIL (gray).

Statistical tests: mean  $\pm$  SD, t test or as indicated. See also Figures S2 and S3.

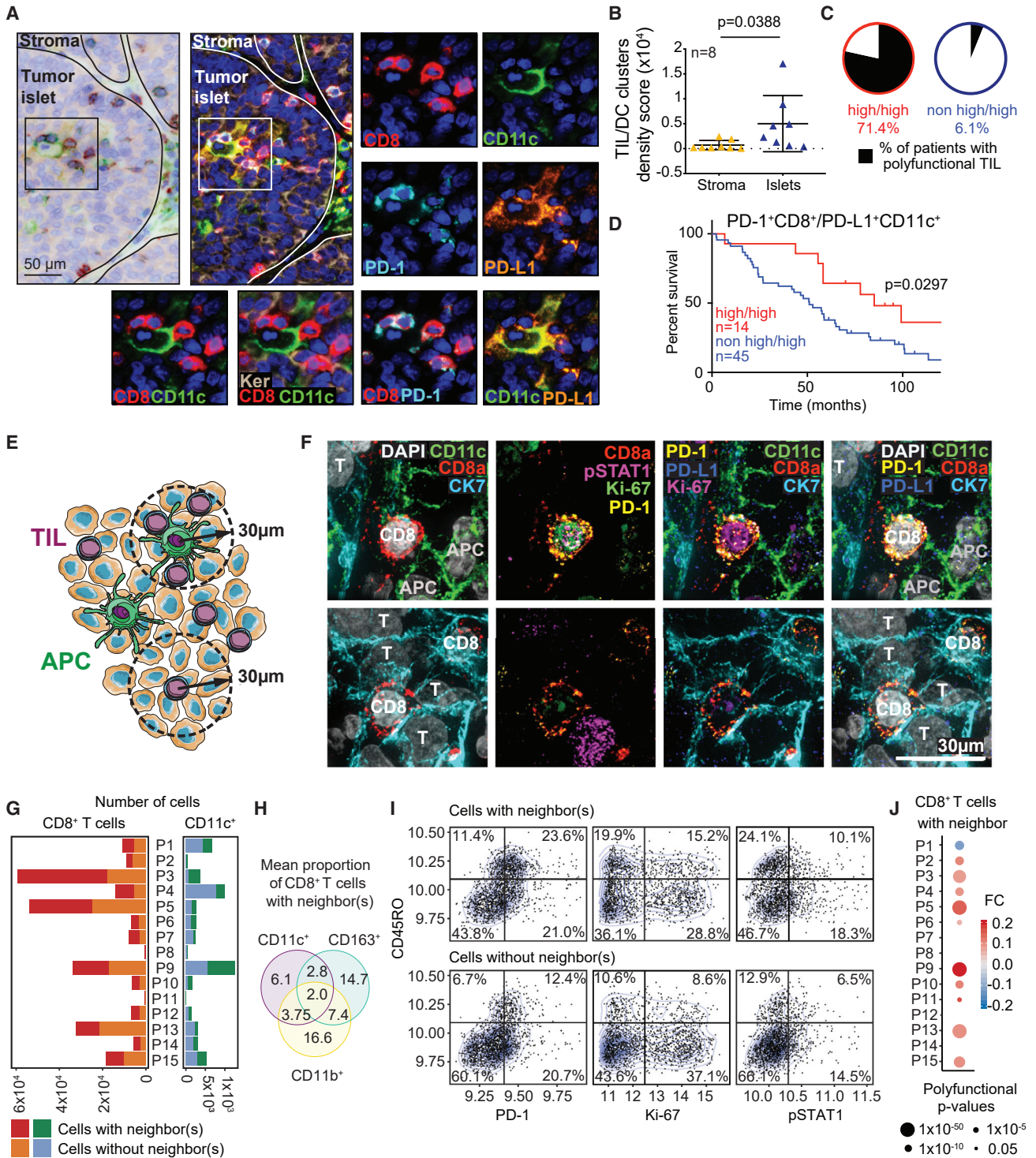


**Figure 3. PD-1<sup>+</sup> CD8<sup>+</sup> TIL associated with intraepithelial myeloid antigen-presenting niches are polyfunctional**

(A–D) Clusters of PD-1<sup>+</sup>CD8<sup>+</sup> TIL with PD-L1<sup>+</sup>CD11c<sup>+</sup> dendritic cells (DC). Representative mIF image (see Figure S4 for details) (A) and cumulative density of clusters in tumor islets versus stroma (B) (mean ± SD, t test). Proportion of polyfunctional (PD-1<sup>+</sup>nNFATc2<sup>+</sup>Gzmb<sup>+</sup>) TIL (C) and progression-free survival (Kaplan-Meier) (D) in tumors that have high number of iePD-1<sup>+</sup>CD8<sup>+</sup> TIL and high number of PD-L1<sup>+</sup>CD11c<sup>+</sup> DC cells per mm<sup>2</sup> (high/high) versus all the other tumors (non-high/high). The groups were split by median, n = 59.

(E–J) tCyCIF imaging analyzing CD8<sup>+</sup> TIL proximity to myeloid antigen-presenting cells (mAPC) and to tumor cells (T) in 15 HGSOE. Schematic view (E) and representative high-resolution images (F) of TIL with CD11c<sup>+</sup> mAPC neighbors (top) and neighborless TIL (bottom). Quantification of ieCD8<sup>+</sup> TIL and CD11c<sup>+</sup>

(legend continued on next page)

topological dependency of CD8<sup>+</sup> TIL polyfunctionality on their association with the myeloid niche. DC and macrophages present in these niches expressed significantly higher levels of PD-L1 (Figure S5C), as expected based on reciprocal activation of DC and macrophages by polyfunctional TIL. Interestingly, in these same tumors we detected tumor-associated lymphoid structures (TLS) (Figure S5D) that were mainly located in the distant omental stroma, outside of the tumor islets. The presence of distant TLS, known to provide a local hub for antitumor immunity (Jansen et al., 2019), correlated with higher frequency of intratumoral TIL-myeloid niches (Figure S5E), suggestive of a coordinated immune attack.

### TCR-engaged CD28-costimulated TIL exhibit increased effector fitness

The above findings suggested that polyfunctional PD-1<sup>+</sup>CD8<sup>+</sup> TIL embedded in mAPC niches receive costimulatory signals at the steady state. By fluorescence-activated cell sorting (FACS) we found an elevated frequency of CD28-expressing cells in TIL and TAL from ascites, which was similar among PD-1<sup>+</sup> and PD-1<sup>+</sup>CD8<sup>+</sup> TIL; however, PD-1<sup>+</sup>CD8<sup>+</sup> TIL expressed higher levels of CD28 on a per-cell basis (Figures 4A, 4B, and S5F). Moreover, PD-1<sup>+</sup>CD8<sup>+</sup> TIL that also expressed CD137, a marker of recent TCR engagement in antigen-responsive T cells (Wolfl et al., 2007), upregulated CD28 compared with their CD137<sup>-</sup> counterparts (Figure 4C). Thus, TCR-engaged PD-1<sup>+</sup>CD8<sup>+</sup> TIL present surface CD28 and could receive CD28 costimulation *in situ*. Importantly, a significant proportion of activated HLA-DR<sup>+</sup>CD11c<sup>+</sup> APC from the same tumors expressed both PD-L1 and CD86 (Figure 4D), the high-affinity ligand that recruits CD28 to the immunological synapse (Pentcheva-Hoang et al., 2004), suggesting that tumor-reactive PD-1<sup>+</sup>CD8<sup>+</sup> TIL embedded in intraepithelial APC niches receive CD28 costimulatory signals that support their polyfunctional phenotype, concomitant to PD-1 co-inhibition, and that the two pathways may interact in this crosstalk.

To learn more about the molecular states of TCR-engaged, exhausted, and CD28-costimulated CD8<sup>+</sup> TIL, we analyzed by single-cell RNA/TCR sequencing 23,000 CD8<sup>+</sup> TIL from 17 ovarian tumor-digest cultures stimulated with TAA peptides. Unsupervised clustering revealed seven distinct clusters of TIL (Figure 4E). Each cell was assigned an “exhaustion” (Tex) and a CD28 costimulation (CD28cost) score (STAR Methods and Table S2). Cluster 2 exhibited simultaneously higher CD28cost and Tex states, and we noted an important overlap in the distribution of the two states (Figures 4F–4G). The significant correlation between the two scores was driven mostly by CD8<sup>+</sup> TIL with high exhaustion (top tertile; Figures 4H, S5G, and S5H). CD8<sup>+</sup> TIL with higher Tex and CD28cost scores were the most clonally expanded and exhibited a unique gene expression profile of antigen-experienced cells (Figures 4I, S5I, and S5J; Table S3).

To gain further insight into the state of CD28-costimulated tumor-specific TIL, we focused on ceTIL ( $\geq 10$  cells/TCR sequence), which are likely tumor specific (van der Leun et al.,

2020). Interestingly, individual TIL clones (identified by identical TCRs) exhibited a similar Tex state but spanned across a range of CD28-costimulated states (Figure 4J), suggesting an evolution process consistent with the notion that T cell activation/exhaustion states are dictated by the TCR (Azizi et al., 2018), while CD28cost may evolve according to the individual cell milieu. Focusing on ceTIL with high exhaustion scores, cells also exhibiting a high CD28-costimulated state (i.e., Tex<sup>hi</sup>CD28cost<sup>hi</sup>) displayed features of polyfunctional cells with enhanced effector fitness relative to their Tex<sup>hi</sup>CD28cost<sup>low</sup> counterparts. Relative to their counterparts lacking the CD28cost state, Tex<sup>hi</sup>CD28cost<sup>hi</sup> exhibited significantly higher gene expression levels for effector machinery components, including: TCR and its signaling partners; granzymes; cytotoxic granules and vesicular trafficking; inflammatory mediators; chemokines; costimulation; survival/proliferation; cytoskeletal proteins involved in the organization of the immunological synapse and lipid rafts; migration; and metabolic programs (Figure 4K; Tables S4 and S5). Notably, the highest upregulated genes were class II HLA molecules, which in conjunction with CD28 delineate CD8<sup>+</sup> lymphocytes with higher telomerase activity (Speiser et al., 2001) and participate in homotypic T cell activation conferring protective memory in CD8<sup>+</sup> cells (Holling et al., 2004).

Next, from the single-cell RNA sequencing (scRNA-seq) data, we inferred regulatory activities of 385 known transcription factors (TFs) and found a clear gradient within the Tex states (Figure 4L). Among the top TFs predicted to be active predominantly in Tex<sup>hi</sup>CD28cost<sup>hi</sup> cells, we found NR5A2, RFX5, STAT1, IRF1, IRF5, and BATF, each variably implicated in BCL-2-mediated survival, expansion, memory formation, and/or effector functions in T cells (Kurachi et al., 2014; Ohteki et al., 2001; Quigley et al., 2008; Seitz et al., 2019; Yan et al., 2020); RUNX3, which promotes CD8<sup>+</sup> T cell tissue residence memory (Milner et al., 2017); and RFX5, shown to mediate activation of MHC class II genes (Brickey et al., 1999) (Figure 4M). Furthermore, EOMES, a TF implicated in the durability of precursor-exhausted T cells (Tpex) (Chen et al., 2019), was found to be activated in Tex<sup>hi</sup>CD28cost<sup>hi</sup> CD8<sup>+</sup> T cells. Thus, a subset of Tex<sup>hi</sup> tumor-specific CD8<sup>+</sup> cells exhibit high CD28-costimulation state and increased effector fitness, driven by specific transcriptional programs.

### TIL activation upon PD-1 blockade depends on CD28 costimulation provided *in situ* by tumor-resident mAPC

The above results indicate that the functional state of phenotypically exhausted tumor-reactive CD8<sup>+</sup> TIL could be predicated based on the availability of local CD28 signals, such that a proportion of Tex CD8<sup>+</sup> TIL in some tumors receives CD28 costimulation by local APC and exhibit polyfunctionality. Given that CD28 may be inactivated by PD-1 (Xu et al., 2020), we asked whether PD-1 blockade leads to CD8<sup>+</sup> TIL activation by virtue of restoring CD28 costimulation *in situ*. We employed p2TA, a peptide mimetic (CD28<sub>8–15</sub>) of the second CD28 domain, which overlaps with the CD28 dimer interface and disrupts CD28-superantigen

mAPC neighborhoods per patient (G) and cumulative diagram for all mAPC (H). (I) Scatterplot display of a tCyCIF measured expression of PD-1, Ki-67, pSTAT1, and CD45RO in CD8<sup>+</sup> TIL in a representative sample. (J) Significant fold change (FC;  $p < 0.05$ ) of average polyfunctional score in ieCD8<sup>+</sup> cells with any mAPC neighbor relative to neighborless ieCD8<sup>+</sup> cells.

See also Figures S3–S5.

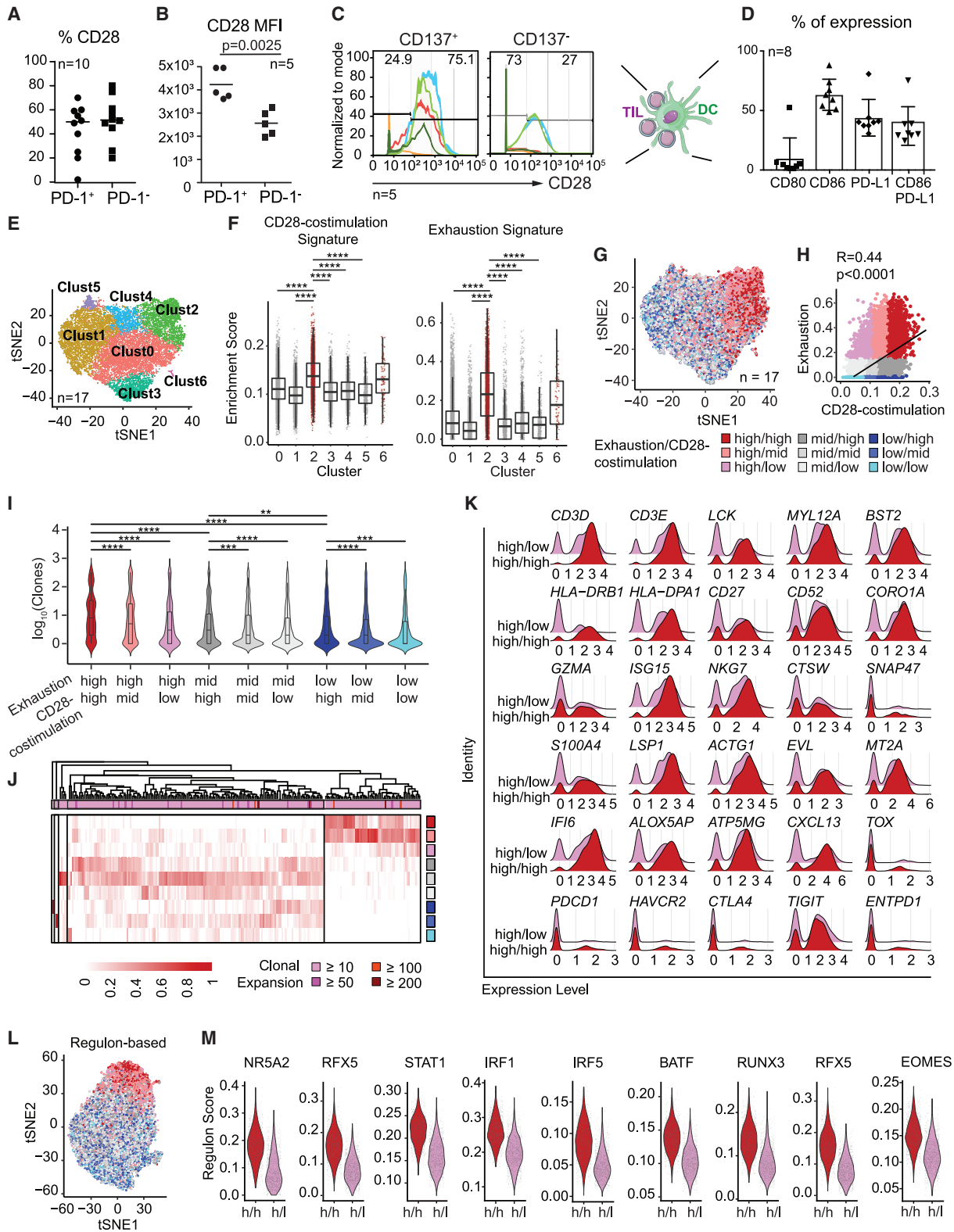


**Figure 4. Identification of CD28-costimulated PD-1<sup>+</sup>CD8<sup>+</sup> TIL**

(A and B) Frequency (A) and expression levels (B; mean fluorescent intensity) of CD28 in CD8<sup>+</sup>PD-1<sup>+</sup> or PD-1<sup>-</sup> patient cells (FACS, t test).  
(C) CD28 expression in CD8<sup>+</sup>CD137<sup>+</sup> or CD137<sup>-</sup> TIL (mass cytometry, mean metal intensity).  
(D) Frequency of HLA-DR<sup>+</sup>CD11c<sup>+</sup> tumor-derived DC expressing CD80, CD86, PD-L1, or double CD86/PD-L1 (FACS, mean ± SD, t test).

(legend continued on next page)

interaction (Arad et al., 2011). By molecular modeling, we predicted direct binding and disruption of the CD28 dimerization by p2TA (STAR Methods). Since activation of CD28 signaling in T cells requires CD28 dimerization (Greene et al., 1996; Sørensen et al., 2004), we hypothesized that p2TA disrupts signaling by B7 ligands. Indeed, P2TA abrogated activation of donor T cells by influenza virus peptide presented by autologous mature DC in the absence of superantigen (Figure S6A). Importantly, activation of TIL by PD-1 blockade was largely attenuated by p2TA *in vitro*. Interestingly, TIL activation was not restored by IL-2 (Figures 5A and S6B).

Furthermore, we found that TIL activation by PD-1 blockade is supported by local mAPC. Indeed, the effect of  $\alpha$ PD-1 on CD8<sup>+</sup> TIL proliferation was lost in mAPC-depleted autologous TME cultures (Figure 5A), thus proving that human tumor-resident mAPC are required *in situ* for effective T cell activation upon PD-1 blockade. We conclude that mAPC—via CD28 costimulation—determine whether tumor-specific TIL respond functionally to PD-1 blockade. In support of this conclusion, we compared pre-treatment expression data of 179 patients with various cancer types and known  $\alpha$ PD-1 response. We found upregulation of both activated T cell and mAPC signatures correlating with  $\alpha$ PD-1 treatment response (Figures 5B and S6C).

The above findings suggest that the magnitude of CD28 signaling dictates responsiveness of TIL to  $\alpha$ PD-1. Interestingly, we observed a short-lived but significant (>2 fold) increase of CD8<sup>+</sup> TIL expressing surface CD28 within 30 min of  $\alpha$ PD-1 treatment, specifically in responding TME (6/6) but not in non-responding ones (1/16) (Figure S6D). We detected concomitant increased ERK phosphorylation within 60 min of  $\alpha$ PD-1 treatment, followed by increased TIL proliferation (Figures 5C and 5D). These events were abrogated by p2TA, consistent with dependency of PD-1 blockade on CD28 signaling (Figures 5C and 5D).

We confirmed such dependency using a human NY-ESO-1-specific CD8<sup>+</sup> TIL clone against HLA-A2\*NY-ESO-1<sup>+</sup> OVCAR5 cells (Figures 5E, 5F, S6E, and S6F). Although rested T cells killed PD-L1<sup>+</sup> OVCAR5 targets, exhausted PD-1<sup>+</sup> T cells lost the ability to kill, and PD-1 blockade was not sufficient to restore killing. However, forced expression of CD28 ligands on OVCAR5 cells restored the ability of  $\alpha$ PD-1 to activate the cytolytic function of exhausted PD-1<sup>+</sup>CD8<sup>+</sup> T cells (Figure 5F). These findings are in agreement with evidence from other experimental systems (Wang et al., 2018) and show that effective PD-1 blockade requires CD28cost to restore human TIL function in the TME. Furthermore, in *in vivo* experiments using intraperitoneal (i.p.) *Tp53<sup>-/-</sup>Brca1<sup>-/-</sup>* ID8 ovarian tumors, coinjection of CD28-neutralizing antibody with  $\alpha$ PD-1 ICB abrogated its therapeutic effects early after tumor engraftment (Figures 5G and S6G).

Thus, as in the viral milieu (Kamphorst et al., 2017), PD-1 blockade can overcome tumor-induced exhaustion via CD28 activation and, as in human tumors, we found PD-1<sup>+</sup>CD8<sup>+</sup> TIL in mouse *Tp53<sup>-/-</sup>Brca1<sup>-/-</sup>* ID8 tumors, and at the steady state these were enriched in Ki-67<sup>+</sup>, GzmB<sup>+</sup>, and CD137<sup>+</sup> cells compared with PD-1<sup>-</sup>CD8<sup>+</sup> TIL (Figure S6H). Moreover, the frequency of polyfunctional PD-1<sup>+</sup>CD8<sup>+</sup> TIL correlated with the frequency of PD-L1<sup>+</sup>DC in the PD-1-treated group (Figure S6I).

### CTLA-4 restrains TIL activation, and its blockade *in situ* enhances $\alpha$ PD-1 locally via CD28

CTLA-4 attenuates CD28 costimulatory signaling by APC, and its blockade is thought to enhance T cell priming in lymph nodes (Wei et al., 2017). In the TCGA ovarian cancer database, high *CTLA4* and *PDCD1* expression was associated with activated T cell and mAPC signatures (Figure S6J). A fraction of PD-1<sup>+</sup> but not PD-1<sup>-</sup>CD8<sup>+</sup> TIL from HGSOE expressed intracellular CTLA-4, showing that CTLA-4 is a hallmark of tumor-reactive CD8<sup>+</sup> TIL, with most TAA-specific TIL expressing CTLA-4 (Figures 6A and 6B). Consistently, we found significantly more tumor-reactive CD137<sup>+</sup> (Ye et al., 2014) cells among CTLA-4<sup>+</sup> than CTLA-4<sup>-</sup> PD-1<sup>+</sup>CD8<sup>+</sup> TIL, and significantly higher CD28<sup>+</sup> frequency among CD137<sup>+</sup> than CD137<sup>-</sup>PD-1<sup>+</sup>CTLA-4<sup>+</sup>CD8<sup>+</sup> TIL across tumors (Figures 6C and S6K). Thus, a fraction of TCR-activated tumor-reactive CD8<sup>+</sup> TIL is potentially positioned to benefit from CD28 costimulation, if embedded in mAPC niches (Figure 6D). PD-1<sup>+</sup>CTLA-4<sup>+</sup>CD8<sup>+</sup> cells expressing CD28 exhibited higher LEF1, EOMES, and CD27, indicating similarities with precursor-exhausted T cells, and displayed a higher polyfunctional state, with greater proliferation (Ki-67), higher IL-2, pSTAT5, and multiple effector molecules, in addition to higher expression of costimulatory receptors (GITR and OX40) at baseline (Figures 6E–6G and S6L). Highlighting the overlap between CD137<sup>+</sup>PD-1<sup>+</sup>CTLA-4<sup>+</sup>CD28<sup>+</sup>CD8<sup>+</sup> TIL identified by mass cytometry and Tex<sup>hi</sup>CD28cost<sup>hi</sup> CD8<sup>+</sup> cells identified by scRNA-seq, proteins highly expressed in the former were also highly expressed at the gene level in Tex<sup>hi</sup>CD28cost<sup>hi</sup> cells (Figures S6L and S6M).

We next asked whether CTLA-4 blockade could act directly *in situ*, combined with  $\alpha$ PD-1, to further activate TIL. The addition of  $\alpha$ CTLA-4 to tumor-digest cultures along with  $\alpha$ PD-1 and TAA peptides significantly enhanced expression of T-bet, a central TF of the effector-memory state that prevents transition to terminal exhaustion (Beltra et al., 2020), and increased GzmB expression, as well as IFN $\gamma$  production and proliferation (Figures 6H–6J) relative to cultures treated with  $\alpha$ PD-1 alone. Importantly, response to  $\alpha$ CTLA-4 also required local tumor mAPC and CD28 expression, and was abrogated when mAPC were depleted from cultures or in the presence of p2TA peptide (Figure 6K). Thus,  $\alpha$ CTLA-4 can act directly in the TME to activate

(E–M) scRNA-seq of CD8<sup>+</sup> TIL from 17 ovarian tumor-digest cultures. (E) Unsupervised clustering. (F) CD28-costimulation (CD28cost, left) and exhaustion (Tex, right) scores per cluster from (E) (Wilcoxon test,  $p < 2.22 \times 10^{-16}$ ). Distribution (G) and Pearson correlation (H) of the Tex and CD28cost states. The first word in the legend refers to Tex, the second to CD28cost. (I) Enrichment of clonally expanded cells in the TexCD28cost states (Wilcoxon test,  $p \leq 0.0016$ ). For each clonotype, the number of occurrences of the given TCR in the sample was calculated and plotted at the log<sub>10</sub> scale. (J) Distribution of ceTIL ( $\geq 10$  cells/TCR,  $n = 208$  total clones) across states. Colors from red to blue represent nine Tex/CD28cost states as in (G) and (H). (K) Select differentially expressed genes between high/high and high/low Tex/CD28cost states in clonally expanded cells ( $\geq 10$  cells/TCR). (L) Distribution of Tex/CD28cost states in a regulon map. Colors from red to blue represent nine Tex/CD28cost states. (M) Comparison of regulon activity between high/high and high/low TexCD28cost states (h/h: Tex<sup>hi</sup>CD28cost<sup>hi</sup>; h/l: Tex<sup>hi</sup>CD28cost<sup>low</sup>).

Box plots defined as box (median; first and third quartiles) and whisker (extreme value). See also Figure S5.

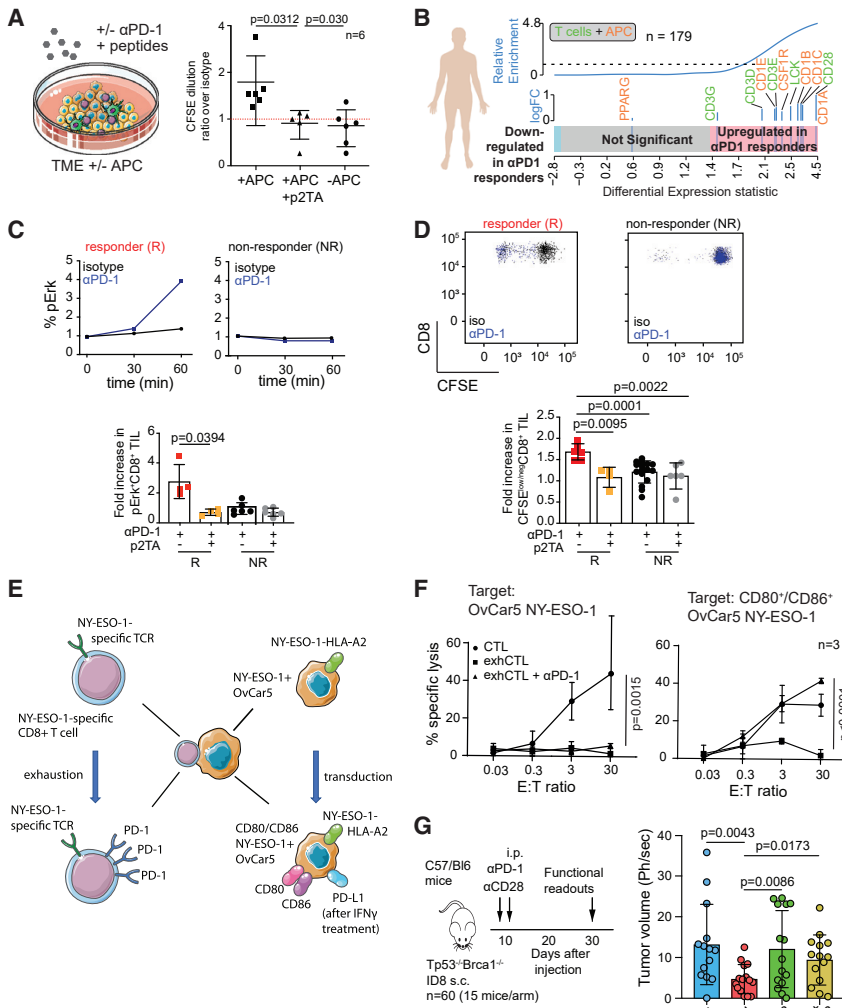


**Figure 5. mAPC and CD28 are required for effective TIL activation upon PD-1 blockade**

(A) Proliferation (CFSE dilution) of CD8<sup>+</sup> TIL in response to TAA peptides and  $\alpha$ PD-1 (fold increase relative to isotype control antibody) in tumor-digest cocultures, at baseline (i.e., APC present, +APC), with addition of CD28 antagonist p2TA, or following myeloid APC depletion (-APC).

(B) Enrichment of a combined T cell/myeloid APC gene signature in patients responding to  $\alpha$ PD-1 in clinical studies (merged cohort of various cancer types; see Figure S6C for details).

(C and D) Representative (top) and cumulative data (bottom) of kinetics of ERK phosphorylation (C) and cell proliferation (CFSE dilution, D) detected in CD8<sup>+</sup> TIL after PD-1 blockade, in responder (n = 6) and non-responder (n = 16) tumor-digest cultures (FACS).

(E and F) Experimental scheme (E) and cell lysis (<sup>51</sup>Cr assay, F) of OVCAR5 cells engineered (or not) to express ectopic CD80/CD86 and PD-L1 by NY-ESO-1<sub>157-165</sub>-specific CD8<sup>+</sup> TIL clone. TIL were either rested cytolytic cells (CTL), exhausted (exhCTL), or exhausted and supplemented by  $\alpha$ PD-1.

(G) Scheme of the experiment (left) and best responder (right) of *Tp53*<sup>-/-</sup>*Brca1*<sup>-/-</sup> ID8 tumors to  $\alpha$ PD-1 and/or  $\alpha$ CD28 treatment *in vivo*.

Statistical tests: mean  $\pm$  SD, t test or as indicated. See also Figure S6.

TIL and enhance PD-1 blockade, and both interventions activate TIL by releasing their respective blocks on CD28 costimulation provided by tumor-resident mAPC.

We validated the positive interaction of  $\alpha$ PD-1 and  $\alpha$ CTLA-4 *in vivo* in immunodeficient NSG mice reconstituted with HLA-A2<sup>+</sup> human CD34<sup>+</sup> cord blood cells and bearing OVCAR5 tumors (STAR Methods), where we identified HER2<sub>369-377</sub>-specific CD8<sup>+</sup> TIL expressing IFN $\gamma$  *in situ* and exhibiting *ex vivo* cytolytic activity against OVCAR5 cells. Dual ICB elicited higher expansion of such TIL *in situ* and increased mouse survival relative to single ICB (Figures 6L–6O). Finally, we confirmed that  $\alpha$ CTLA-4 directly reinvigorates exhausted CD8<sup>+</sup> TIL upon PD-1 blockade, taking advantage of the aforementioned NY-ESO-1-specific cytolytic TIL clone. Addition of  $\alpha$ CTLA-4 significantly enhanced the effect of  $\alpha$ PD-1 in activating exhausted TIL against NY-ESO-1<sup>+</sup> OVCAR5 cells expressing CD28 ligands (Figure S6N).

### TCR-engaged CD28-costimulated TIL with increased effector fitness respond to ICB

From the above, we surmised that tumor-reactive TIL exhibiting both exhaustion and CD28cost transcriptional programs are better equipped to respond to ICB. To test this hypothesis, we stim-

ulated ovarian-digest cultures, previously profiled for TIL at baseline (Figure 4E), with TAA peptides plus ICB. Cultures that mounted polyfunctional TIL responses to ICB were distinguished for comprising at baseline frequent CD8<sup>+</sup> clonotypes with Tex<sup>hi</sup>CD28cost<sup>hi</sup> phenotype among highly clonally expanded TIL ( $\geq 50$  cells/TCR, n = 2,334 cells), while in non-responding

cultures clonally expanded TIL comprised either Tex<sup>hi</sup>CD28cost<sup>low</sup> or Tex<sup>low</sup>CD28cost<sup>low</sup> cells, with a positive correlation between the Tex<sup>hi</sup> and CD28cost<sup>hi</sup> states seen only in responders (Figures 7A, 7B, and S7A).

We identified seven molecular clusters within these clonally expanded CD8<sup>+</sup> TIL, three of which (0/5/6) were highly enriched for Tex<sup>hi</sup>CD28cost<sup>hi</sup> clones and specifically associated with response to ICB *ex vivo* (Figures 7C–7E, S7B, and S7C). We derived a five-gene signature, henceforth referred to as PD1R, using the top differentially expressed genes (*CXCL13*, *HLA-DRB5*, *CCL5*, *CD74*, and *CLIC1*) between responding and non-responding TIL, and noted enrichment specifically in Tex<sup>hi</sup>CD28cost<sup>hi</sup> TIL (Figures 7F and S7D). Importantly, PD1R was overexpressed in baseline biopsies of patients with resectable melanoma who did not relapse after neoadjuvant pembrolizumab and surgical excision (Figure 7G). Moreover, TCGA cancers known to respond better to  $\alpha$ PD-1 therapy (i.e., melanoma, non-small-cell lung, head and neck, kidney, and bladder cancers) more frequently overexpressed PD1R and the CD28cost signature compared with cancers known to be less responsive to ICB (glioblastoma, colon, prostate, esophageal, ovarian, and uterine carcinomas; Figure 7H). Additionally,

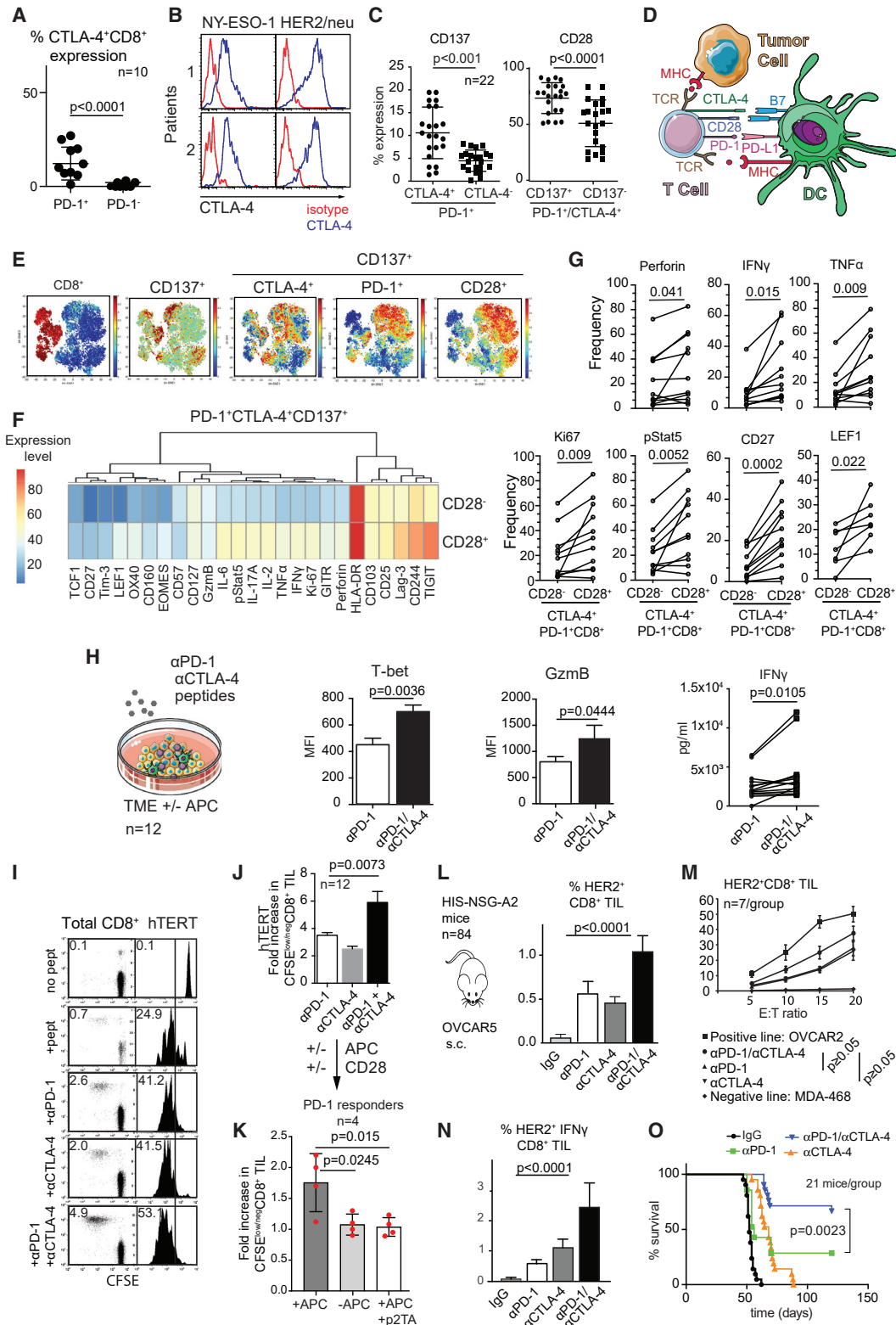


**Figure 6. CTLA-4 blockade *in situ* enhances TIL activation by  $\alpha$ PD-1 via CD28**

(A and B) Expression of intracellular CTLA-4 in PD-1<sup>+</sup> and PD-1<sup>+</sup> CD8<sup>+</sup> TIL (A) and in tumor antigen-specific CD8<sup>+</sup> TIL (B, representative histograms). (C) Frequency of CD137<sup>+</sup> TIL in CTLA-4<sup>+</sup> or CTLA-4<sup>-</sup> PD-1<sup>+</sup>CD8<sup>+</sup> TIL (left) and of CD28<sup>+</sup> TIL in CD137<sup>+</sup> or CD137<sup>-</sup> CTLA-4<sup>+</sup>PD-1<sup>+</sup> CD8<sup>+</sup> TIL (mass cytometry). (D) Crosstalk with APC regulates CD28 costimulation in tumor-reactive TIL embedded in the intraepithelial tumor niche.

(legend continued on next page)

univariate analysis revealed a significant positive correlation between PD1R and objective response rates (ORR) to  $\alpha$ PD-1 in solid tumors ( $p = 0.0459$ ), while use of either PD1R or the CD28cost signature correlated with ORR in a multivariate model that also included tumor mutational burden ( $p = 0.015$  and  $p = 0.013$ , respectively; Figure 7I and Table S6). Lastly, we found a clear enrichment for the CD28cost signature and a trend for enrichment for PD1R across the cohort of patients from Figure 5B responding to  $\alpha$ PD-1 (Figure S7E).

Thus, tumors harboring  $\text{Tex}^{\text{hi}}\text{CD28cost}^{\text{hi}}$  TIL are more likely to respond to ICB. Since these TIL are associated with myeloid niches *in situ*, we asked whether myeloid interactions of PD-1<sup>+</sup> TIL are predictive for response to ICB. In a cohort of 26 metastatic melanoma patients undergoing frontline ICB, we found by mIF a significantly higher frequency of TIL in proximity to CD11c<sup>+</sup> cells *in situ* in patients who achieved an objective response to ICB relative to patients who failed to respond (Figure 7J).

### CD40 activation amplifies TIL responsiveness to ICB

We finally reasoned that tumors where PD-1<sup>+</sup> TIL are incapable of responding to  $\alpha$ PD-1 might be deficient in CD28 ligands *in situ*, i.e., they lack properly activated myeloid APC. Since CD40 ligands are known to activate mAPC, we used a cohort of 22 ovarian tumor-digest cultures to ask whether local delivery of CD40L could potentiate the activation of TIL *in situ* by  $\alpha$ PD-1/ $\alpha$ CTLA-4 blockade. We found that combining CD40L with  $\alpha$ PD-1/ $\alpha$ CTLA-4 and peptide stimulation elicited polyfunctional TIL activation in more tumors ( $n = 9/22$ ) relative to  $\alpha$ PD-1/ $\alpha$ CTLA-4 ( $n = 6/22$ ) or  $\alpha$ PD-1 alone ( $n = 4/22$ , Figures 8A and S8A).

We profiled TIL and CD11b<sup>+</sup> cells at baseline in 12 of the above tumors (Figures S7A, S8A, and S8B), whose TIL responded to single  $\alpha$ PD-1 ( $n = 2$ ), only to triple treatment ( $n = 5$ ), or to no treatment ( $n = 5$ ). Through MegaClust unsupervised analysis, we identified numerous myeloid cell and TIL phenotypes in tumors with responsive or non-responsive CD8<sup>+</sup> cells. We used orthogonal projections to latent structures discriminant analysis to assign relative discriminant scores for correlation with response to each cell cluster (Figure S8B). Combined use of lymphoid and myeloid phenotypes achieved better separation of responsive tumors than each cell type separately, suggesting that both T cell and myeloid cell states determined CD8<sup>+</sup> TIL response (Figure 8B). Activated myeloid phenotypes with high expression at baseline of CD28 ligands CD86 and CD80, class I/II HLAs (phenotype M22), PD-L1 and CD40 (M35, M36, M53), and PD-L2 and HVEM (M67; Figures 8C and S8C) showed the strongest positive discriminative power for CD8<sup>+</sup> activation by ICB. Furthermore, baseline expression of PD-1, CD28, CTLA-4, CD137, OX40, and ICOS (phenotype L33) discriminated TIL

that could be activated by  $\alpha$ PD-1 and CD40L combination (Figures 8C and S8C). Importantly, myeloid phenotypes were mostly not discriminatory for response to CD40L combination, indicating that CD40L can compensate for suboptimal baseline activation of the myeloid compartment and enable TIL response to ICB. However, CD8<sup>+</sup> TIL overexpressing CD103, a marker of tumor-resident memory cells, as well as CD137, PD-1, and CTLA-4 (phenotypes L29, L39, and L45), plus the L33 phenotype, were discriminatory for response to the CD40L combination (Figures 8C and S8C).

To ask whether our *in vitro* findings have implications for other tumor types, we derived an activated myeloid cell gene signature based on the above myeloid markers associated with  $\alpha$ PD-1 responsive ovarian TIL, and interrogated baseline biopsies of patients with resectable melanoma receiving neoadjuvant pembrolizumab (same as in Figure 7G). Tumors that did not relapse post  $\alpha$ PD-1 were significantly enriched for the myeloid signature (Figure S8D). Furthermore, in the cohort of patients with various advanced cancer types from Figure 5B, the myeloid signature was associated with response to ICB (Figures S8E and S8F; Table S7).

These findings confirm that tumor myeloid activation is a key determinant of response to PD-1/CTLA-4 blockade and indicate that this can be therapeutically achieved by CD40L. To test this, we treated mice bearing orthotopic i.p. *Tp53*<sup>-/-</sup>*Brca1*<sup>-/-</sup> ID8 ovarian tumors with CD40L plus  $\alpha$ PD-1 or  $\alpha$ PD-1/ $\alpha$ CTLA-4. In agreement with the human data, we found that triple therapy led to more effective tumor control relative to single or double interventions (Figures 8D and S8G).

## DISCUSSION

The ovarian TME captures many elements that are shared across solid tumors and thus is informative in studying underlying mechanisms of immunoreactivity. We chose HGSOc to study how TIL carry out their mission of tumor attack and to better understand the limiting responses of HGSOc to ICB therapy. Our data support the notion that the exhaustion state of iTIL marked by PD1 upregulation is a hallmark of tumor reactivity.

Recent mouse studies have identified the differentiation pathway responsible for T cell exhaustion and have found a committed lineage, forced by a fixed epigenetic context, within which key TF dictate an evolution across four identifiable states, from progenitor Tex to terminal Tex (Khan et al., 2019). Here we report a novel state within CD8<sup>+</sup> Tex cells, characterized by a polyfunctional effector phenotype specifically associated with CD28 costimulation. Unlike canonical Tex cells lacking CD28cost,  $\text{Tex}^{\text{hi}}\text{CD28cost}^{\text{hi}}$  cells exhibited superior effector

(E–G) Mass cytometry profiling of TIL from 11 HGSOc. (E) Distribution of TIL populations. (F) Cumulative expression of markers in CD28<sup>+</sup> and CD28<sup>-</sup> subsets of CD137<sup>+</sup>CTLA-4<sup>+</sup>PD-1<sup>+</sup> CD8<sup>+</sup> TIL. (G) Expression of precursor, memory, and activation markers in CD28<sup>+</sup> and CD28<sup>-</sup> subsets of PD-1<sup>+</sup>CTLA-4<sup>+</sup> CD8<sup>+</sup> TIL.

(H–K) TIL activation in tumor-digest cultures in response to tumor antigen peptides and ICB (FACS). (H) Left to right: experimental scheme and levels of T-bet, GzmB, and IFN $\gamma$  secretion. Representative (I) and cumulative CD8<sup>+</sup> TIL proliferation (CFSE dilution) (J) in tumor-digest cultures. (K) Abrogation of response to  $\alpha$ PD-1/ $\alpha$ CTLA-4/TAA peptides in  $\alpha$ PD-1 responders: at baseline (i.e., APC present, +APC), with addition of CD28 antagonist p2TA (+APC/+p2TA), or following myeloid APC depletion (–APC).

(L–O) Response to  $\alpha$ PD-1/ $\alpha$ CTLA-4 in HLA-A2\* CD34-reconstituted human immune system/NSG mice (HIS-NSG-A2) bearing OVCAR5 tumors. (L) Detection of TIL recognizing HER2 peptide in mice treated with control IgG,  $\alpha$ PD-1, and/or  $\alpha$ CTLA-4. (M) Cytolytic activity (<sup>61</sup>Cr assay) of HER2-specific TIL against OVCAR5 cells. TIL were sorted by multimer from responding mice. (N) Detection of HER2-specific IFN $\gamma$ <sup>+</sup>CD8<sup>+</sup> TIL. (O) Kaplan-Meier survival curves in mice treated with control IgG,  $\alpha$ PD-1, and/or  $\alpha$ CTLA-4.

Statistical tests: mean  $\pm$  SD, t test or as indicated. See also Figure S6.

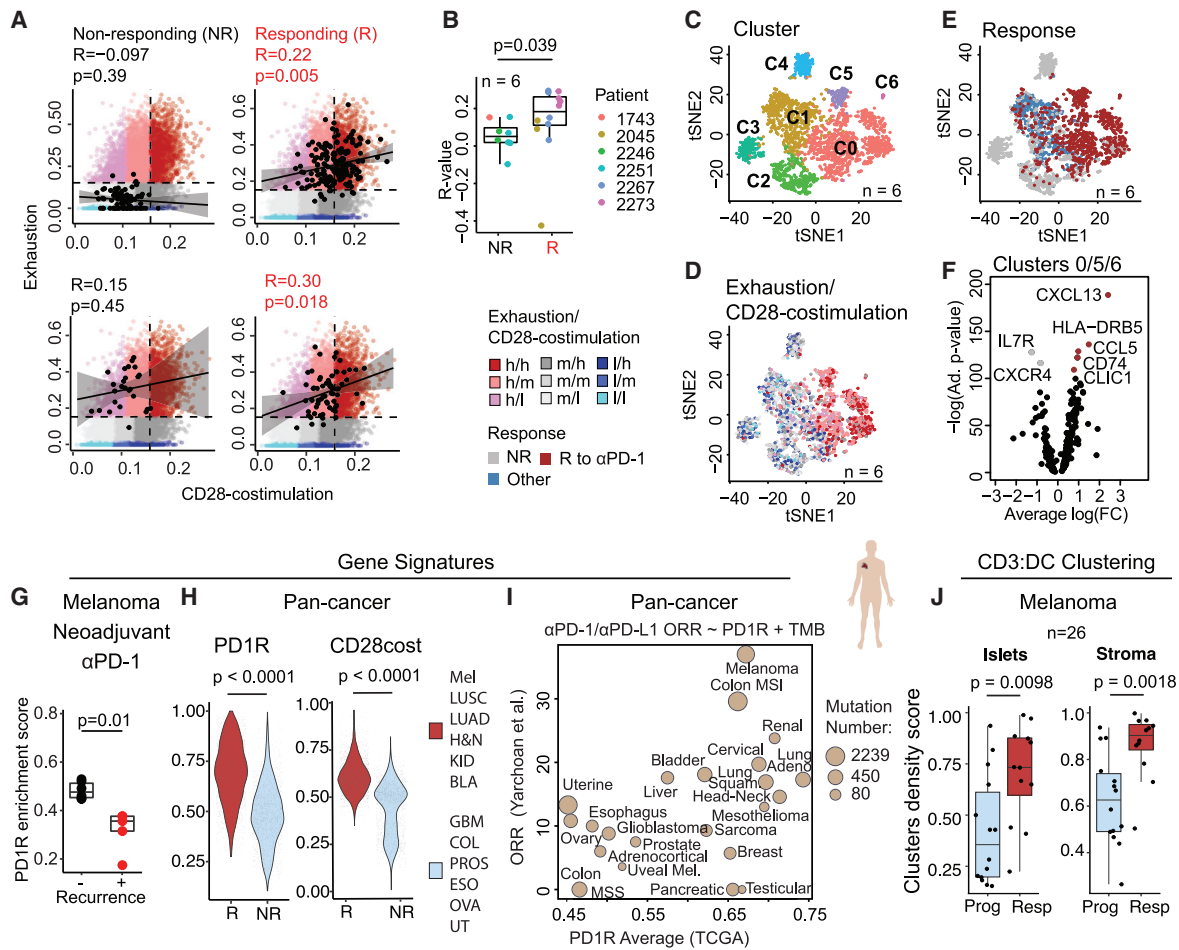


**Figure 7. CD28-costimulated exhausted TIL and proximity to tumor APC is associated with response to  $\alpha$ PD-1 in solid tumors**

(A–F) Exhaustion (Tex) and CD28-costimulation (CD28cost) states at baseline of clonally expanded CD8<sup>+</sup> TIL in HGSOc tumor-digest cultures that exhibited response (or not) to ICB *ex vivo*. (A) Pearson correlation of Tex and CD28cost states inferred by scRNA-seq in specific TIL clonotypes from representative samples (black dots) against a backdrop of all oligoclonal CD8<sup>+</sup> TIL ( $\geq 10$  cells/TCR) analyzed in all samples. (B) Cumulative data per patient for  $\geq 50$  cells/TCR (h = high, m = mid, l = low; R to  $\alpha$ PD-1: response to at least  $\alpha$ PD-1; Other: response to  $\alpha$ PD-1/ $\alpha$ CTLA-4 but not  $\alpha$ PD-1; NR: response to neither). (C) t-Distributed stochastic neighbor embedding depiction of unsupervised clusters, all clonotypes with  $\geq 50$  cells/TCR. (D) Distribution of TexCD28cost states. (E) *Ex vivo* responses of the same. (F) Differentially expressed genes between clusters 0/5/6 and other clusters.

(G) Enrichment of the five-gene PD-1 response (PD1R) signature at baseline in tumors that did not relapse ( $n = 8$ ) compared with tumors that relapsed ( $n = 5$ ) in an  $\alpha$ PD-1 neoadjuvant study in resectable melanoma patients (Huang et al., 2019).

(H) PD1R and CD28cost signatures in TCGA data, in cancer types known to respond (R) or not (NR) to  $\alpha$ PD-1 therapy.

(I) Correlation between average objective response rate (ORR) to  $\alpha$ PD-1 or  $\alpha$ PD-L1 monotherapy according to published assignments (Yarchoan et al., 2017) and expression levels of PD1R signature in TCGA data. Diameter of the bubble is proportional to tumor mutation burden (TMB).

(J) Frequency of CD11<sup>+</sup> cells with at least one CD3<sup>+</sup> cell neighbor ( $\leq 20 \mu\text{m}$  radius) normalized by the total CD11<sup>+</sup> cells in melanoma tumor islets versus stroma. Statistical tests: t test or as indicated. box plots defined as box (median and first and third quartiles) and whisker (extreme value). See also Figure S7 and Table S6.

fitness, endowed with more molecules required for bioenergetic function, homing, migration, organization of the immunological synapse, TCR signaling, chemokine production, IFN $\gamma$  expression, and cytolytic capacity, but also proliferation, survival, IL-2 signaling, and memory.

Furthermore, we show that intraepithelial mAPC niches provide critical CD28 costimulation signals that likely sustain ieTIL in the Tex<sup>hi</sup>CD28cost<sup>hi</sup> state, countering terminal exhaustion. Canonical DC that can process and cross-present antigens are likely the key actors in this crosstalk (Oh et al., 2020), but macrophages may also be implicated as they exhibit remarkable plasticity (Izar et al., 2020) and APC potential (Adams et al., 2020), and were

regularly found in the mAPC niches. Remarkably, mAPC niches are organized within tumor nests, most likely due to activation of specific chemokine networks (Dangaj et al., 2019). As a result, polyfunctional ieCD8<sup>+</sup> TIL are embedded in the mAPC niches while simultaneously engaging tumor cells, suggesting that the myeloid niche supports their effector fitness. Conversely, solitary PD-1<sup>+</sup>CD8<sup>+</sup> TIL are more likely to reach dysfunctional Tex *in situ* due to the absence of CD28 costimulatory cues. Overall the above observations allow us to reinterpret cell dysfunction associated with phenotypic exhaustion as the convergence of persistent TCR activation and insufficient CD28 costimulation. Such cells reach terminal dysfunction in the TME.

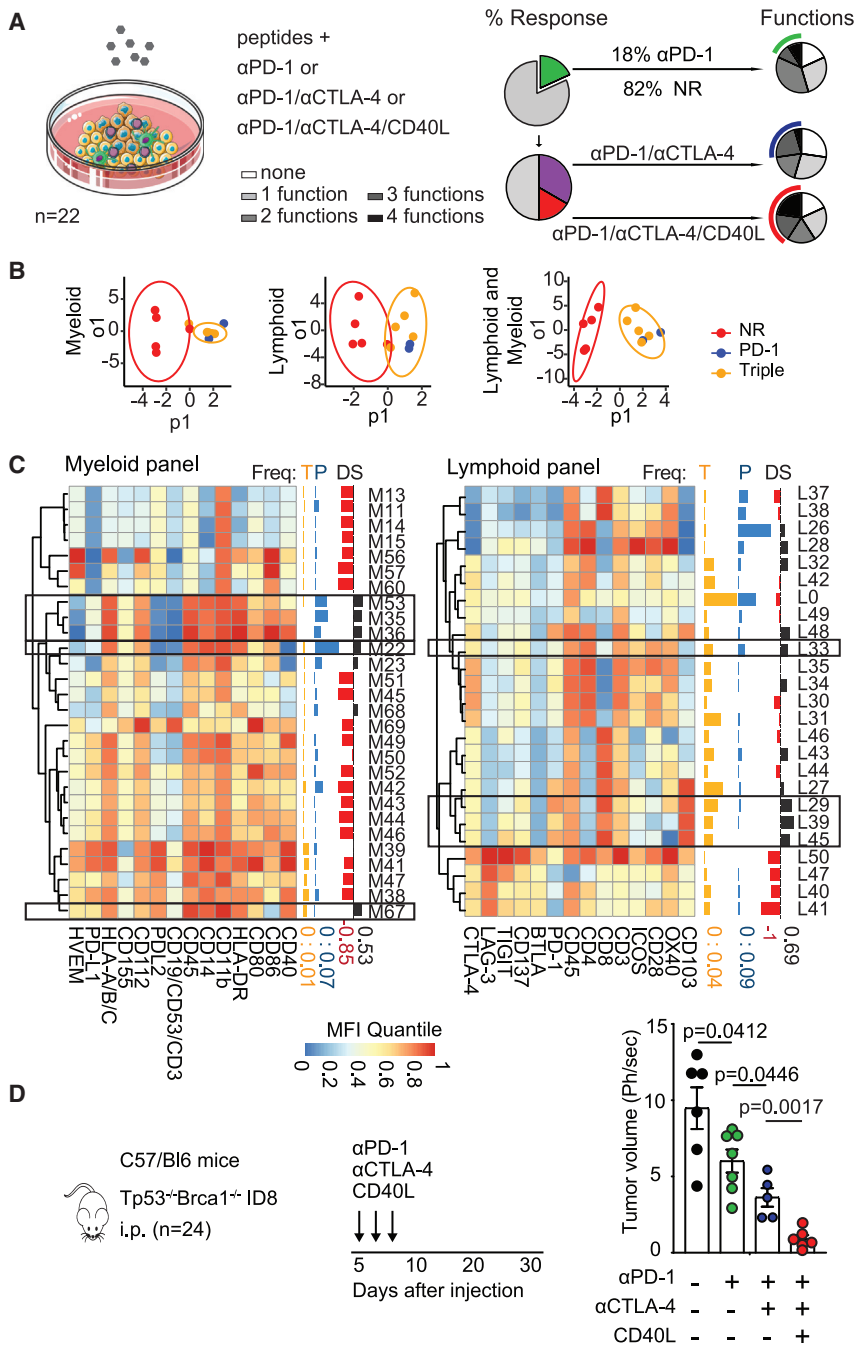


**Figure 8. Response to αPD-1 is amplified by CD40 agonist**

(A) Left: experimental setup. Right: response of tumor-digest cultures to peptide stimulation plus single or combinational ICB. Response was defined as proliferation plus  $\geq 2$  functions. Left pies: fraction of tumors responding to treatment; right pies: number of functions in CD8<sup>+</sup> TIL; response is indicated by arcs.

(B) Orthogonal projections to latent structures discriminant analysis of myeloid (CD11b<sup>+</sup>), lymphoid (CD3<sup>+</sup>), and combined myeloid/lymphoid FACS (14-parameter) panels discriminate non-responding (NR) tumors from those responding to αPD-1 versus triple αPD-1/αCTLA-4/CD40L.

(C) Clustering analysis of myeloid and lymphoid cells. Each row represents a cell subset based on phenotypes identified by MegaClust via unbiased analysis of FACS parameters of all cells. Side bars represent the average relative frequency for each cell subset at baseline in tumor-digest cultures that respond *ex vivo* to triple αPD-1/αCTLA-4/CD40L (T = yellow) or single αPD-1 treatment (P = blue), and their normalized discriminant score (DS; positive = black; negative = red).

(D) Best *in vivo* response to combinatorial ICB in C57BL/6 mice bearing *Tp53*<sup>-/-</sup>*Brca1*<sup>-/-</sup> ID8 tumors (mean ± SD, t test).

See also Figure S8 and Table S7.

TIL benefit from αPD-1 because this simultaneously strengthens TCR signaling while releasing the break on CD28 costimulation, thus enabling proper TIL activation and promoting TIL survival, proliferation, and, ultimately, clonal activation. Conversely, solitary niche-less exhausted TIL would respond to αPD-1 solely by strengthening TCR signaling but potentially undergoing activation-induced cell death in the absence of CD28 costimulation signals. This could explain the lack of clinical response in many tumors with pre-existing TIL as well as the clonal replacement observed during αPD-1 by us *in vitro* and by others *in vivo* (Yost et al., 2019).

Combining αPD-1 with αCTLA-4 may engage not only additive effects of CD28 coreceptors *in situ*, but also activate

While our study did not test directly p2TA binding on CD28, we inferred computationally its ability to inhibit CD28 dimerization and used it to show in human TIL the dependence of αPD-1 response on the availability of CD28 costimulation. We further showed the CD28 requirement for effective PD-1 blockade via orthogonal approaches and revealed the key role of tumor-resident mAPC. In a cell-free reconstitution system and in the Jurkat T cell line, CD28 is a preferred target of PD-1 (Hui et al., 2017), although PD-1 targets both CD28 and several components of the TCR signaling pathway (Sheppard et al., 2004), confirming previous evidence of a direct effect of PD-1 on the TCR (Mizuno et al., 2019; Wei et al., 2013). We postulate that niche-embedded

mTOR (Colombetti et al., 2006), which triggers glycolysis and maintains T cell response upon antigen persistence (Uttschneider et al., 2016). CD28 signaling also upregulates T-bet in antigen-stimulated CD8<sup>+</sup> T cells (Rao et al., 2010), a central regulator preventing transition of cells to terminal exhaustion (Beltra et al., 2020). We saw T-bet upregulation as well as proliferation of select clones *in situ* upon double blockade, which likely contributes to the expansion of αPD-1 response-associated Tex<sup>hi</sup>CD28cost<sup>hi</sup> pool, similarly to precursor Tex cells (Kurtulus et al., 2019).

Tex<sup>hi</sup>/CD28cost<sup>hi</sup> pool expansion was further enhanced by the addition of CD40L, which served to amplify the effects of ICB or

rescue response to ICB in the absence of pre-existing APC activation at the steady state. In addition to upregulating CD28, APC activation by CD40L may trigger further costimulatory signals and cytokines *in situ* including IL-12, which has the potential to further strengthen effector fitness (Kusaba et al., 2005; Schurich et al., 2013). Nevertheless, even though the cognate receptors were coexpressed by CD28-costimulated TIL, the addition of OX40 or CD137 agonists to  $\alpha$ PD-1 did not induce TIL activation as effectively as the addition of  $\alpha$ CTLA-4 in our culture system (not shown), highlighting the central role of the CD28 pathway. CD40 agonists can also reduce myeloid-derived suppressor cells (Liljenfeldt et al., 2014) and attenuate regulatory T cells (Schiza et al., 2017), expanding the beneficial effects on anti-tumor immunity. Finally, it should be noted that although here we focus largely on CD8<sup>+</sup> TIL, cytolytic CD4<sup>+</sup> TIL may also play an important role in tumor attack (Cachot et al., 2021), and properly activated CD4<sup>+</sup> helper cells could be the relevant physiological source of CD40L in tumors where APC are properly licensed at the steady state (Ferris et al., 2020).

## STAR★METHODS

Detailed methods are provided in the online version of this paper and include the following:

- **KEY RESOURCES TABLE**
- **RESOURCE AVAILABILITY**
  - Lead contact
  - Materials availability
  - Data and code availability
- **EXPERIMENTAL MODEL AND SUBJECT DETAILS**
  - Tumor and peripheral blood mononuclear cell samples
  - Cell lines and primary cultures
  - *In vivo* animal studies
- **METHOD DETAILS**
  - Fresh vs. frozen usage of samples
  - Cytolytic assay with NY-ESO-1 specific TIL and ovarian cancer cell line with ectopic expression of CD80/CD86
  - Syngeneic model of ovarian cancer and ex-vivo functional assays
  - Xenograft models of ovarian cancer
  - Preparation of HIS-NSG mice
  - Multispectral immunofluorescence (mIF) microscopy
  - Cyclic immunofluorescence in high-resolution imaging
  - Choice of antigen specificity for the evaluation of ovarian cancer TIL (directed against tumor associate antigens)
  - Flow cytometry
  - Time-of-flight mass cytometry (CyTOF)
  - Tumor digest cultures and TIL stimulation
  - APC depletion and disruption of CD28 costimulation
  - p2TA (AB103) peptide hypothetical mechanism of action
  - Functional analysis of fresh TIL or TIL from tumor digest cultures
  - Kinetic of expression of CD28 and phosphorylated ERK
  - TCR sequencing and analysis

- Single cell (sc)RNAseq
- Gene signatures
- Survival and gene expression analyses
- Public gene expression data correlation with response to  $\alpha$ PD-1 treatment
- MegaClust analysis
- Graphical illustrations

## ● QUANTIFICATION AND STATISTICAL ANALYSES

### SUPPLEMENTAL INFORMATION

Supplemental information can be found online at <https://doi.org/10.1016/j.ccell.2021.10.008>.

### ACKNOWLEDGMENTS

The study was supported by NIH grants P50 CA083638 SPORE in Ovarian Cancer, R01-CA116779, R01-CA098951; U54-CA225088; the Ludwig Institute for Cancer Research; grants from the Ovarian Cancer Research Alliance, Sidney Kimmel Foundation, Cancera Foundation, Mats Paulsson Foundation (all to G.C.); by NIH grant U54-CA225088 (to P.K.S.); and by RO1EB026892 grant (to D.J.P.). We thank Danny Labes from FCF@UNIL for performing the cell sorting for the scRNA-seq, and Michel A. Cuendet and Ekaterina Fortis for assisting with the melanoma cohort staining.

### AUTHOR CONTRIBUTIONS

Conceptualization, G.C.; supervision, G.C., M.A.D., and D.D.L.; methodology, G.C., J.D., M.A.D., R.T., D.D.L., A. Minasyan, S.R., P.G.F., P.K.S., and W.C.; validation, G.C., D.D.L., and M.A.D.; writing, G.C., P.K.S., D.D.L., A. Minasyan, R.T., M.A.D., D.B., I.C., J.C., A.F., and R.G.; analysis, G.C., J.D., R.T., A. Minasyan, J.C., A.F., S.J.C., K.I., A.J.G., D.B., I.C., F.B., A.W., R.G., M.A.E., W.C., V.Z., P.G.F., M.D., S.R., D.J.P.J., I.M.S., and C.A.J.; investigation, J.D., R.T., A. Minasyan, K.I., A.W., W.C., C.N., P.G.F., A.J.G., A. Moriot, S.R.-T., N.F., V.A., M.A.E., M.C.W.W., and I.M.S.; resources, J.L.T., D.D.L., K.T.M., M.A.E., L.E.K., and O.M.

### DECLARATION OF INTERESTS

G.C. has received grants from Celgene, Boehringer-Ingelheim, BMS, and Tigen, and participated in advisory board or presented at Roche, MSD Merck, BMS, AstraZeneca, and Geneos Tx-sponsored symposia (fees received by G.C.'s institution). G.C. has patents in the domain of antibodies, vaccines, T cell expansion, and engineering technologies, and receives royalties from UPenn. P.K.S. is a member of the SAB or Board of Directors of Applied Biomath, Glencoe Software, RareCyte Inc., and has equities in these companies; he is a member of the SAB of NanoString Inc. and a consultant for Merck and Montai Health. P.K.S. has received research funding from Novartis and Merck. D.J.P. receives research funding from Incyte and serves as an adviser, receives fees, stock options, and research funding from InsTIL Bio. R.G. holds a patent for TCR sequencing. J.D. is presently a US FDA employee. R.T., C.N., V.A., and M.A.D. are current employees of Ichnos Sciences Biotherapeutics SA. None of the above declared relationships has influenced the content of this manuscript. The other authors declare no competing financial interests.

Received: December 2, 2020

Revised: July 6, 2021

Accepted: October 15, 2021

Published: November 4, 2021

### REFERENCES

Adams, S.F., Grimm, A.J., Chiang, C.L., Mookerjee, A., Flies, D., Jean, S., McCann, G.A., Michaux, J., Pak, H., Huber, F., et al. (2020). Rapid tumor vaccine using Toll-like receptor-activated ovarian cancer ascites monocytes. *J. Immunother. Cancer* 8, e000875.

- Aibar, S., González-Blas, C.B., Moerman, T., Huynh-Thu, V.A., Imrichova, H., Hulselmans, G., Rambow, F., Marine, J.C., Geurts, P., Aerts, J., et al. (2017). SCENIC: single-cell regulatory network inference and clustering. *Nat. Methods* **14**, 1083–1086.
- Amir el, A.D., Davis, K.L., Tadmor, M.D., Simonds, E.F., Levine, J.H., Bendall, S.C., Shenfeld, D.K., Krishnaswamy, S., Nolan, G.P., and Pe'er, D. (2013). viSNE enables visualization of high dimensional single-cell data and reveals phenotypic heterogeneity of leukemia. *Nat. Biotechnol.* **31**, 545–552.
- Anderson, K.G., Voillet, V., Bates, B.M., Chiu, E.Y., Burnett, M.G., Garcia, N.M., Oda, S.K., Morse, C.B., Stromnes, I.M., Drescher, C.W., et al. (2019). Engineered adoptive T-cell therapy prolongs survival in a preclinical model of advanced-stage ovarian cancer. *Cancer Immunol. Res.* **7**, 1412–1425.
- Andrews, S. (2010). FastQC: A Quality Control Tool for High Throughput Sequence Data. <https://www.scienceopen.com/document?vid=de674375-ab83-4595-afa9-4c8aa9e4e736>.
- Arad, G., Levy, R., Nasie, I., Hillman, D., Rotfogel, Z., Barash, U., Supper, E., Shpilka, T., Minis, A., and Kaempfer, R. (2011). Binding of superantigen toxins into the CD28 homodimer interface is essential for induction of cytokine genes that mediate lethal shock. *Plos Biol.* **9**, e1001149.
- Ascierto, M.L., Makohon-Moore, A., Lipson, E.J., Taube, J.M., McMiller, T.L., Berger, A.E., Fan, J., Kaunitz, G.J., Cottrell, T.R., Kohutek, Z.A., et al. (2017). Transcriptional mechanisms of resistance to anti-PD-1 therapy. *Clin. Cancer Res.* **23**, 3168–3180.
- Ayers, M., Lunceford, J., Nebozhyn, M., Murphy, E., Loboda, A., Kaufman, D.R., Albright, A., Cheng, J.D., Kang, S.P., Shankaran, V., et al. (2017). IFN-gamma-related mRNA profile predicts clinical response to PD-1 blockade. *J. Clin. Invest.* **127**, 2930–2940.
- Azizi, E., Carr, A.J., Pliatas, G., Cornish, A.E., Konopacki, C., Prabhakaran, S., Nainys, J., Wu, K., Kiseliovas, V., Setty, M., et al. (2018). Single-cell map of diverse immune phenotypes in the breast tumor microenvironment. *Cell* **174**, 1293–1308.e36.
- Baitsch, L., Baumgaertner, P., Devevre, E., Raghav, S.K., Legat, A., Barba, L., Wieckowski, S., Bouzourene, H., Deplancke, B., Romero, P., et al. (2011). Exhaustion of tumor-specific CD8(+) T cells in metastases from melanoma patients. *J. Clin. Invest.* **121**, 2350–2360.
- Beltra, J.C., Manne, S., Abdel-Hakeem, M.S., Kurachi, M., Giles, J.R., Chen, Z., Casella, V., Ngiew, S.F., Khan, O., Huang, Y.J., et al. (2020). Developmental relationships of four exhausted CD8(+) T cell subsets reveals underlying transcriptional and epigenetic landscape control mechanisms. *Immunity* **52**, 825–841.e8.
- Bentink, S., Haibe-Kains, B., Risch, T., Fan, J.B., Hirsch, M.S., Holton, K., Rubio, R., April, C., Chen, J., Wickham-Garcia, E., et al. (2012). Angiogenic mRNA and microRNA gene expression signature predicts a novel subtype of serous ovarian cancer. *PLoS One* **7**, e30269.
- Bindea, G., Mlecnik, B., Tosolini, M., Kirilovsky, A., Waldner, M., Obenauf, A.C., Angell, H., Fredriksen, T., Lafontaine, L., Berger, A., et al. (2013). Spatiotemporal dynamics of intratumoral immune cells reveal the immune landscape in human cancer. *Immunity* **39**, 782–795.
- Blackburn, S.D., Shin, H., Freeman, G.J., and Wherry, E.J. (2008). Selective expansion of a subset of exhausted CD8 T cells by alphaPD-L1 blockade. *Proc. Natl. Acad. Sci. U. S. A.* **105**, 15016–15021.
- Bobisse, S., Genolet, R., Roberti, A., Tanyi, J.L., Racle, J., Stevenson, B.J., Iseli, C., Michel, A., Le Bitoux, M.A., Guillaume, P., et al. (2018). Sensitive and frequent identification of high avidity neo-epitope specific CD8 (+) T cells in immunotherapy-naïve ovarian cancer. *Nat. Commun.* **9**, 1092.
- Brickey, W.J., Wright, K.L., Zhu, X.S., and Ting, J.P. (1999). Analysis of the defect in IFN-gamma induction of MHC class II genes in G1B cells: identification of a novel and functionally critical leucine-rich motif (62-LYLYLQL-68) in the regulatory factor X 5 transcription factor. *J. Immunol.* **163**, 6622–6630.
- Broad Institute of MIT and Harvard (2016). Broad Institute TCGA Genome Data Analysis Center: Firehose 2016\_01\_28 Run. <https://gdac.broadinstitute.org/>.
- Bruand, M., Barras, D., Mina, M., Ghisoni, E., Morotti, M., Lanitis, E., Fahr, N., Desbuisson, M., Zhang, H., Chong, C., et al. (2021). Cell-autonomous inflammation of BRCA1-deficient ovarian cancers drives both tumor-intrinsic Immunoreactivity and immune resistance through STING. *Cell Rep.* **36**, 109412.
- Buckanovich, R.J., Sasaroli, D., O'Brien-Jenkins, A., Botbyl, J., Conejo-Garcia, J.R., Benencia, F., Liotta, L.A., Gimotty, P.A., and Coukos, G. (2006). Use of immuno-LCM to identify the in situ expression profile of cellular constituents of the tumor microenvironment. *Cancer Biol. Ther.* **5**, 635–642.
- Butler, A., Hoffman, P., Smibert, P., Papalexi, E., and Satija, R. (2018). Integrating single-cell transcriptomic data across different conditions, technologies, and species. *Nat. Biotechnol.* **36**, 411–420.
- Cachot, A., Bilous, M., Liu, Y.C., Li, X., Saillard, M., Cenerenti, M., Rockinger, G.A., Wyss, T., Guillaume, P., Schmidt, J., et al. (2021). Tumor-specific cytolytic CD4 T cells mediate immunity against human cancer. *Sci. Adv.* **7**, eabe3348.
- Chen, P.L., Roh, W., Reuben, A., Cooper, Z.A., Spencer, C.N., Prieto, P.A., Miller, J.P., Bassett, R.L., Gopalakrishnan, V., Wani, K., et al. (2016). Analysis of immune signatures in longitudinal tumor samples yields insight into biomarkers of response and mechanisms of resistance to immune checkpoint blockade. *Cancer Discov.* **6**, 827–837.
- Chen, Z., Ji, Z., Ngiew, S.F., Manne, S., Cai, Z., Huang, A.C., Johnson, J., Staup, R.P., Bengsch, B., Xu, C., et al. (2019). TCF-1-Centered transcriptional network drives an effector versus exhausted CD8 T cell-fate decision. *Immunity* **51**, 840–855.e5.
- Chu, C.S., Boyer, J., Schullery, D.S., Gimotty, P.A., Gamerman, V., Bender, J., Levine, B.L., Coukos, G., Rubin, S.C., Morgan, M.A., et al. (2012). Phase I/II randomized trial of dendritic cell vaccination with or without cyclophosphamide for consolidation therapy of advanced ovarian cancer in first or second remission. *Cancer Immunol. Immunother.* **61**, 629–641.
- Chu, C.S., Kim, S.H., June, C.H., and Coukos, G. (2008). Immunotherapy opportunities in ovarian cancer. *Expert Rev. Anticancer Ther.* **8**, 243–257.
- Chu, T., and Zehn, D. (2020). Charting the roadmap of T cell exhaustion. *Immunity* **52**, 724–726.
- Colombetti, S., Basso, V., Mueller, D.L., and Mondino, A. (2006). Prolonged TCR/CD28 engagement drives IL-2-independent T cell clonal expansion through signaling mediated by the mammalian target of rapamycin. *J. Immunol.* **176**, 2730–2738.
- Crijns, A.P., Fehrmann, R.S., de Jong, S., Gerbens, F., Meersma, G.J., Klip, H.G., Hollema, H., Hofstra, R.M., te Meerman, G.J., de Vries, E.G., et al. (2009). Survival-related profile, pathways, and transcription factors in ovarian cancer. *Plos Med.* **6**, e24.
- D'Angelo, S.P., Melchiori, L., Merchant, M.S., Bernstein, D., Glod, J., Kaplan, R., Grupp, S., Tap, W.D., Chagin, K., Binder, G.K., et al. (2018). Antitumor activity associated with prolonged persistence of adoptively transferred NY-ESO-1 (c259)T cells in synovial sarcoma. *Cancer Discov.* **8**, 944–957.
- Dammeijer, F., van Gulijk, M., Mulder, E.E., Lukkes, M., Klaase, L., van den Bosch, T., van Nimwegen, M., Lau, S.P., Latupeirissa, K., Schetters, S., et al. (2020). The PD-1/PD-L1-checkpoint restrains T cell immunity in tumor-draining lymph nodes. *Cancer Cell* **38**, 685–700.e8.
- Dangaj, D., Bruand, M., Grimm, A.J., Ronet, C., Barras, D., Dutttagupta, P.A., Lanitis, E., Duraiswamy, J., Tanyi, J.L., Benencia, F., et al. (2019). Cooperation between constitutive and inducible chemokines enables T cell engraftment and immune attack in solid tumors. *Cancer Cell* **35**, 885–900.e10.
- Daud, A.I., Loo, K., Pauli, M.L., Sanchez-Rodriguez, R., Sandoval, P.M., Taravati, K., Tsai, K., Nosrati, A., Nardo, L., Alvarado, M.D., et al. (2016). Tumor immune profiling predicts response to anti-PD-1 therapy in human melanoma. *J. Clin. Invest.* **126**, 3447–3452.
- Dunkle, A., Dzhagalov, I., Gordy, C., and He, Y.W. (2013). Transfer of CD8<sup>+</sup> T cell memory using Bcl-2 as a marker. *J. Immunol.* **190**, 940–947.
- Duraiswamy, J., Kaluza, K.M., Freeman, G.J., and Coukos, G. (2013). Dual blockade of PD-1 and CTLA-4 combined with tumor vaccine effectively restores T-cell rejection function in tumors. *Cancer Res.* **73**, 3591–3603.
- Faget, J., Groeneveld, S., Boivin, G., Sankar, M., Zangger, N., Garcia, M., Guex, N., Zlobec, I., Steiner, L., Piersigilli, A., et al. (2017). Neutrophils and snail orchestrate the establishment of a pro-tumor microenvironment in lung cancer. *Cell Rep.* **21**, 3190–3204.

- Färkkilä, A., Gulhan, D.C., Casado, J., Jacobson, C.A., Nguyen, H., Kochupurakkal, B., Maliga, Z., Yapp, C., Chen, Y.A., Schapiro, D., et al. (2020). Immunogenomic profiling determines responses to combined PARP and PD-1 inhibition in ovarian cancer. *Nat. Commun.* *11*, 1459.
- Fend, F., Emmert-Buck, M.R., Chuaqui, R., Cole, K., Lee, J., Liotta, L.A., and Raffeld, M. (1999). Immuno-LCM: laser capture microdissection of immunostained frozen sections for mRNA analysis. *Am. J. Pathol.* *154*, 61–66.
- Ferris, S.T., Durai, V., Wu, R., Theisen, D.J., Ward, J.P., Bern, M.D., Davidson, J.T.t., Bagadia, P., Liu, T., Briseño, C.G., et al. (2020). cDC1 prime and are licensed by CD4(+) T cells to induce anti-tumour immunity. *Nature* *584*, 624–629.
- Ferriss, J.S., Kim, Y., Duska, L., Birrer, M., Levine, D.A., Moskaluk, C., Theodorescu, D., and Lee, J.K. (2012). Multi-gene expression predictors of single drug responses to adjuvant chemotherapy in ovarian carcinoma: predicting platinum resistance. *PLoS One* *7*, e30550.
- Galindo-Prieto, B., Eriksson, L., and Trygg, J. (2014). Variable influence on projection (VIP) for orthogonal projections to latent structures (OPLS). *J. Chemom.* *28*, 623–632.
- Ganzfried, B.F., Riester, M., Haibe-Kains, B., Risch, T., Tyekucheva, S., Jazic, I., Wang, X.V., Ahmadifar, M., Birrer, M.J., Parmigiani, G., et al. (2013). curatedOvarianData: clinically annotated data for the ovarian cancer transcriptome. *Database J. Biol. Databases Curation* *2013*, bat013.
- Garapati, P.V. (2008). Costimulation by the CD28 Family (Reactome, release#71). <https://reactome.org/content/detail/R-HSA-388841>.
- Geng, Y., Shao, Y., He, W., Hu, W., Xu, Y., Chen, J., Wu, C., and Jiang, J. (2015). Prognostic role of tumor-infiltrating lymphocytes in lung cancer: a meta-analysis. *Cell Physiol. Biochem. Int. J. Exp. Cell. Physiol. Biochem. Pharmacol.* *37*, 1560–1571.
- Gentric, G., Kieffer, Y., Mieulet, V., Goundiam, O., Bonneau, C., Nemati, F., Hurbain, I., Raposo, G., Popova, T., Stern, M.H., et al. (2019). PML-regulated mitochondrial metabolism enhances chemosensitivity in human ovarian cancers. *Cell Metab.* *29*, 156–173.e10.
- GitHub (2018). ASHLAR: alignment by simultaneous harmonization of layer/adjacency registration. <https://github.com/labsyspharm/ashlar>.
- Gjerdrum, L.M., Lielpetere, I., Rasmussen, L.M., Bendix, K., and Hamilton-Dutoit, S. (2001). Laser-assisted microdissection of membrane-mounted paraffin sections for polymerase chain reaction analysis: identification of cell populations using immunohistochemistry and in situ hybridization. *J. Mol. Diagn.* *3*, 105–110.
- Goode, E.L., Block, M.S., Kalli, K.R., Vierkant, R.A., Chen, W., Fogarty, Z.C., Gentry-Maharaj, A., Toloczko, A., Hein, A., Bouligny, A.L., et al. (2017). Dose-response association of CD8<sup>+</sup> tumor-infiltrating lymphocytes and survival time in high-grade serous ovarian cancer. *JAMA Oncol.* *3*, e173290.
- Greene, J.L., Leytze, G.M., Emswiler, J., Peach, R., Bajorath, J., Cosand, W., and Linsley, P.S. (1996). Covalent dimerization of CD28/CTLA-4 and oligomerization of CD80/CD86 regulate T cell costimulatory interactions. *J. Biol. Chem.* *271*, 26762–26771.
- Gritzapis, A.D., Mahaira, L.G., Perez, S.A., Cacoullos, N.T., Papamichail, M., and Baxevis, C.N. (2006). Vaccination with human HER-2/neu (435–443) CTL peptide induces effective antitumor immunity against HER-2/neu-expressing tumor cells in vivo. *Cancer Res.* *66*, 5452–5460.
- Gros, A., Robbins, P.F., Yao, X., Li, Y.F., Turcotte, S., Tran, E., Wunderlich, J.R., Mixon, A., Farid, S., Dudley, M.E., et al. (2014). PD-1 identifies the patient-specific CD8(+) tumor-reactive repertoire infiltrating human tumors. *J. Clin. Invest.* *124*, 2246–2259.
- Guo, X., Zhang, Y., Zheng, L., Zheng, C., Song, J., Zhang, Q., Kang, B., Liu, Z., Jin, L., Xing, R., et al. (2018). Global characterization of T cells in non-small-cell lung cancer by single-cell sequencing. *Nat. Med.* *24*, 978–985.
- Hänzelmann, S., Castelo, R., and Guinney, J. (2013). GSEA: gene set variation analysis for microarray and RNA-seq data. *BMC Bioinform.* *14*, 7.
- Herbst, R.S., Soria, J.C., Kowanetz, M., Fine, G.D., Hamid, O., Gordon, M.S., Sosman, J.A., McDermott, D.F., Powderly, J.D., Gettinger, S.N., et al. (2014). Predictive correlates of response to the anti-PD-L1 antibody MPDL3280A in cancer patients. *Nature* *515*, 563–567.
- Herrmann, C., Van de Sande, B., Potier, D., and Aerts, S. (2012). i-cisTarget: an integrative genomics method for the prediction of regulatory features and cis-regulatory modules. *Nucleic Acids Res.* *40*, e114.
- Holling, T.M., Schooten, E., and van Den Elsen, P.J. (2004). Function and regulation of MHC class II molecules in T-lymphocytes: of mice and men. *Hum. Immunol.* *65*, 282–290.
- Huang, A.C., Orłowski, R.J., Xu, X., Mick, R., George, S.M., Yan, P.K., Manne, S., Kraya, A.A., Wubbenhorst, B., Dorfman, L., et al. (2019). A single dose of neoadjuvant PD-1 blockade predicts clinical outcomes in resectable melanoma. *Nat. Med.* *25*, 454–461.
- Huang, R.Y., Francois, A., McGray, A.R., Milotto, A., and Odunsi, K. (2017). Compensatory upregulation of PD-1, LAG-3, and CTLA-4 limits the efficacy of single-agent checkpoint blockade in metastatic ovarian cancer. *Oncimmunology* *6*, e1249561.
- Hugo, W., Zaretsky, J.M., Sun, L., Song, C., Moreno, B.H., Hu-Lieskovan, S., Berent-Maoz, B., Pang, J., Chmielowski, B., Cherry, G., et al. (2016). Genomic and transcriptomic features of response to anti-PD-1 therapy in metastatic melanoma. *Cell* *165*, 35–44.
- Hui, E., Cheung, J., Zhu, J., Su, X., Taylor, M.J., Wallweber, H.A., Sasmal, D.K., Huang, J., Kim, J.M., Mellman, I., et al. (2017). T cell costimulatory receptor CD28 is a primary target for PD-1-mediated inhibition. *Science* *355*, 1428–1433.
- Hung, C.F., Tsai, Y.C., He, L., and Wu, T.C. (2007). Control of mesothelin-expressing ovarian cancer using adoptive transfer of mesothelin peptide-specific CD8<sup>+</sup> T cells. *Gene Ther.* *14*, 921–929.
- Huynh-Thu, V.A., Irrthum, A., Wehenkel, L., and Geurts, P. (2010). Inferring regulatory networks from expression data using tree-based methods. *PLoS One* *5*, e12776.
- Imrichová, H., Hulselmans, G., Atak, Z.K., Potier, D., and Aerts, S. (2015). i-cisTarget 2015 update: generalized cis-regulatory enrichment analysis in human, mouse and fly. *Nucleic Acids Res.* *43*, W57–W64.
- Izar, B., Tirosh, I., Stover, E.H., Wakiro, I., Cuoco, M.S., Alter, I., Rodman, C., Leeson, R., Su, M.J., Shah, P., et al. (2020). A single-cell landscape of high-grade serous ovarian cancer. *Nat. Med.* *26*, 1271–1279.
- Jansen, C.S., Prokhnevskaya, N., Master, V.A., Sanda, M.G., Carlisle, J.W., Bilen, M.A., Cardenas, M., Wilkinson, S., Lake, R., Sowalsky, A.G., et al. (2019). An intra-tumoral niche maintains and differentiates stem-like CD8 T cells. *Nature* *576*, 465–470.
- Jerby-Aron, L., Shah, P., Cuoco, M.S., Rodman, C., Su, M.J., Melms, J.C., Leeson, R., Kanodia, A., Mei, S., Lin, J.R., et al. (2018). A cancer cell program promotes T cell exclusion and resistance to checkpoint blockade. *Cell* *175*, 984–997.e24.
- Kaempfer, R., Popugailo, A., Levy, R., Arad, G., Hillman, D., and Rotfogel, Z. (2017). Bacterial superantigen toxins induce a lethal cytokine storm by enhancing B7-2/CD28 costimulatory receptor engagement, a critical immune checkpoint. *Receptors Clin Investig* *4*, e1500.
- Kamphorst, A.O., Wieland, A., Nasti, T., Yang, S., Zhang, R., Barber, D.L., Konieczny, B.T., Daugherty, C.Z., Koenig, L., Yu, K., et al. (2017). Rescue of exhausted CD8 T cells by PD-1-targeted therapies is CD28-dependent. *Science* *355*, 1423–1427.
- Khan, O., Giles, J.R., McDonald, S., Manne, S., Ngjow, S.F., Patel, K.P., Werner, M.T., Huang, A.C., Alexander, K.A., Wu, J.E., et al. (2019). TOX transcriptionally and epigenetically programs CD8(+) T cell exhaustion. *Nature* *571*, 211–218.
- Kim, K., Park, S., Park, S.Y., Kim, G., Park, S.M., Cho, J.W., Kim, D.H., Park, Y.M., Koh, Y.W., Kim, H.R., et al. (2020). Single-cell transcriptome analysis reveals TOX as a promoting factor for T cell exhaustion and a predictor for anti-PD-1 responses in human cancer. *Genome Med.* *12*, 22.
- Kolde, R. (2019). Pheatmap: Pretty Heatmaps. R Package Version 1.0.12. <https://rdrr.io/cran/pheatmap/>
- Kurachi, M., Barnitz, R.A., Yosef, N., Odorizzi, P.M., Dilorio, M.A., Lemieux, M.E., Yates, K., Godec, J., Klatt, M.G., Regev, A., et al. (2014). The transcription factor BATF operates as an essential differentiation checkpoint in early effector CD8<sup>+</sup> T cells. *Nat. Immunol.* *15*, 373–383.

- Kurtulus, S., Madi, A., Escobar, G., Klapholz, M., Nyman, J., Christian, E., Pawlak, M., Dionne, D., Xia, J., Rozenblatt-Rosen, O., et al. (2019). Checkpoint blockade immunotherapy induces dynamic changes in PD-1(-) CD8(+) tumor-infiltrating T cells. *Immunity* *50*, 181–194.e6.
- Kusaba, H., Ghosh, P., Derin, R., Buchholz, M., Sasaki, C., Madara, K., and Longo, D.L. (2005). Interleukin-12-induced interferon-gamma production by human peripheral blood T cells is regulated by mammalian target of rapamycin (mTOR). *J. Biol. Chem.* *280*, 1037–1043.
- Lee, H.S., Jang, H.J., Choi, J.M., Zhang, J., de Rosen, V.L., Wheeler, T.M., Lee, J.S., Tu, T., Jindra, P.T., Kerman, R.H., et al. (2018). Comprehensive immunoproteogenomic analyses of malignant pleural mesothelioma. *JCI insight* *3*, e98575.
- Levine, J.H., Simonds, E.F., Bendall, S.C., Davis, K.L., Amir el, A.D., Tadmor, M.D., Litvin, O., Fienberg, H.G., Jager, A., Zunder, E.R., et al. (2015). Data-driven phenotypic dissection of AML reveals progenitor-like cells that correlate with prognosis. *Cell* *162*, 184–197.
- Levy, R., Rotfogel, Z., Hillman, D., Popugailo, A., Arad, G., Supper, E., Osman, F., and Kaempfer, R. (2016). Superantigens hyperinduce inflammatory cytokines by enhancing the B7-2/CD28 costimulatory receptor interaction. *Proc. Natl. Acad. Sci. U S A* *113*, E6437–E6446.
- Liljenfeldt, L., Dieterich, L.C., Dimberg, A., Mangsbo, S.M., and Loskog, A.S. (2014). CD40L gene therapy tilts the myeloid cell profile and promotes infiltration of activated T lymphocytes. *Cancer Gene Ther.* *21*, 95–102.
- Lin, J.R., Izar, B., Wang, S., Yapp, C., Mei, S., Shah, P.M., Santagata, S., and Sorger, P.K. (2018). Highly multiplexed immunofluorescence imaging of human tissues and tumors using t-CyCIF and conventional optical microscopes. *eLife* *7*, e31657.
- Matsuzaki, J., Gnjatic, S., Mhawech-Fauceglia, P., Beck, A., Miller, A., Tsuji, T., Eppolito, C., Qian, F., Lele, S., Shrikant, P., et al. (2010). Tumor-infiltrating NY-ESO-1-specific CD8<sup>+</sup> T cells are negatively regulated by LAG-3 and PD-1 in human ovarian cancer. *Proc. Natl. Acad. Sci. U. S. A.* *107*, 7875–7880.
- Matulonis, U.A., Shapira-Frommer, R., Santin, A.D., Lisyanskaya, A.S., Pignata, S., Vergote, I., Raspagliesi, F., Sonke, G.S., Birrer, M., Provencher, D.M., et al. (2019). Antitumor activity and safety of pembrolizumab in patients with advanced recurrent ovarian cancer: results from the phase II KEYNOTE-100 study. *Ann. Oncol.* *30*, 1080–1087.
- Mayoux, M., Roller, A., Pulko, V., Samiceli, S., Chen, S., Sum, E., Jost, C., Fransen, M.F., Buser, R.B., Kovanetz, M., et al. (2020). Dendritic cells dictate responses to PD-L1 blockade cancer immunotherapy. *Sci. Transl. Med.* *12*, eaav7431.
- Miller, B.C., Sen, D.R., Al Abosy, R., Bi, K., Virkud, Y.V., LaFleur, M.W., Yates, K.B., Lako, A., Felt, K., Naik, G.S., et al. (2019). Subsets of exhausted CD8(+) T cells differentially mediate tumor control and respond to checkpoint blockade. *Nat. Immunol.* *20*, 326–336.
- Milner, J.J., Toma, C., Yu, B., Zhang, K., Omilusik, K., Phan, A.T., Wang, D., Getzler, A.J., Nguyen, T., Crotty, S., et al. (2017). Runx3 programs CD8<sup>+</sup> T cell residency in non-lymphoid tissues and tumours. *Nature* *552*, 253–257.
- Miyazaki, Y., Fujiwara, H., Asai, H., Ochi, T., Azuma, T., Ishida, T., Okamoto, S., Mineno, J., Kuzushima, K., et al. (2013). Development of a novel redirected T-cell-based adoptive immunotherapy targeting human telomerase reverse transcriptase for adult T-cell leukemia. *Blood* *121*, 4894–4901.
- Mizuno, R., Sugiura, D., Shimizu, K., Maruhashi, T., Watada, M., Okazaki, I.M., and Okazaki, T. (2019). PD-1 primarily targets TCR signal in the inhibition of functional T cell activation. *Front. Immunol.* *10*, 630.
- Mok, S.C., Bonome, T., Vathipadiekal, V., Bell, A., Johnson, M.E., Wong, K.K., Park, D.C., Hao, K., Yip, D.K., Donninger, H., et al. (2009). A gene signature predictive for outcome in advanced ovarian cancer identifies a survival factor: microfibril-associated glycoprotein 2. *Cancer Cell* *16*, 521–532.
- Nowicka, M., Krieg, C., Weber, L.M., Hartmann, F.J., Guglietta, S., Becher, B., Levesque, M.P., and Robinson, M.D. (2017). CyTOF workflow: differential discovery in high-throughput high-dimensional cytometry datasets. *F1000Research* *6*, 748.
- Odunsi, K., Matsuzaki, J., Karbach, J., Neumann, A., Mhawech-Fauceglia, P., Miller, A., Beck, A., Morrison, C.D., Ritter, G., Godoy, H., et al. (2012). Efficacy of vaccination with recombinant vaccinia and fowlpox vectors expressing NY-ESO-1 antigen in ovarian cancer and melanoma patients. *Proc. Natl. Acad. Sci. U. S. A.* *109*, 5797–5802.
- Odunsi, K., Qian, F., Matsuzaki, J., Mhawech-Fauceglia, P., Andrews, C., Hoffman, E.W., Pan, L., Ritter, G., Vilella, J., Thomas, B., et al. (2007). Vaccination with an NY-ESO-1 peptide of HLA class I/II specificities induces integrated humoral and T cell responses in ovarian cancer. *Proc. Natl. Acad. Sci. U. S. A.* *104*, 12837–12842.
- Oh, S.A., Wu, D.-C., Cheung, J., Navarro, A., Xiong, H., Cubas, R., Totpal, K., Chiu, H., Wu, Y., Comps-Agrar, L., et al. (2020). PD-L1 expression by dendritic cells is a key regulator of T-cell immunity in cancer. *Nat. Cancer* *1*, 681–691.
- Ohteki, T., Maki, C., and Koyasu, S. (2001). Overexpression of Bcl-2 differentially restores development of thymus-derived CD4-8+ T cells and intestinal intraepithelial T cells in IFN-regulatory factor-1-deficient mice. *J. Immunol.* *166*, 6509–6513.
- Pe'er, D. (2021). **CYT download page.** <https://dpeerlab.github.io/dpeerlab-website/cyt-download.html>.
- Peng, T., Thorn, K., Schroeder, T., Wang, L., Theis, F.J., Marr, C., and Navab, N. (2017). A BaSiC tool for background and shading correction of optical microscopy images. *Nat. Commun.* *8*, 14836.
- Pentcheva-Hoang, T., Egen, J.G., Wojnoonski, K., and Allison, J.P. (2004). B7-1 and B7-2 selectively recruit CTLA-4 and CD28 to the immunological synapse. *Immunity* *21*, 401–413.
- Pils, D., Hager, G., Tong, D., Aust, S., Heinze, G., Kohl, M., Schuster, E., Wolf, A., Sehouli, J., Braicu, I., et al. (2012). Validating the impact of a molecular subtype in ovarian cancer on outcomes: a study of the OVCAD Consortium. *Cancer Sci.* *103*, 1334–1341.
- Prat, A., Navarro, A., Paré, L., Reguart, N., Galván, P., Pascual, T., Martínez, A., Nuciforo, P., Comerma, L., Alos, L., et al. (2017). Immune-Related gene expression profiling after PD-1 blockade in non-small cell lung carcinoma, head and neck squamous cell carcinoma, and melanoma. *Cancer Res.* *77*, 3540–3550.
- Quigley, M., Huang, X., and Yang, Y. (2008). STAT1 signaling in CD8 T cells is required for their clonal expansion and memory formation following viral infection in vivo. *J. Immunol.* *180*, 2158–2164.
- R Core Team (2020). **R: A Language and Environment for Statistical Computing (R Foundation for Statistical Computing).** <https://www.R-project.org/>.
- Rao, R.R., Li, Q., Odunsi, K., and Shrikant, P.A. (2010). The mTOR kinase determines effector versus memory CD8<sup>+</sup> T cell fate by regulating the expression of transcription factors T-bet and Eomesodermin. *Immunity* *32*, 67–78.
- Redjimi, N., Duperrier-Amouriaux, K., Raimbaud, I., Luescher, I., Dojcinovic, D., Classe, J.M., Berton-Rigaud, D., Frenel, J.S., Bourbouloux, E., Valmori, D., et al. (2011). NY-ESO-1-specific circulating CD4<sup>+</sup> T cells in ovarian cancer patients are prevalently T(H)1 type cells undetectable in the CD25<sup>+</sup> FOXP3<sup>+</sup> Treg compartment. *PLoS One* *6*, e22845.
- Renard, V., Sonderbye, L., Ebbelø, K., Rasmussen, P.B., Gregorius, K., Gottschalk, T., Mouritsen, S., Gautam, A., and Leach, D.R. (2003). HER-2 DNA and protein vaccines containing potent Th cell epitopes induce distinct protective and therapeutic antitumor responses in HER-2 transgenic mice. *J. Immunol.* *171*, 1588–1595.
- Riaz, N., Havel, J.J., Makarov, V., Desrichard, A., Urba, W.J., Sims, J.S., Hodi, F.S., Martin-Algarra, S., Mandal, R., Sharfman, W.H., et al. (2017). Tumor and microenvironment evolution during immunotherapy with nivolumab. *Cell* *171*, 934–949.e16.
- Ritchie, M.E., Phipson, B., Wu, D., Hu, Y., Law, C.W., Shi, W., and Smyth, G.K. (2015). Limma powers differential expression analyses for RNA-sequencing and microarray studies. *Nucleic Acids Res.* *43*, e47.
- Robbins, P.F., Morgan, R.A., Feldman, S.A., Yang, J.C., Sherry, R.M., Dudley, M.E., Wunderlich, J.R., Nahvi, A.V., Helman, L.J., Mackall, C.L., et al. (2011). Tumor regression in patients with metastatic synovial cell sarcoma and melanoma using genetically engineered lymphocytes reactive with NY-ESO-1. *J. Clin. Oncol.* *29*, 917–924.
- Roh, W., Chen, P.L., Reuben, A., Spencer, C.N., Prieto, P.A., Miller, J.P., Gopalakrishnan, V., Wang, F., Cooper, Z.A., Reddy, S.M., et al. (2017).

Integrated molecular analysis of tumor biopsies on sequential CTLA-4 and PD-1 blockade reveals markers of response and resistance. *Sci. Transl. Med.* 9, eaah3560.

Ronneberger, O., Fischer, P., and Brox, T. (2015). U-net: convolutional networks for biomedical image segmentation. In *International Conference on Medical Image Computing and Computing-Assisted Intervention (MICCAI 2015)*, pp. 234–241.

Sade-Feldman, M., Yizhak, K., Bjorgaard, S.L., Ray, J.P., de Boer, C.G., Jenkins, R.W., Lieb, D.J., Chen, J.H., Frederick, D.T., Barzily-Rokni, M., et al. (2018). Defining T cell states associated with response to checkpoint immunotherapy in melanoma. *Cell* 175, 998–1013.e20.

Sade-Feldman, M., Yizhak, K., Bjorgaard, S.L., Ray, J.P., de Boer, C.G., Jenkins, R.W., Lieb, D.J., Chen, J.H., Frederick, D.T., Barzily-Rokni, M., et al. (2019). Defining T cell states associated with response to checkpoint immunotherapy in melanoma. *Cell* 176, 404.

Salmon, H., Idoyaga, J., Rahman, A., Leboeuf, M., Remark, R., Jordan, S., Casanova-Acebes, M., Khudoynazarova, M., Agudo, J., Tung, N., et al. (2016). Expansion and activation of CD103(+) dendritic cell progenitors at the tumor site enhances tumor responses to therapeutic PD-L1 and BRAF inhibition. *Immunity* 44, 924–938.

Sanchez-Lockhart, M., Rojas, A.V., Fettis, M.M., Bauserman, R., Higa, T.R., Miao, H., Waugh, R.E., and Miller, J. (2014). T cell receptor signaling can directly enhance the avidity of CD28 ligand binding. *PLoS One* 9, e89263.

Schapiro, D., Jackson, H.W., Raghuraman, S., Fischer, J.R., Zanotelli, V.R.T., Schulz, D., Giesen, C., Catena, R., Varga, Z., and Bodenmiller, B. (2017). histoCAT: analysis of cell phenotypes and interactions in multiplex image cytometry data. *Nat. Methods* 14, 873–876.

Scheper, W., Kelderman, S., Fanchi, L.F., Linnemann, C., Bendle, G., de Rooij, M.A.J., Hirt, C., Mezzadra, R., Slagter, M., Dijkstra, K., et al. (2019). Low and variable tumor reactivity of the intratumoral TCR repertoire in human cancers. *Nat. Med.* 25, 89–94.

Schiza, A., Wenhe, J., Mangsbo, S., Eriksson, E., Nilsson, A., Tötterman, T.H., Loskog, A., and Ullenhag, G. (2017). Adenovirus-mediated CD40L gene transfer increases T effector/T regulatory cell ratio and upregulates death receptors in metastatic melanoma patients. *J. Transl. Med.* 15, 79.

Schmidt, J., Guillaume, P., Irving, M., Baumgaertner, P., Speiser, D., and Luescher, I.F. (2011). Reversible major histocompatibility complex I-peptide multimers containing Ni(2+)-nitrilotriacetic acid peptides and histidine tags improve analysis and sorting of CD8(+) T cells. *J. Biol. Chem.* 286, 41723–41735.

Schurich, A., Pallett, L.J., Lubowiecki, M., Singh, H.D., Gill, U.S., Kennedy, P.T., Nastouli, E., Tanwar, S., Rosenberg, W., and Maini, M.K. (2013). The third signal cytokine IL-12 rescues the anti-viral function of exhausted HBV-specific CD8 T cells. *Plos Pathog.* 9, e1003208.

Schwartz, J.C., Zhang, X., Fedorov, A.A., Nathenson, S.G., and Almo, S.C. (2001). Structural basis for co-stimulation by the human CTLA-4/B7-2 complex. *Nature* 410, 604–608.

Schymkowitz, J., Borg, J., Stricher, F., Nys, R., Rousseau, F., and Serrano, L. (2005). The FoldX web server: an online force field. *Nucleic Acids Res.* 33, W382–W388.

Seitz, C., Huang, J., Geiselhöringer, A.L., Galbani-Bianchi, P., Michalek, S., Phan, T.S., Reinhold, C., Dietrich, L., Schmidt, C., Corazza, N., et al. (2019). The orphan nuclear receptor LRR-1/NR5a2 critically regulates T cell functions. *Sci. Adv.* 5, eaav9732.

Sheppard, K.A., Fitz, L.J., Lee, J.M., Benander, C., George, J.A., Wooters, J., Qiu, Y., Jussif, J.M., Carter, L.L., Wood, C.R., et al. (2004). PD-1 inhibits T-cell receptor induced phosphorylation of the ZAP70/CD3zeta signalosome and downstream signaling to PKCtheta. *FEBS Lett.* 574, 37–41.

Shirvan, A., Bulger, E., and Danker, W. (2018). Reltecomod. T-cell-specific surface glycoprotein CD28 (TP44) antagonist, CD28 homodimer interface mimetic peptide, Treatment of necrotizing soft-tissue infection. *Drugs of the Future* 43, 243.

Siddiqui, I., Schaeuble, K., Chennupati, V., Fuentes Marraco, S.A., Calderon-Copete, S., Pais Ferreira, D., Carmona, S.J., Scarpellino, L., Gfeller, D.,

Pradervand, S., et al. (2019). Intratumoral Tcf1(+)PD-1(+)CD8(+) T cells with stem-like properties promote tumor control in response to vaccination and checkpoint blockade immunotherapy. *Immunity* 50, 195–211.e10.

Sørensen, P., Kussmann, M., Rosén, A., Bennett, K.L., Thrige Dda, G., Uvebrant, K., Walse, B., Roepstorff, P., and Björk, P. (2004). Identification of protein-protein interfaces implicated in CD80-CD28 costimulatory signaling. *J. Immunol.* 172, 6803–6809.

Speiser, D.E., Migliaccio, M., Pittet, M.J., Valmori, D., Liénard, D., Lejeune, F., Reichenbach, P., Guillaume, P., Lüscher, I., Cerottini, J.C., et al. (2001). Human CD8(+) T cells expressing HLA-DR and CD28 show telomerase activity and are distinct from cytolytic effector T cells. *Eur. J. Immunol.* 31, 459–466.

Stuart, T., Butler, A., Hoffman, P., Hafemeister, C., Papalexi, E., Mauck, W.M., 3rd, Hao, Y., Stoeckius, M., Smibert, P., and Satija, R. (2019). Comprehensive integration of single-cell data. *Cell* 177, 1888–1902.e21.

Thévenot, E.A., Roux, A., Xu, Y., Ezan, E., and Junot, C. (2015). Analysis of the human adult urinary metabolome variations with age, body mass index, and gender by implementing a comprehensive workflow for univariate and OPLS statistical analyses. *J. Proteome Res.* 14, 3322–3335.

Thommen, D.S., Koelzer, V.H., Herzig, P., Roller, A., Trefny, M., Dimeloe, S., Kiialainen, A., Hanhart, J., Schill, C., Hess, C., et al. (2018). A transcriptionally and functionally distinct PD-1(+) CD8(+) T cell pool with predictive potential in non-small-cell lung cancer treated with PD-1 blockade. *Nat. Med.* 24, 994–1004.

Tirosh, I., Izar, B., Prakadan, S.M., Wadsworth, M.H., 2nd, Treacy, D., Trombetta, J.J., Rotem, A., Rodman, C., Lian, C., Murphy, G., et al. (2016). Dissecting the multicellular ecosystem of metastatic melanoma by single-cell RNA-seq. *Science* 352, 189–196.

Tothill, R.W., Tinker, A.V., George, J., Brown, R., Fox, S.B., Lade, S., Johnson, D.S., Trivett, M.K., Etemadmoghadam, D., Locandro, B., et al. (2008). Novel molecular subtypes of serous and endometrioid ovarian cancer linked to clinical outcome. *Clin. Cancer Res. : official J. Am. Assoc. Cancer Res.* 14, 5198–5208.

Tumeh, P.C., Harview, C.L., Yearley, J.H., Shintaku, I.P., Taylor, E.J., Robert, L., Chmielowski, B., Spasic, M., Henry, G., Ciobanu, V., et al. (2014). PD-1 blockade induces responses by inhibiting adaptive immune resistance. *Nature* 515, 568–571.

Utzuschneider, D.T., Alfei, F., Roelli, P., Barras, D., Chennupati, V., Darbre, S., Delorenzi, M., Pinschewer, D.D., and Zehn, D. (2016). High antigen levels induce an exhausted phenotype in a chronic infection without impairing T cell expansion and survival. *J. Exp. Med.* 213, 1819–1834.

van der Leun, A.M., Thommen, D.S., and Schumacher, T.N. (2020). CD8(+) T cell states in human cancer: insights from single-cell analysis. *Nat. Rev. Cancer* 20, 218–232.

Wagner, J., Rapsomaniki, M.A., Chevrier, S., Anzeneder, T., Langwieder, C., Dykgers, A., Rees, M., Ramaswamy, A., Muenst, S., Soysal, S.D., et al. (2019). A single-cell atlas of the tumor and immune ecosystem of human breast cancer. *Cell* 177, 1330–1345.e18.

Walton, J.B., Farquharson, M., Mason, S., Port, J., Kruspig, B., Dowson, S., Stevenson, D., Murphy, D., Matzuk, M., Kim, J., et al. (2017). CRISPR/Cas9-derived models of ovarian high grade serous carcinoma targeting Brca1, Pten and Nf1, and correlation with platinum sensitivity. *Sci. Rep.* 7, 16827.

Wang, B., Zhang, W., Jankovic, V., Golubov, J., Poon, P., Oswald, E.M., Gurer, C., Wei, J., Ramos, I., Wu, Q., et al. (2018). Combination cancer immunotherapy targeting PD-1 and GITR can rescue CD8(+) T cell dysfunction and maintain memory phenotype. *Sci. Immunol.* 3, eaat7061.

Wei, F., Zhong, S., Ma, Z., Kong, H., Medvec, A., Ahmed, R., Freeman, G.J., Krogsgaard, M., and Riley, J.L. (2013). Strength of PD-1 signaling differentially affects T-cell effector functions. *Proc. Natl. Acad. Sci. U. S. A.* 110, E2480–E2489.

Wei, S.C., Duffy, C.R., and Allison, J.P. (2018). Fundamental mechanisms of immune checkpoint blockade therapy. *Cancer Discov.* 8, 1069–1086.

Wei, S.C., Levine, J.H., Cogdill, A.P., Zhao, Y., Anang, N.A.S., Andrews, M.C., Sharma, P., Wang, J., Wargo, J.A., Pe'er, D., et al. (2017). Distinct cellular

- mechanisms underlie anti-CTLA-4 and anti-PD-1 checkpoint blockade. *Cell* 170, 1120–1133.e17.
- Westergaard, M.C.W., Andersen, R., Chong, C., Kjeldsen, J.W., Pedersen, M., Friese, C., Hasselager, T., Lajer, H., Coukos, G., Bassani-Sternberg, M., et al. (2019). Tumour-reactive T cell subsets in the microenvironment of ovarian cancer. *Br. J. Cancer* 120, 424–434.
- Whittington, P.J., Radkevich-Brown, O., Jacob, J.B., Jones, R.F., Weise, A.M., and Wei, W.Z. (2009). Her-2 DNA versus cell vaccine: immunogenicity and anti-tumor activity. *Cancer Immunol. Immunother.* 58, 759–767.
- Wickham, H. (2016). *ggplot2: Elegant Graphics for Data Analysis* (Springer-Verlag). <https://ggplot2.tidyverse.org>.
- Wolf, M., Kuball, J., Ho, W.Y., Nguyen, H., Manley, T.J., Bleakley, M., and Greenberg, P.D. (2007). Activation-induced expression of CD137 permits detection, isolation, and expansion of the full repertoire of CD8<sup>+</sup> T cells responding to antigen without requiring knowledge of epitope specificities. *Blood* 110, 201–210.
- Wu, L., Seung, E., Xu, L., Rao, E., Lord, D.M., Wei, R.R., Cortez-Retamozo, V., Ospina, B., Posternak, V., Uliniski, G., et al. (2020a). Trispecific antibodies enhance the therapeutic efficacy of tumor-directed T cells through T cell receptor co-stimulation. *Nat. Cancer* 1, 86–98.
- Wu, T.D., Madireddi, S., de Almeida, P.E., Banchereau, R., Chen, Y.-J.J., Chitre, A.S., Chiang, E.Y., Iftikhar, H., O’Gorman, W.E., Au-Yeung, A., et al. (2020b). Peripheral T cell expansion predicts tumour infiltration and clinical response. *Nature* 579, 274–278.
- Xiong, H., Mittman, S., Rodriguez, R., Pacheco-Sanchez, P., Moskalenko, M., Yang, Y., Elstrott, J., Ritter, A.T., Müller, S., Nickles, D., et al. (2019). Coexpression of inhibitory receptors enriches for activated and functional CD8(+) T cells in murine syngeneic tumor models. *Cancer Immunol. Res.* 7, 963–976.
- Xu, X., Hou, B., Fulzele, A., Masubuchi, T., Zhao, Y., Wu, Z., Hu, Y., Jiang, Y., Ma, Y., Wang, H., et al. (2020). PD-1 and BTLA regulate T cell signaling differentially and only partially through SHP1 and SHP2. *J. Cell Biol.* 219, e201905085.
- Yan, J., Pandey, S.P., Barnes, B.J., Turner, J.R., and Abraham, C. (2020). T cell-intrinsic IRF5 regulates T cell signaling, migration, and differentiation and promotes intestinal inflammation. *Cell Rep.* 31, 107820.
- Yarchoan, M., Hopkins, A., and Jaffee, E.M. (2017). Tumor mutational burden and response rate to PD-1 inhibition. *New Engl. J. Med.* 377, 2500–2501.
- Ye, Q., Song, D.G., Poussin, M., Yamamoto, T., Best, A., Li, C., Coukos, G., and Powell, D.J., Jr. (2014). CD137 accurately identifies and enriches for naturally occurring tumor-reactive T cells in tumor. *Clin. Cancer Res. : official J. Am. Assoc. Cancer Res.* 20, 44–55.
- Yoshihara, K., Tajima, A., Yahata, T., Kodama, S., Fujiwara, H., Suzuki, M., Onishi, Y., Hatae, M., Sueyoshi, K., Fujiwara, H., et al. (2010). Gene expression profile for predicting survival in advanced-stage serous ovarian cancer across two independent datasets. *PLoS One* 5, e9615.
- Yoshihara, K., Tsunoda, T., Shigemizu, D., Fujiwara, H., Hatae, M., Fujiwara, H., Masuzaki, H., Katabuchi, H., Kawakami, Y., Okamoto, A., et al. (2012). High-risk ovarian cancer based on 126-gene expression signature is uniquely characterized by downregulation of antigen presentation pathway. *Clin. Cancer Res.* 18, 1374–1385.
- Yost, K.E., Satpathy, A.T., Wells, D.K., Qi, Y., Wang, C., Kageyama, R., McNamara, K.L., Granja, J.M., Sarin, K.Y., Brown, R.A., et al. (2019). Clonal replacement of tumor-specific T cells following PD-1 blockade. *Nat. Med.* 25, 1251–1259.
- Yu, Y., Pilgrim, P., Zhou, W., Gagliano, N., Frezza, E.E., Jenkins, M., Weidanz, J.A., Lustgarten, J., Cannon, M., Bumm, K., et al. (2008). rAAV/Her-2/neu loading of dendritic cells for a potent cellular-mediated MHC class I restricted immune response against ovarian cancer. *Viral Immunol.* 21, 435–442.
- Zamarin, D., Burger, R.A., Sill, M.W., Powell, D.J., Jr., Lankes, H.A., Feldman, M.D., Zivanovic, O., Gunderson, C., Ko, E., Mathews, C., et al. (2020). Randomized phase II trial of nivolumab versus nivolumab and ipilimumab for recurrent or persistent ovarian cancer: an NRG oncology study. *J. Clin. Oncol.* 38, 1814–1823.
- Zhang, L., Conejo-Garcia, J.R., Katsaros, D., Gimotty, P.A., Massobrio, M., Regnani, G., Makrigiannakis, A., Gray, H., Schlienger, K., Liebman, M.N., et al. (2003). Intratumoral T cells, recurrence, and survival in epithelial ovarian cancer. *New Engl. J. Med.* 348, 203–213.
- Zheng, C., Zheng, L., Yoo, J.K., Guo, H., Zhang, Y., Guo, X., Kang, B., Hu, R., Huang, J.Y., Zhang, Q., et al. (2017). Landscape of infiltrating T cells in liver cancer revealed by single-cell sequencing. *Cell* 169, 1342–1356.e16.

STAR★METHODS

KEY RESOURCES TABLE

REAGENT or RESOURCE	SOURCE	IDENTIFIER
<b>Antibodies</b>		
Rabbit monoclonal anti-CD11c, clone EP1347Y (mIF)	Abcam	Cat# ab52632, RRID:AB_2129793
Rabbit monoclonal anti-CD8, clone SP16 (mIF)	ThermoFisher Scientific	Cat# 12603747
Rabbit monoclonal anti-PD-L1, clone E1L3N (mIF)	Cell Signaling Technology	Cat# 13684, RRID:AB_2687655
Mouse monoclonal anti-PD-1, clone MRQ-22 (mIF)	BioSB	Cat# BSB 6216
Mouse monoclonal anti-GzmB, clone GrB-7 (mIF)	Monosan	Cat# 127029F
Mouse monoclonal anti-Cytokeratin, clone AE1/AE3 (mIF)	Dako (now part of Agilent)	Cat# M3515, RRID:AB_2132885
Mouse polyclonal anti-CD68, clone PG-M1 (mIF)	Dako (now part of Agilent)	Cat# M0876, RRID:AB_2074844
Rabbit polyclonal anti-( $\alpha$ )NFATC2 (mIF)	Sigma	Cat# HPA008789, RRID:AB_1079474
HRP-labeled polyclonal goat anti-rabbit (mIF)	Dako	Cat# P0448, RRID:AB_2617138
HRP-labeled polyclonal goat anti-mouse (mIF)	Dako	Cat# P0447, RRID:AB_2617137
Rabbit polyclonal anti-CD3 (mIF)	Dako	Cat# A0452, RRID:AB_2335677
Mouse monoclonal anti-CD11c, clone 5D11 (mIF)	Cell Marque	Cat# 111M-15
Mouse monoclonal anti-CD8a, Clone AMC908 (tCyclF)	eBioscience	CAT#50-0008-80, RRID:AB_2574148
Rabbit monoclonal anti-Cytokeratin 7, clone EPR17078 (tCyclF)	Abcam	Cat# AB209601, RRID:AB_2728790
CD11c (tCyclF)	Cell Singaling	77882BC
Rabbit monoclonal anti-CD11b, clone EPR1344 (tCyclF)	Abcam	Cat# ab204271, RRID:AB_2728739
Rabbit recombinant anti-CD163, Clone EPR14643-36 (tCyclF)	Abcam	Cat# ab218293, RRID:AB_2889155
Rabbit monoclonal anti-pSTAT1, Clone 58D6 (tCyclF)	Cell Signalling	Cat# 8183, RRID:AB_10860600
Rabbit monoclonal anti-Ki-67, clone D3B5 (tCyclF)	Cell Signalling	Cat# 11882, RRID:AB_2687824
Mouse monoclonal anti-PD-1, Clone EH33 (tCyclF)	Cell Signalling	Cat# 43248, RRID:AB_2728836
Rabbit monoclonal anti-PD-L1, Clone E1L3N (tCyclF)	Cell Signalling	Cat# 13684, RRID:AB_2687655
Mouse monoclonal anti-CD45RO, Clone UCHL1 (tCyclF)	BioLegend	Cat# 304212, RRID:AB_528823
Mouse monoclonal anti-CD57, Clone HNK-1 (tCyclF)	BioLegend	Cat# 359612, RRID:AB_2562759
Mouse monoclonal anti-Cyclin A, Clone B-8 (tCyclF)	Santa Cruz	Cat# sc-271682, RRID:AB_10709300
Mouse monoclonal anti-CD3, Clone UCHT1 (FACS, hs)	BD Biosciences	Cat# 555332, RRID:AB_395739
Mouse monoclonal anti-CD4, Clone RPA-T4 (FACS, hs)	BD Biosciences	Cat# 560650, RRID:AB_1727476
Mouse monoclonal anti-CD8, Clone SK1 (FACS, hs)	BD Biosciences	Cat# 345775, RRID:AB_2868803
Mouse monoclonal anti-CD8, Clone SK1 (FACS, hs)	BD Biosciences	Cat# 345773, RRID:AB_2868801
Mouse monoclonal anti-CD27, Clone M-T271 (FACS, hs)	BD Biosciences	Cat# 555440, RRID:AB_395833
Mouse monoclonal anti-CD28, Clone CD28.2 (FACS, hs)	BD Biosciences	Cat# 556622, RRID:AB_396494
Mouse monoclonal anti-CD38, Clone HIT2 (FACS, hs)	BD Biosciences	Cat# 560981, RRID:AB_10563932
Mouse monoclonal anti-CD45RA, Clone HI100 (FACS, hs)	BD Biosciences	Cat# 550855, RRID:AB_398468
Mouse monoclonal anti-CD127, Clone HIL-7R-M21 (FACS, hs)	BD Biosciences	Cat# 560822, RRID:AB_2033938
Rat monoclonal anti-CCR7, Clone 3D12 (FACS, hs)	BD Biosciences	Cat# 557648, RRID:AB_396765
anti-HLA-DR, Clone G46-6 (FACS, hs)	BD Biosciences	Cat# 556643, RRID:AB_396509
Mouse monoclonal anti-CTLA-4, Clone BNI3 (FACS, hs)	BD Biosciences	Cat# 557301, RRID:AB_396628
Mouse monoclonal anti-PD-1, Clone EH12.2H7 (FACS, hs)	BioLegend	Cat# 329924, RRID:AB_2563212
Mouse monoclonal anti-CD137, Clone 4B4-1 (FACS, hs)	BioLegend	Cat# 309820, RRID:AB_2563830
Mouse monoclonal anti-CD45, Clone HI30 (FACS, hs)	BioLegend	Cat# 304028, RRID:AB_893338
Mouse monoclonal anti-CD28, Clone CD28.2 (FACS, hs)	BioLegend	Cat# 302920, RRID:AB_528786
Mouse monoclonal anti-CD14, Clone M5E2 (FACS, hs)	BioLegend	Cat# 367126, RRID:AB_2716231
Mouse monoclonal anti-CD11b, Clone ICRF44 (FACS, hs)	BioLegend	Cat# 301336, RRID:AB_2563793

(Continued on next page)

**Continued**

REAGENT or RESOURCE	SOURCE	IDENTIFIER
Mouse monoclonal anti-PD-L1, Clone 29E.2A3 (FACS, hs)	BioLegend	Cat# 329738, RRID:AB_2617010
Mouse monoclonal anti-HLA-I, Clone W6/32 (FACS, hs)	BioLegend	Cat# 311438, RRID:AB_2566306
Mouse monoclonal anti-CD80, Clone 2D10 (FACS, hs)	BioLegend	Cat# 305206, RRID:AB_314502
Mouse monoclonal anti-CD86, Clone IT2.2 (FACS, hs)	BioLegend	Cat# 305442, RRID:AB_2616794
Mouse monoclonal anti-PD-L2, Clone 24F.10C12 (FACS, hs)	BioLegend	Cat# 345512, RRID:AB_2687280
Mouse monoclonal anti-Ki-67, Clone B56 (FACS, hs)	BD Biosciences	Cat# 561281, RRID:AB_10613816
Mouse monoclonal anti-BCL-2, Clone Bcl-2/100 (FACS, hs)	BD Biosciences	Cat# 340576, RRID:AB_400061
Mouse monoclonal anti-T-bet, Clone O4-46 (FACS, hs)	BD Biosciences	Cat# 561268, RRID:AB_10564071
Mouse monoclonal anti-perforin, Clone $\delta$ G9 (FACS, hs)	BD Biosciences	Cat# 556577, RRID:AB_396470
Mouse monoclonal anti-granzyme B, Clone GB12 (FACS, hs)	ThermoFisher Scientific	Cat# MHGB04, RRID:AB_10372671
Mouse monoclonal anti-IL-2, Clone 5344.111 (FACS, hs)	BD biosciences	Cat# 340450, RRID:AB_400426
Mouse monoclonal anti-IFN $\gamma$ , Clone 25723.11 (FACS, hs)	BD biosciences	Cat# 341117, RRID:AB_2264629
Mouse monoclonal anti-IFN $\gamma$ , Clone 25723.11 (FACS, hs)	BD biosciences	Cat# 340452, RRID:AB_400428
Mouse monoclonal anti-CD11b, Clone ICRF44 (FACS, hs)	BioLegend	Cat# 301335, RRID:AB_2562761
Mouse monoclonal anti-CD11c, Clone Bu15 (FACS, hs)	BioLegend	Cat# 337219, RRID:AB_2561502
Mouse monoclonal anti-CD14, Clone 63D3 (FACS, hs)	BioLegend	Cat# 367125, RRID:AB_2716230
Mouse monoclonal anti-CD80, Clone 2D10 (FACS, hs)	BioLegend	Cat# 305205, RRID:AB_314501
Mouse monoclonal anti-CD83, Clone HB15e (FACS, hs)	BioLegend	Cat# 305323, RRID:AB_10899571
Mouse monoclonal anti-CD86, Clone BU63 (FACS, hs)	BioLegend	Cat# 374207, RRID:AB_2721448
Mouse monoclonal anti-HLA-DR, Clone L243 (FACS, hs)	BioLegend	Cat# 307658, RRID:AB_2572101
Rat monoclonal anti-PD-L1, Clone 10F.9G2 (FACS, hs)	BioLegend	Cat# 124333, RRID:AB_2629831
Mouse monoclonal anti-PD-L2, Clone MIH18 (FACS, hs)	BioLegend	Cat# 345511, RRID:AB_2687279
Mouse monoclonal anti-human PD-1, EH12-2H7, mouse IgG1 (blocking)	BioLegend	Cat# 329926, RRID:AB_11147365
anti-PD-L1 (blocking)	gift from Dr Gordon J Freeman, Dana Farber Cancer Institute	NA
anti-PD-L2 (blocking)	gift from Dr Gordon J Freeman, Dana Farber Cancer Institute	NA
anti-CTLA-4 (blocking)	Ipilimumab, gift from Bristol-Myers-Squibb, Cambridge, MA	NA
IgG2b antibody (blocking)	gift from Dr Gordon J Freeman, Dana Farber Cancer Institute	NA
IgG1 antibody (blocking)	gift from Dr Gordon J Freeman, Dana Farber Cancer Institute	NA
Mouse monoclonal anti-CD11b, Clone D12 (FACS, hs)	BD Biosciences	Cat# 347557, RRID:AB_400323
Mouse monoclonal anti-CD11c, Clone S-HCL-3 (FACS, hs)	BD Biosciences	Cat# 347637, RRID:AB_2129929
Mouse monoclonal anti-CD14, Clone HCD14 (FACS, hs)	BioLegend	Cat# 325605, RRID:AB_830678
Mouse monoclonal anti-CD68, Clone Y1/82A (FACS, hs)	BioLegend	Cat# 333807, RRID:AB_1089057
Mouse monoclonal phosphor-ERK-specific antibodies (20A)	BD Biosciences	Cat# 561991, RRID:AB_10895978
Rat monoclonal anti-PD-1, Clone RMP1-14 ( <i>in vivo</i> )	BioX Cell	Cat# BE0146, RRID:AB_10949053
Mouse monoclonal anti-CTLA-4, Clone 9D9 ( <i>in vivo</i> )	BioX Cell	Cat# BE0164, RRID:AB_10949609
Rat monoclonal CD40L, Clone FGK45 ( <i>in vivo</i> )	BioX Cell	Cat# BE0016-2, RRID:AB_1107647

(Continued on next page)

Continued

REAGENT or RESOURCE	SOURCE	IDENTIFIER
Mouse monoclonal anti-CD28, Clone E18 ( <i>in vivo</i> )	BioLegend	Cat# 122022, RRID:AB_2810371
Mouse monoclonal anti-CD45.2, Clone 104 (FACS, mm)	BD Biosciences	Cat# 612779, RRID:AB_2870108
Rat monoclonal anti-CD83, Clone Michel-19 (FACS, mm)	BD Biosciences	Cat# 563136, RRID:AB_2738024
Rat monoclonal anti-I-A/I-E, Clone 2G9, (FACS, mm)	BD Biosciences	Cat# 562009, RRID:AB_10893593
Rat monoclonal anti-Gr1, Clone RB6-8C5 (FACS, mm)	BD Biosciences	Cat# 562060, RRID:AB_10893227
Rat monoclonal anti-PD-1, Clone 29F.1A12 (FACS, mm)	BioLegend	Cat# 135241, RRID:AB_2715761
Rat monoclonal anti-PD-L1, Clone 10F.9G2 (FACS, mm)	BioLegend	Cat# 124331, RRID:AB_2629659
Armenian hamster monoclonal anti-CD80, Clone 16-10A1 (FACS, mm)	BioLegend	Cat# 104725, RRID:AB_10900989
Rat monoclonal anti-CD86, Clone GL-1 (FACS, mm)	BioLegend	Cat# 105045, RRID:AB_2629769
Rat monoclonal anti-CD4, Clone RM4-5 (FACS, mm)	BioLegend	Cat# 100549, RRID:AB_11219396
Rat monoclonal anti-F4/80, Clone BM8 (FACS, mm)	BioLegend	Cat# 123149, RRID:AB_2564589
Rat monoclonal anti-CD11b, Clone M1/70 (FACS, mm)	BioLegend	Cat# 101237, RRID:AB_11126744
Rat monoclonal anti-Ki-67 PE/Dazzle, Clone 16A8 (FACS, mm)	BioLegend	Cat# 652427, RRID:AB_2632695
Armenian hamster monoclonal anti-CD103, Clone 2E7 (FACS, mm)	BioLegend	Cat# 121405, RRID:AB_535948
Syrian hamster monoclonal anti-CD137, Clone 17B5 (FACS, mm)	BioLegend	Cat# 106109, RRID:AB_2564296
Rat monoclonal anti-PD-L2, Clone 122 (FACS, mm)	ThermoFisher Scientific	Cat# 46-9972-82, RRID:AB_2573928
Rat monoclonal anti-CD8a, Clone 53.6.7 (FACS, mm)	ThermoFisher Scientific	Cat# 47-0081-82, RRID:AB_1272185
Armenian hamster monoclonal anti-CD11c, Clone N418 (FACS, mm)	ThermoFisher Scientific	Cat# 17-0114-82, RRID:AB_469346
Mouse monoclonal anti-CD45, Clone 2D1 (scRNAseq)	BioLegend	Cat# 368503, RRID:AB_2566351
Mouse monoclonal anti-CD3, Clone UCHT1 (scRNAseq)	BioLegend	Cat# 300463, RRID:AB_2566035
Mouse monoclonal anti-CD8, Clone SK1 (scRNAseq)	BioLegend	Cat# 344729, RRID:AB_2564509
anti-human CD45, Clone HI30 89Y (CyTOF)	Fluidigm	Cat # 3089003B, RRID:AB_2661851
anti-human IL-17A, Clone N49653 164Dy (CyTOF)	Fluidigm	Cat # 3164002B, RRID:AB_2864733
anti-human CD4, Clone RPA-T4, conjugated to 143Nd (CyTOF)	BioLegend	Cat # 300541, RRID:AB_2562809
anti-human CD69, Clone FN50 144Nd (CyTOF)	Fluidigm	Cat # 3144018, RRID:AB_2687849
anti-human CD8, Clone RPA-T8 146Nd (CyTOF)	Fluidigm	Cat # 3146001B, RRID:AB_2687641
anti-human (cross) pStat5, Clone 47 147Sm (CyTOF)	Fluidigm	Cat # 3147012A, RRID:AB_2661819
anti-human EOMES, Clone 644730 148Nd (CyTOF)	Novus Biologicals	Cat # MAB6166
anti-human Lag-3, Clone 11C3C65 150Nd (CyTOF)	Fluidigm	Cat # 3150030B
anti-human CD103, Clone BerACT8 151Eu (CyTOF)	Fluidigm	Cat # 3151011B, RRID:AB_2756418
anti-human TNF $\alpha$ , Clone Mab11 152Sm (CyTOF)	Fluidigm	Cat # 3152002B
anti-human Tim-3, Clone F382E2 153Eu (CyTOF)	Fluidigm	Cat # 3153008B, RRID:AB_2687644
anti-human TIGIT, Clone MBSA43 154Sm (CyTOF)	Fluidigm	Cat # 3154016B, RRID:AB_2888926
anti-human PD-1, Clone EH12.2H7 155Gd (CyTOF)	Fluidigm	Cat # 3155009B, RRID:AB_2687854
anti-human IL-6 Clone MQ213A5 156Gd (CyTOF)	Fluidigm	Cat # 3156011B, RRID:AB_2810973
anti-human CD127, Clone A019D5 165Ho (CyTOF)	Fluidigm	Cat # 3165008B, RRID:AB_2868401

(Continued on next page)

**Continued**

REAGENT or RESOURCE	SOURCE	IDENTIFIER
anti-human CD244, Clone C1.7, conjugated to 142Nd (CyTOF)	BioLegend	Cat # 329502, RRID:AB_1279194
anti-human CD28, Clone CD28.2 160Gd (CyTOF)	Fluidigm	Cat # 3160003B, RRID:AB_2868400
anti-human CTLA-4, Clone 14D3 161Dy (CyTOF)	Fluidigm	Cat # 3161004B, RRID:AB_2687649
anti-human Ki67, Clone B56 162Dy (CyTOF)	Fluidigm	Cat # 3162012B, RRID:AB_2888928
anti-human OX40, Clone ACT35, conjugated to 145Nd (CyTOF)	BioLegend	Cat # 350015, RRID:AB_2563718
anti-human CD215, polyclonal, conjugated to 148Nd (CyTOF)	Novus Biologicals	Cat # AF247
anti-human IL-2, Clone MQ117H12 166Er (CyTOF)	Fluidigm	Cat # 3166002B
anti-human CD27, Clone L128 167Er (CyTOF)	Fluidigm	Cat # 3167006B, RRID:AB_2811093
anti-human IFN $\gamma$ , Clone B27 168Er (CyTOF)	Fluidigm	Cat # 3168005B
anti-human CD49d, Clone 9F10 141Pr (CyTOF)	Fluidigm	Cat # 3141004B
anti-human pStat3, Clone pY705, conjugated to 149Sm (CyTOF)	BD Biosciences	Cat # 612357, RRID:AB_399646
anti-human GITR, Clone 621 159Tb (CyTOF)	Fluidigm	Cat # 3159020B, RRID:AB_2858232
anti-human CD25, Clone 2A3 169Tm (CyTOF)	Fluidigm	Cat # 3169003B, RRID:AB_2661806
anti-human CD137, Clone 4B41 158Gd (CyTOF)	Fluidigm	Cat # 3158013B, RRID:AB_2888927
anti-human Ki-67, Clone B56 172Yb (CyTOF)	Fluidigm	Cat # 3172024B, RRID:AB_2858243
anti-human CD160, Clone 688327, conjugated to 176Yb (CyTOF)	R&D Systems	Cat # mab6700, RRID:AB_10891689
anti-human TCF1, Clone 7F11A10, conjugated to 149Sm (CyTOF)	BioLegend	Cat # 655202, RRID:AB_2562103
anti-human LEF1, Clone 15H5A18, conjugated to 163Dy (CyTOF)	BioLegend	Cat # 653102, RRID:AB_2561615
anti-human CD3, Clone UCHT1 170Er (CyTOF)	Fluidigm	Cat # 3170001B, RRID:AB_2811085
anti-human Granzyme B, Clone GB11 171Yb (CyTOF)	Fluidigm	Cat # 3171002B, RRID:AB_2687652
anti-human CD57, Clone HCD57 172Yb (CyTOF)	Fluidigm	Cat # 3172009B, RRID:AB_2888930
anti-human CD137, Clone 4B4-1 173Yb (CyTOF)	Fluidigm	Cat # 3173015B
anti-human HLA-DR, Clone L243 174Yb (CyTOF)	Fluidigm	Cat # 3174001B, RRID:AB_2665397
anti-human Perforin, Clone BD48 175Yb (CyTOF)	Fluidigm	Cat # 3175004B
anti-human CD127, Clone A019D5 176Yb (CyTOF)	Fluidigm	Cat # 3176004B, RRID:AB_2687863

**Biological samples**

High-grade serous ovarian cancer (HGSOC) specimens, ascites, PBMCs	Ovarian Cancer Research Center Tumor Bank Facility at the University of Pennsylvania	<a href="https://www.med.upenn.edu/OCRCBioTrust/">https://www.med.upenn.edu/OCRCBioTrust/</a>
HGSOC specimens	Herlev Hospital, Copenhagen	<a href="#">Westergaard et al. (2019)</a>
Ovarian cancer samples	Topacio clinical study	<a href="#">Färkkilä et al. (2020)</a>

(Continued on next page)

REAGENT or RESOURCE	SOURCE	IDENTIFIER
<b>Continued</b>		
Chemicals, peptides, and recombinant proteins		
Zombie Aqua Fixable Viability Dye	BioLegend	Cat# 423101
Zombie UV Fixable Viability Dye	BioLegend	Cat# 423107
Human CD40-Ligand	Miltenyi Biotec	Cat# 130-096-714
RPMLI-1640	Gibco	Cat# 61870-010
Cell Conditioning 1 (CC1) buffer	Ventana	Cat# 950-124
Protein block buffer	Dako	Cat# X090930-2
TSA Fluorescein	PerkinElmer	Cat# NEL741B001KT
TSA Cyanine 5	PerkinElmer	Cat# NEL745B001KT
TSA Cyanine 3.5	PerkinElmer	Cat# NEL763B001KT
TSA Cyanine 5.5	PerkinElmer	Cat# NEL766B001KT
TSA Cyanine 3	PerkinElmer	Cat# NEL744B001KT
DAPI	Biolegend	Cat#422801
Fluorescence mounting medium	Dako	Cat# S3023
GolgiStop	BD Biosciences	Cat# 554715, RRID:AB_2869009
FACS permeabilization solution	BD Biosciences	Cat# 554715, RRID:AB_2869009
Brefeldin A (Protein Transport Inhibitor Cocktail)	eBiosciences	Cat# 00-4980-93
Collagenase I	Gibco	Cat# 171-00-017
Collagenase IV	Gibco	Cat# 171-04-019
DNase	Roche	Cat# 50-100-3290
DMSO	Sigma-Aldrich	Cat# D8418
Human serum	Valley Biomedical	Cat# HS1017
IL-7	PeproTech	Cat# 200-07
IL-15	PeproTech	Cat# 200-15
127 IdU (5-Iodo-2' -deoxyuridine)	Fluidigm	Cat # 201127
Iridium 191/193	Fluidigm	Cat # 201192A
mm-DOTA (Macrocyclics) 139	Wherry Lab	Custom made
Cisplatin 195	Fluidigm	Cat # 201195
Maxpar Fixation/permeabilization buffer	Fluidigm	Cat # 201067
Maxpar cell staining buffer	Fluidigm	Cat # 201068
anti-PE magnetic beads	Miltenyi	Cat# 130-048-801
Carboxy-fluorescein diacetate succinimidyl ester (CFSE)	ThermoFischer Scientific	Cat# C34554
p2TA and p2TA scramble, custom made	Protein and Peptide Chemistry Facility, UNIL	NA
Chromium-51 <sup>51</sup> Cr	PerkinElmer	NEZ030S001MC
Granzyme A CBA Flex Set D9	BD Biosciences	Cat# 560299, RRID:AB_2869330
Granzyme B CBA Flex Set D7	BD Biosciences	Cat# 560304, RRID:AB_2869331
IL-2 ES CBA Flex Set A4	BD Biosciences	Cat# 561517, RRID:AB_2869379
IFN-Gamma ES CBA Flex Set B8	BD Biosciences	Cat# 561515, RRID:AB_2869377
TNF ES CBA Flex Set C4	BD Biosciences	Cat# 561516, RRID:AB_2869378
Permeabilization buffer III	BD Biosciences	Cat# 558050
PGE <sub>2</sub>	PeproTech	Cat# 3632464
IFN <sub>γ</sub>	PeproTech	Cat# 300-02
0.09% NaCl solution	Bichsel AG	FE1001340
Fish Gelatin	Sigma Aldrich	Cat# G7765
RNasin	Promega	Cat# N2611
Fc Block	Miltenyi Biotec	Cat# 130-059-901
Calcein AM	ThermoFisher Scientific	Cat# C3099

(Continued on next page)

**Continued**

REAGENT or RESOURCE	SOURCE	IDENTIFIER
BSA	Sigma Aldrich	Cat# A2153
MHC class I, HER2/neu p369 (KIFGSLAFL)	TCMetrix	NA
MHC class I, HER2/neu p689 (RLLQETELV)	TCMetrix	NA
MHC class I, survivin (LMLGEFLKL)	TCMetrix	NA
MHC class I, NY-ESO-1 (SLLMWITQC)	TCMetrix	NA
MHC class I, mesothelin (VLPLTVAEV)	TCMetrix	NA
MHC class I, hTERT (ILAKFLHWL)	TCMetrix	NA
MHC class I, p53 (LLGRNSFEV)	TCMetrix	NA
MHC class I, SP-17 (ILDSSEEDK)	TCMetrix	NA
MHC class I, WT-1 (RMFPNAPYL)	TCMetrix	NA
MHC class II, folate receptor (FR)-a 147 (RTSYTCKSNWHKGNWT)	TCMetrix	NA
MHC class II, FR-a 56 (QCRPWRKNACCSTNT)	TCMetrix	NA
MHC class II, hTERT E611 (EARPALLTSRLRFIPK)	TCMetrix	NA
MHC class II, NY-ESO-1 (SLLMWITQCFLPVF)	TCMetrix	NA
PepTivator WT1	Miltenyi Biotec	Cat# 130-095-916
PepTivator TERT	Miltenyi Biotec	Cat# 130-097-277
PepTivator NY-ESO-1	Miltenyi Biotec	Cat# 130-095-380

**Critical commercial assays**

Maxpar X8 Antibody Labeling Kit, 143Nd—4 Rxn	Fluidigm	Cat# 201143A
Maxpar X8 Antibody Labeling Kit, 142Nd—4 Rxn	Fluidigm	Cat #201142A
Maxpar X8 Antibody Labeling Kit, 145Nd—4 Rxn	Fluidigm	Cat #201145A
Maxpar X8 Antibody Labeling Kit, 148Nd—4 Rxn	Fluidigm	Cat # 201148A
Maxpar X8 Antibody Labeling Kit, 149Sm—4 Rxn	Fluidigm	Cat # 201149A
Maxpar X8 Antibody Labeling Kit, 176Yb—4 Rxn	Fluidigm	Cat #201176A
Maxpar® X8 Antibody Labeling Kit, 163Dy—4 Rxn	Fluidigm	Cat #201163A
Micro RNA Isolation kit	Stratagene, La Jolla, CA	<a href="#">Fend et al. (1999)</a>
RNeasy micro kit	Qiagen	Cat# 74004
DNeasy blood and tissue kit	Qiagen	Cat# 69504
10x Chromium Single Cell 5' Gel beads and Library kit	10X Genomics	Cat# 1000006
Dynabeads MyOne SILANE	10X Genomics	Cat# 2000048
5' Library construction kit	10X Genomics	Cat# 1000002
Chromium Single cell VDJ enrichment kit (human T cell)	10X Genomics	Cat# 1000005
Qubit dsDNA HS assay kit	ThermoFisher	Cat# Q32851
Fragment analyzer kit HS-NGS (1-6000pb)	Agilent	DNF-473-0500

**Deposited data**

Raw and analyzed data	This paper	GEO: GSE178245
Transcription and microRNA profiling by array of human high grade, late stage serous ovarian cancer	<a href="#">Bentink et al. (2012)</a>	E-MTAB-386
Survival Related Profile, Pathways and Transcription Factors in Ovarian Cancer	<a href="#">Crijns et al. (2009)</a>	GSE13876
Prediction of progression-free survival in patients with advanced-stage serous ovarian cancer	<a href="#">Yoshihara et al. (2010)</a>	GSE17260
Whole-genome oligonucleotide expression analysis of papillary serous ovarian adenocarcinomas	<a href="#">Mok et al. (2009)</a>	GSE18520
Control of oxidative stress by miRNA and impact on ovarian tumorigenesis	<a href="#">Gentric et al. (2019)</a>	GSE26193
Genomic Multivariate Predictors of Response to Adjuvant Chemotherapy in Ovarian Carcinoma: Predicting Platinum Resistance	<a href="#">Ferriss et al. (2012)</a>	GSE30161

(Continued on next page)

**Continued**

REAGENT or RESOURCE	SOURCE	IDENTIFIER
Immune-activation as a therapeutic direction for patients with high-risk ovarian cancer based on gene expression signature	Yoshihara et al. (2012)	GSE32062
Validating the Impact of a Molecular Subtype in Epithelial Ovarian Cancer (EOC) on Progression Free and Overall Survival	Pils et al. (2012)	GSE49997
Expression profile of 285 ovarian tumour samples	Tothill et al. (2008)	GSE9891
Integrated genomic analyses of ovarian carcinoma	TCGA-RNASeqV2	<a href="https://rdrr.io/bioc/MetaGxOvarian/man/TCGA.RNASeqV2.html">https://rdrr.io/bioc/MetaGxOvarian/man/TCGA.RNASeqV2.html</a>
TCGA RNA sequencing data	GDAC firehose platform (Broad Institute of MIT and Harvard, 2016)	<a href="https://gdac.broadinstitute.org">https://gdac.broadinstitute.org</a>
pan-cancer TCGA	TCGA pan-cancer atlas repository	<a href="https://gdc.cancer.gov/about-data/publications/pancanatlas">https://gdc.cancer.gov/about-data/publications/pancanatlas</a>
Programmed death 1 receptor blockade and immune-related gene expression profiling in non-small cell lung carcinoma, head and neck squamous cell carcinoma and melanoma	Prat et al. (2017)	GSE93157
mRNA expressions in pre-treatment melanomas undergoing anti-PD-1 checkpoint inhibition therapy	Hugo et al. (2016)	GSE78220
Comprehensive immunoproteogenomic analyses of malignant pleural mesothelioma	Lee et al. (2018)	GSE99070
Transcriptional mechanisms of resistance to anti-PD-1 therapy	Ascierto et al. (2017)	GSE79691
<b>Experimental models: Cell lines</b>		
OvCar5 cells expressing HLA-A2-NY-ESO-1	Dr. M. Irving, Ludwig Institute, Lausanne branch	NA
NY-ESO-1 CD8 <sup>+</sup> TIL clone	Dr. N. Rufer, Ludwig Institute, Lausanne branch	NA
<i>Tp53</i> <sup>-/-</sup> <i>Brca1</i> <sup>-/-</sup> ID8 ovarian cancer cells expressing luciferase	Dr. Ian McNeish, Imperial College London	Walton et al. (2017) and Bruand et al. (2021)
<b>Experimental models: Organisms/strains</b>		
Conventional C57BL/6 mice	Envigo	057
Immunodeficient NSG mice	Stem Cell and Xenograft Core of the Abramson Cancer Center (University of Pennsylvania)	NA
<b>Software and algorithms</b>		
Nuance Image Analysis software	PerkinElmer	<a href="https://www-punchout.perkinelmer.com/Content/LST_Software_Downloads/tissueimaging/NuanceUserManual_3_0_2_rev0.pdf">https://www-punchout.perkinelmer.com/Content/LST_Software_Downloads/tissueimaging/NuanceUserManual_3_0_2_rev0.pdf</a>
inForm 2.1.0 image analysis software	PerkinElmer	<a href="https://www.perkinelmer.com/Content/LST_Software_Downloads/inFormUserManual_2_3_0_rev1.pdf">https://www.perkinelmer.com/Content/LST_Software_Downloads/inFormUserManual_2_3_0_rev1.pdf</a>
xAverageCountsBatch.R	PerkinElmer	<a href="https://www.perkinelmer.com">https://www.perkinelmer.com</a>
BaSiC	Peng et al. (2017)	<a href="https://sites.imagej.net/BaSiC/">https://sites.imagej.net/BaSiC/</a>
ASHLAR	GitHub (2018)	<a href="https://github.com/labsyspharm/ashlar/blob/master/README.md">https://github.com/labsyspharm/ashlar/blob/master/README.md</a>
UNet neural network	Ronneberger et al. (2015)	<a href="https://arxiv.org/abs/1505.04597">https://arxiv.org/abs/1505.04597</a>

(Continued on next page)

**Continued**

REAGENT or RESOURCE	SOURCE	IDENTIFIER
HistoCAT v1.73	Schapiro et al. (2017)	<a href="https://github.com/BodenmillerGroup/histoCAT/releases/tag/histoCAT_1.73">https://github.com/BodenmillerGroup/histoCAT/releases/tag/histoCAT_1.73</a>
SoftWorx, version 2018b	MATLAB	<a href="https://www.mathworks.com">https://www.mathworks.com</a>
FlowJo	BD Biosciences	<a href="https://www.flowjo.com">https://www.flowjo.com</a>
The matlab tool cyt (R2015)	MATLAB	<a href="https://www.mathworks.com">https://www.mathworks.com</a>
Cellranger, version 3.0.2 and version 3.1.0	10x Genomics	<a href="https://support.10xgenomics.com/single-cell-gene-expression/software/overview/welcome">https://support.10xgenomics.com/single-cell-gene-expression/software/overview/welcome</a>
BaseCalling in Illumina RTA 1.18.66.3	Illumina	<a href="https://www.illumina.com">https://www.illumina.com</a>
Illumina pipeline 2.19.1	Illumina	<a href="https://www.illumina.com">https://www.illumina.com</a>
FastQC	Andrews (2010)	<a href="https://www.bioinformatics.babraham.ac.uk/projects/fastqc/">https://www.bioinformatics.babraham.ac.uk/projects/fastqc/</a>
Seurat, version 3.1.0	Butler et al. (2018) and Stuart et al. (2019)	<a href="https://satijalab.org/seurat/">https://satijalab.org/seurat/</a>
R language for statistical computing	R Core Team (2020)	<a href="https://www.r-project.org">https://www.r-project.org</a>
ggplot2	Wickham (2016)	<a href="https://cran.r-project.org/web/packages/ggplot2/index.html">https://cran.r-project.org/web/packages/ggplot2/index.html</a>
pheatmap	Kolde (2019)	<a href="https://cran.r-project.org/web/packages/pheatmap/index.html">https://cran.r-project.org/web/packages/pheatmap/index.html</a>
SCENIC	Aibar et al. (2017)	<a href="https://scenic.aertslab.org">https://scenic.aertslab.org</a>
Genie3	Huynh-Thu et al. (2010)	<a href="https://bioconductor.org/packages/release/bioc/html/GENIE3.html">https://bioconductor.org/packages/release/bioc/html/GENIE3.html</a>
RcisTarget	Aibar et al. (2017)	<a href="https://github.com/aertslab/RcisTarget">https://github.com/aertslab/RcisTarget</a>
AUCell	Aibar et al. (2017)	<a href="https://github.com/aertslab/AUCell">https://github.com/aertslab/AUCell</a>
curatedOvarianData	Ganzfried et al. (2013)	<a href="https://bioconductor.org/packages/release/data/experiment/html/curatedOvarianData.html">https://bioconductor.org/packages/release/data/experiment/html/curatedOvarianData.html</a>
limma	Ritchie et al. (2015)	<a href="https://bioconductor.org/packages/release/bioc/html/limma.html">https://bioconductor.org/packages/release/bioc/html/limma.html</a>
MegaClust	Nowicka et al. (2017)	<a href="https://megaclust.vital-it.ch">https://megaclust.vital-it.ch</a>
flowCore	Bioconductor R package	<a href="https://bioconductor.org/packages/release/bioc/html/flowCore.html">https://bioconductor.org/packages/release/bioc/html/flowCore.html</a>
ropls	Thévenot et al. (2015)	<a href="https://www.bioconductor.org/packages/release/bioc/html/ropls.html">https://www.bioconductor.org/packages/release/bioc/html/ropls.html</a>

**Equipment**

Discovery ULTRA Staining Module with the Tyramide signal amplification	Ventana, Roche	<a href="https://diagnostics.roche.com/global/en/products/instruments/discovery">https://diagnostics.roche.com/global/en/products/instruments/discovery</a>
Vectra 3.0 automated quantitative pathology imaging system	PerkinElmer	<a href="https://www.akoyabio.com/phenoptics/mantra-vectra-instruments/vectra-3-0/">https://www.akoyabio.com/phenoptics/mantra-vectra-instruments/vectra-3-0/</a>
μCUT Laser-MicroBeam System	SL Microtest, Jena, Germany	Gjerdum et al. (2001)
RareCyte CyteFinder scanner	Lin et al. (2018)	<a href="https://rarecyte.com/cytefinder/">https://rarecyte.com/cytefinder/</a>
Deltavision Elite	GE Life Sciences	<a href="https://www3.unifr.ch/bioimage/microscopes/live-imaging/ge-deltavision-elite-med/">https://www3.unifr.ch/bioimage/microscopes/live-imaging/ge-deltavision-elite-med/</a>
LSRII-SORP	BD Biosciences	<a href="https://www.expmedndm.ox.ac.uk/flow-cytometry-facility/lsr-ii-sorp">https://www.expmedndm.ox.ac.uk/flow-cytometry-facility/lsr-ii-sorp</a>
CytoFlex LX	Beckman Coulter	<a href="https://www.beckman.ch/flow-cytometry/instruments/cytoflex-lx">https://www.beckman.ch/flow-cytometry/instruments/cytoflex-lx</a>
FACSAria III	BD Biosciences	<a href="https://www.bdbiosciences.com/en-us/instruments/research-instruments/research-cell-sorters/facsaria-iii">https://www.bdbiosciences.com/en-us/instruments/research-instruments/research-cell-sorters/facsaria-iii</a>

(Continued on next page)

<i>Continued</i>		
REAGENT or RESOURCE	SOURCE	IDENTIFIER
Gallios	Beckman Coulter	<a href="https://www.beckman.ch/flow-cytometry/instruments/gallios">https://www.beckman.ch/flow-cytometry/instruments/gallios</a>
CyTOF Helios	Fluidigm	<a href="https://www.fluidigm.com/products/helios">https://www.fluidigm.com/products/helios</a>
Illumina Genome Analyzer	Adaptive Biotechnologies, Seattle, USA	<a href="https://www.illumina.com/documents/products/datasheets/datasheet_genome_analyzer_software.pdf">https://www.illumina.com/documents/products/datasheets/datasheet_genome_analyzer_software.pdf</a>
TopCount NXT Scintillation Counter	PerkinElmer	<a href="https://www.perkinelmer.com/CMSResources/Images/44-73884SPC_TopCountNXTMicropt Scint.pdf">https://www.perkinelmer.com/CMSResources/Images/44-73884SPC_TopCountNXTMicropt Scint.pdf</a>
luma-plate	PerkinElmer	Cat# 6006633
Adaptive Biotechnology	Adaptive Biotechnologies	<a href="https://www.immunoseq.com/assays/">https://www.immunoseq.com/assays/</a>
IVIS Lumina II	Perkin Elmer	NA
MoFlo Astrios	Beckman Coulter	<a href="https://www.beckman.ch/flow-cytometry/instruments/moflo-astrios-eq">https://www.beckman.ch/flow-cytometry/instruments/moflo-astrios-eq</a>
5200 Fragment Analyzer	Agilent	<a href="https://www.agilent.com/en/product/automated-electrophoresis/fragment-analyzer-systems/fragment-analyzer-systems/5200-fragment-analyzer-system-365720">https://www.agilent.com/en/product/automated-electrophoresis/fragment-analyzer-systems/fragment-analyzer-systems/5200-fragment-analyzer-system-365720</a>
Illumina HiSeq 4000	Illumina	<a href="https://www.illumina.com/systems/sequencing-platforms/hiseq-3000-4000.html">https://www.illumina.com/systems/sequencing-platforms/hiseq-3000-4000.html</a>

## RESOURCE AVAILABILITY

### Lead contact

Further information and requests for resources and reagents should be directed to and will be fulfilled by the lead contact, George Coukos ([George.Coukos@chuv.ch](mailto:George.Coukos@chuv.ch)).

### Materials availability

This study did not generate new unique reagents.

### Data and code availability

The accession number for the raw and processed single cell sequencing data reported in this paper is GEO: GSE178245.

Ovarian gene expression profiles with patient survival data were obtained from: E-MTAB-386, GSE13876, GSE17260, GSE18520, GSE26193, GSE30161, GSE32062, GSE49997, GSE9891, TCGA-RNASeqV2. Public cancer cohorts with both gene expression profiling and clinical response to  $\alpha$ PD-1 treatment were obtained from: GSE93157, GSE78220, GSE99070, GSE79691 (Roh et al., 2017; Chen et al., 2016).

## EXPERIMENTAL MODEL AND SUBJECT DETAILS

### Tumor and peripheral blood mononuclear cell samples

**UPENN cohort:** De-identified tumor specimens (n = 74), ascites, and peripheral blood mononuclear cells (PBMCs) were obtained from the Ovarian Cancer Research Center Tumor Bank Facility at the University of Pennsylvania. Samples were collected from unselected consecutive patients (“all comers”) undergoing surgery for stage III or IV high-grade serous ovarian cancer (HGSOC), as well as from the fallopian tube or primary peritoneal origin, at the Hospital of the University of Pennsylvania, Philadelphia, under an approved protocol from the Institutional Review Board (UPCC 17909, IRB 702679) under the care of Dr DJ Powell Jr. It should be noted that high grade serous cancer from ovarian, fallopian tube or primary peritoneal origin are regarded as the same pathologic entity as they have the same tissue origin, histology, and molecular features and they are presently understood to originate all from the fallopian tube epithelium, while the anatomic attribution depends on the surgical identification of an ovarian or fallopian tube mass. These samples were digested freshly (see below) and tumor digests were used for experiments or viably cryopreserved. Paraffin blocks from the same tumors were also procured and stored for tissue analyses.

**Herlev cohort:** A second cohort of processed HGSOc specimens ( $n = 21$ ) was obtained from patients at Herlev Hospital, Copenhagen, under a protocol approved by the National Committee on Health Research Ethics (reference number H-2-2014-055) under the care of Dr IM Svane (Westergaard et al., 2019).

**Topacio clinical study cohort:** We collaborated with Drs Anniina Färkkilä (University of Helsinki) and Peter Sorger (Harvard University) to investigate 15 different ovarian cancer samples collected in the context of the Topacio clinical study (Färkkilä et al., 2020).

**Melanoma cohort:** We collaborated with Dr Olivier Michielin (CHUV) to investigate 26 metastatic melanoma samples from patients with progression ( $n = 14$ ) versus response status ( $n = 12$ ) after ICB (anti-CTLA-4 and anti-PD-1). These samples were collected through the deepMEL protocol approved by the local Ethics Committee (CER-VD) on the 25th of May 2019. All samples were metastatic lesions and lymph node samples were excluded. Response to treatment was evaluated by an independent physician radiologist and was corroborated with clinical history.

Cryopreserved and paraffin embedded tissues from the University of Pennsylvania and tissue sections from Herlev Hospital were transferred to the University Hospital of Lausanne under a material transfer agreement and studied under a local ethics committee approval by the Canton of Vaud. PBMC were collected from healthy donors at the University of Pennsylvania Human Immunology Core. Informed consent has been obtained from all subjects whose samples were used for this study.

### Cell lines and primary cultures

This study has made use of the following cell lines: OvCar5 cells (human female) expressing HLA-A2-NY-ESO-1 (obtained from Dr. M. Irving, Ludwig Institute, Lausanne branch); NY-ESO-1 CD8<sup>+</sup> TIL clone (human female, obtained from Dr. N. Rufer, Ludwig Institute, Lausanne branch); and Tp53<sup>-/-</sup>Brca1<sup>-/-</sup> ID8 ovarian cancer cells (mouse female) were obtained from Dr. Ian McNeish (Imperial College London). Tp53<sup>-/-</sup>Brca1<sup>-/-</sup> ID8 ovarian cancer cells were authenticated and transduced to express luciferase (Bruand et al., 2021). NY-ESO-1 CD8<sup>+</sup> TIL clone has been obtained by limiting dilution cloning and authenticated: clone was validated, TCR $\alpha\beta$  sequenced and tested functionally. All cell lines were negative for Mycoplasma contamination.

Cell lines, tumor cells and PBMC were maintained at 37°C in complete medium R-10: RPMI-1640 supplemented with 10% (v/v) heat-inactivated FBS, 2 mM L-glutamine, and 100  $\mu$ g/mL penicillin and 100 U/mL streptomycin.

### In vivo animal studies

This study has used C57BL/6 female mice (from Envigo, #057) housed at conventional mouse facility, and immunodeficient female NSG mice bred at the Stem Cell and Xenograft Core of the Abramson Cancer Center, University of Pennsylvania and housed in dedicated BSL-2 experimental animal barrier space equipped with whole body irradiation and all necessary procedures and survival surgeries. All mice were 6-to-8 weeks old, and kept under food and water *ad libitum* conditions. The number of animals used in each experiment was determined and justified in accordance with the protocols approved by the governing authorities. The experiments were designed to achieve the statistically significant results with the minimal use of animals.

## METHOD DETAILS

### Fresh vs. frozen usage of samples

All of the phenotypic analyses by FACS, tetramer analyses, and functional assays with peptides used fresh TIL, ascites and PBMC.

All the PDX tumors in NSG mice were developed with fresh samples, injected into NSG mice immediately after mild and short digestion. For adoptive TIL ACT transfer to HIS-NSG, we used frozen TIL for expanding tetramer-positive cells (ex. 1595 NY-ESO-1); cells were thawed for at least 1 hour in complete medium before further staining.

To characterize TIL from the OVCAR5 HIS-NSG mouse model, tumor samples were collected at approximately 50 days and digested. HER2/neu- and mesothelin-specific TIL infiltration was evaluated by tetramer staining in fresh cells. Following coculture of fresh TIL with HER2/neu or mesothelin peptide, IFN- $\gamma$  production was evaluated by ICS. Lastly, chromium release assay was performed using TIL from dissociated tumors treated with the different checkpoint blockades.

All CytoF analyses and experiments on tumor digest cocultures using PD-1 and CTLA-4 blocking antibodies and CD40 agonist or anti-PD-1 and CD28 antagonist were performed on cryopreserved samples.

In quality control experiments performed at the Penn Ovarian Cancer Research Center tumor biobank we ascertained that the immunophenotype of T<sub>EM</sub> or T<sub>EMRA</sub> and antigen-experienced TIL by FACS, as well as their reactivity to OKT3 antibody or peptide, were not altered. To ensure the quality of the material, tumors were digested gently and single-cell suspensions were cryopreserved using controlled rate freezing in 10% DMSO and FCS whole media. Cells were thawed at least one hour before analysis with complete medium and washed carefully, and we rested cultures overnight after thawing before any stimulation challenge. We used the same protocols for tumor dissociation and freezing in Lausanne.

In quality control experiments performed in Lausanne, we performed scRNAseq on a tumor sample that was analyzed either fresh or after freezing. We observed striking similarities between the cell population phenotypes in the fresh vs. the frozen tumor samples. We did detect some loss in the representation of tumor cells, which were the most sensitive population, and we detected a subtle reduction also in conventional (c)DC1, NK cells and macrophages. Nevertheless, we observed that T<sub>EM</sub> or T<sub>EMRA</sub> and antigen-experienced TIL had >70% recovery following freezing-thawing.

Proportion of cell types	Cell Type	CAFs	CD4 resting	CD8 cytotoxic	CD8 resting	CD8 terminal effector	DC1	DC2	DC3	NK cells	Naive B cells
Frozen	0.107	0.129	0.035	0.117	0.015	0.003	0.051	0.009	0.007	0.006	

Proportion of cell types	Cell Type	Endothelial	Macrophages	Memory B cells	Monocytes	MonoDC	pDC	Plasma cells	Tfh	Tgd	Tregs
Frozen	0.034	0.085	0.044	0.024	0.101	0.006	0.005	0.041	0.003	0.138	

Finally, comparing the number of genes per-cell, we found that most major cell types displayed no significant difference post freeze/thaw, although we observed a minor decrease in genes per-cell in macrophages and resting T cells, and a major drop in endothelial cells.

Average number of genes per cell	Cell Type	CD8 cytotoxic	CD8 resting	NK cells	TRegs	Tfh	CD4 resting	Memory B cells	Macrophages	MonoDC	Malignant	Endothelial	CAFs
Frozen	789	634	662	940	770	906	883	1455	2151	2424	674	1527	

Overall, the majority of the cell populations remained quite stable and preserved well their transcriptomic characteristics upon the freeze/thaw procedure with only small differences observed that could also be the result of intratumoral heterogeneity within that sample.

### Cytolytic assay with NY-ESO-1 specific TIL and ovarian cancer cell line with ectopic expression of CD80/CD86

OvCar5 cells expressing HLA-A2-NY-ESO-1 (kind gift from Dr. M. Irving, Ludwig Institute, Lausanne branch) were transduced with pMSGV vector coding for CD80 and CD86. Cells were sorted for double positive and double negative CD80/CD86 markers and treated prior to functional test with 200 ng/mL IFN $\gamma$  overnight. Effector cells were a NY-ESO-1 CD8<sup>+</sup> TIL clone (kind gift from Dr. N. Rufer, Ludwig Institute, Lausanne branch), exhausted with medium composed for 2/3 of R-10 and 1/3 for OVCAR5 conditioned medium, and supplemented with PGE<sub>2</sub> 20 ng/ml. Chromium release assay (as described above) was performed with combinations of HLA-A2<sup>+</sup>NY-ESO-1<sup>+</sup> OVCAR5 and CD80/CD86-expressing counterparts, untreated or treated with IFN $\gamma$ , with rested or exhausted NY-ESO-1-specific CD8<sup>+</sup> T cells, in the presence of single  $\alpha$ PD-1 or double  $\alpha$ PD-1/ $\alpha$ CTLA-4 treatment, as already described.

### Syngeneic model of ovarian cancer and ex-vivo functional assays

Conventional C57BL/6 mice were obtained from Envigo and housed at the pathogen-free animal facility of the Ludwig Institute in Epalinges (license 2797.1g), under approved protocols. Mice (n = 15 per group) were injected i.p. with 0.5 million *Tp53*<sup>-/-</sup>*Brca1*<sup>-/-</sup> ID8 ovarian cancer cells (a kind gift of Dr. Ian McNeish, Imperial College London (Walton et al., 2017) expressing luciferase (Bruand et al., 2021) and evaluated weekly for the luciferase signal by IVIS Lumina (Perkin Elmer). Mice were treated with 100  $\mu$ g/mouse of  $\alpha$ PD-1 (RMP1-14, BioX Cell),  $\alpha$ CTLA-4 (9D9, BioX Cell), CD40L (FGK45), or  $\alpha$ CD28 antibody (E18, BioLegend), 3 times/week for 3 weeks, except for CD40L (twice/week, 2 weeks), starting 5 days after tumor injection. At the end point, mice were euthanized, and blood and tumors were collected. Tumors were minced, dissociated and stained for CD45.2 BUV737 (104), CD83 BV711 (Michel.19), I- $\alpha$ /I-E FITC (2G9), Gr1 FITC (RB6-8C5) from BD, PD-1 BV510 (29F.1A12), PD-L1 BV785 (10F.9G2), CD80 BV421 (16-10A1), CD86 APC-A780 (GL-1), CD4 BV711 (RM4-5), F4/80 BV650 (BM8), CD11b BV605 (M1/70), Ki-67 PEDazzle (16A8), CD103 PE (2E7), CD137 APC (17B5) from BioLegend, and PD-L2 PerCP Cy5.5 (122), CD8a APCeFluo780 (53.6.7), and CD11c APC (N4/18) from ThermoFisher Scientific.

### Xenograft models of ovarian cancer

Immunodeficient NSG mice were obtained from the Stem Cell and Xenograft Core of the Abramson Cancer Center (University of Pennsylvania) and maintained under pathogen-free conditions in-house, under University of Pennsylvania Institutional Animal Care and Use Committee approved protocols. NSG mice were engrafted in intramammary location with patient's digested tumor material and followed until patient-derived xenografts (PDX) tumors reached approximately 100 mm<sup>3</sup> (about 8–12 weeks), at which point mice were injected i.v. with autologous TIL. TAA-specific TIL were sorted with multimers from autologous dissociated tumor cultures where they were incubated in the presence or absence of  $\alpha$ PD-1 Ab for 3–4 day. Sorted cells were expanded in the presence of IL-2 (300 IU/mL) for 5–7 days. 1  $\times$  10<sup>6</sup> T cells were transferred adoptively to PDX mice intravenously every 2 days for 5 times. End-point was mouse survival at 90 days after the first injection. Regressing tumors were collected from some mice to isolate RNA for TCRV $\beta$  sequencing as described above.

### Preparation of HIS-NSG mice

Immunodeficient NSG mice were reconstituted with human immune system stemming from cord blood CD34<sup>+</sup> cells harvested from HLA\*0201 donors to create a humanized mouse model (HIS-NSG). NOD-scid IL2R $\gamma$ null (NSG) female mice were reconstituted with

HLA\*0201 human cord blood precursors. After confirmation of immune reconstitution with human CD3<sup>+</sup> cells, HIS-NSG mice (n = 21 per group) were inoculated subcutaneously with  $1 \times 10^6$  HLA-A2 matched OVCAR5 cells on the flank on day 0. After tumors became palpable (4–5 weeks), 10 mg/kg anti-PD-1 (a kind gift of Dr Gordon Freedman), or 5 mg/kg of anti-CTLA-4 (ipilimumab), combination of anti-PD-1 with anti-CTLA-4 or isotype control antibodies were administered i.p. 5 times on alternate days. Tumor dimensions were measured with calipers, and tumor volumes calculated using the formula  $V = (\text{length} \times \text{width}^2)/2$ . End-point was mouse survival at 120 days after the first injection.

### Multispectral immunofluorescence (mIF) microscopy

Multispectral immunofluorescence (mIF) microscopy was performed on 4  $\mu\text{m}$  formalin-fixed paraffin-embedded (FFPE) sections from patient ovarian tumors. Slides were heated at 57°C for 2 hours and deparaffinized by immersing them in xylene, three washes 5 min each and rehydrated by immersing them to ethanol grades step. The automated Discovery ULTRA Staining Module (Ventana, Roche) with the Tyramide signal amplification (TSA) was used. The staining procedure consists of consecutive rounds of antigen retrieval, blocking, staining with primary antibody, incubation with secondary HRP-labeled antibody, TSA and antibodies denaturation, as previously described (Stack, 2014 #877). In brief, heat-induced antigen retrieval step was performed with buffer Cell Conditioning 1 (CC1, Ventana) for 32 minutes at 100°C followed by a blocking step with Protein block buffer (Dako). Then, the primary antibodies were applied at RT for 60 minutes.

The following multiplexed panels were validated and used the following: (1) PD-L1/CD68/CD11c/CD8/cytokeratins; (2) PD-1/CD8/NFATc2/GzmB/cytokeratins; and (3) PD-L1/CD11c/PD-1/CD8/cytokeratins. The following primary Ab were used: rabbit monoclonal antibody specific for CD11c (1:100, Clone EP1347Y, Abcam), CD8 (1:100, Clone SP16, ThermoFisher Scientific), PD-L1 (1:200, Clone E1L3N, Cell Signaling Technology), mouse monoclonal antibody specific for PD-1 (1:500, clone MRQ-22, BioSB), Gzm B (1:30, Clone GrB-7, Monosan), pan Cytokeratin (1:1000, Clone AE1/AE3, Dako), and CD68 (1:200, Clone PG-M1, Dako). Finally, rabbit polyclonal antibody anti-( $\alpha$ )NFATC2 (1:50, HPA008789, Sigma) has been also used in the same conditions.

Following washes, HRP-labeled polyclonal goat anti-rabbit or anti-mouse antibodies (Dako) were used for 32 minutes at RT. Next, the following TSA amplification reagents were added: TSA Fluorescein (NEL741B001KT, PerkinElmer), TSA Cyanine 5 (NEL745B001KT, PerkinElmer), TSA Cyanine 3.5 (NEL763B001KT, PerkinElmer), TSA Cyanine 5.5 (NEL766B001KT, PerkinElmer) and TSA Cyanine 3 (NEL744B001KT, PerkinElmer), at room temperature (RT) for 8 minutes. Antibody denaturation was performed by incubating sections in Cell Conditioning 1 buffer (CC1, Ventana) at 100°C for 32- and 24-minutes for CD11c and other antibodies, respectively. The sections were counterstained with DAPI (Biolegend, 1:4000) and mounted (S3023, Dako fluorescence mounting medium). A section of tonsil tissue was used as a positive control for staining.

Multiplex stained of intact FFPE-tissue slides from 74 patients were imaged using the Vectra 3.0 automated quantitative pathology imaging system (Perkin Elmer). The whole tissue slides were pre-scanned at a 10 $\times$  magnification and 20 regions were randomly selected for the acquisition of high-power (20 $\times$ ) multispectral images. Images out of focus or with folded tissue area as well as images containing normal ovarian epithelium and/or stroma were removed. An average of 10 high-resolution multispectral images per case were used for the analysis.

Melanoma cohort (Figure 7J) was imaged using similar protocol, using CD3 (1:400, polyclonal, Dako) and CD11c (1:100, Clone 5D11, Cell Marque) antibodies and applying full slide acquisition with the Vectra Polaris scanner. In Herlev cohort (Figure 2E), an average of 45 regions per sample was analyzed in representative tissue slides, representing a surface area of 16 mm<sup>2</sup> of tumor tissue on average.

### Sample selection and quality control

The 74 UPENN tumors were evaluated by multispectral immunofluorescent (mIF) microscopy for the presence of reactive CD8<sup>+</sup> TIL expressing granzyme B and nuclear NFAT in tumor stroma and islets (Figures 1A, 1B, and 1E). Most (n = 59) of these 74 tumors were also examined similarly and quantified by mIF for CD8<sup>+</sup> TIL polyfunctionality and expression of PD-1 in islets and in stroma, following the same approach (Figures 2A and 2B). Furthermore, 59 tumors were subjected to analysis of ieCD8<sup>+</sup> TIL density and CD11c<sup>+</sup> PD-L1<sup>+</sup> DC density, analyzing at least 12 regions (i.e. 20% of the tumor section surface area; Figures 3A, 3B, and 3D). Among them, we extended our studies in 18 randomly selected cases, in which we performed painstaking measurements of the distances between the two cell types, analyzing 12 to 129 regions per sample to evaluate the clustering of ieTIL with ieDC (Figure 3C). All samples from Herlev cohort were quantified extensively by mIF the density of reactive CD8<sup>+</sup> TIL (an average of 45 regions per sample was analyzed representing a surface area of 16 mm<sup>2</sup> of tumor tissue in average).

In all investigations, the examined regions were selected randomly, regions with fat, necrosis, high background and section folding were excluded from the analysis. Only regions with high quality images were retained for analysis. For the *in vitro* assays, samples were selected based on the availability of good quality frozen tissue, the presence of ieCD8<sup>+</sup> TIL, HLA-A2<sup>+</sup> status, the detection of TAA-specific TIL by tetramer, and satisfactory quality controls. Within the samples where the selection criteria were satisfied, the choice of samples was further randomized. Overall, there is a decent amount of overlap between the samples in all of the *in vitro* experiments from the UPENN cohort.

### Spectral unmixing and tissue segmentation

A spectral library containing the emitting spectral profile of all 6 fluorophores (5 TSAs + Dapi) was created with the Nuance Image Analysis software (PerkinElmer) using multispectral images obtained from single stained slides for each marker and associated fluorophore. Two ovarian cancer sections were subjected to identical slide processing without the use of TSA reagents, in order to determine the autofluorescence profile of ovarian cancer tissue. The phenotyping analysis was performed using inForm

2.1.0 image analysis software (PerkinElmer). The images were segmented into specific tissue categories of tumor islets, stroma and no tissue, based on the cytokeratin and DAPI expression, after manually drawing training regions on each image by a qualified pathologist (PGF). Individual cells were segmented using the counterstained-based cell segmentation algorithm. Following tissue and cell segmentation, scoring was performed by using manually specified threshold values for each marker and then was normalized per  $\text{mm}^2$  of tumor and stromal area following the formula  $\text{pixels} \times 0.246 \times 10^{-6} = 1\text{mm}^2$ , from the exported data.

#### **Average distance analysis**

For distance analysis, all spectrally unmixed and tissue-segmented images were subsequently subjected to an inForm active learning phenotyping algorithm, by assigning several cells to each phenotype, choosing across several images. Cells were phenotyped into different classes according to the markers of interest as follows:  $\text{CD8}^+$ ,  $\text{CD8}^+\text{PD-1}^+$ ,  $\text{CD11c}^+$ ,  $\text{PD-L1}^+\text{CD11c}^+$  and tumor (cytokeratin<sup>+</sup>). Using the script and the application `xAverageCountsBatch.R`, from Perkin Elmer, the average number of APC with “ $\text{PD-L1}^+\text{CD11c}^+$ ” phenotype within a radius of 20 microns of TIL with “ $\text{CD8}^+\text{PD-1}^+$ ” or “ $\text{CD8}^+\text{PD-1}^-$ ” phenotype were computed, within tumor and within stroma of tissue categories. The distance score was calculated by averaging the number of cells with given phenotypes within the 20 microns distance and normalizing to the number of  $\text{CD8}^+\text{PD-1}^{+/-}/\text{mm}^2$  tissue or to the  $\text{CD11c}^+\text{PD-L1}^+/\text{mm}^2$  tissue. Tissue and cell segmentation data from the Batch analysis were processed. For the quantification, for each sample, at least 10 regions (i.e.  $3.46\text{mm}^2$  representing 10–20% of the tumor section surface area) including both tumor islets and stroma were evaluated.

#### **Nuclear NFATc2 measurement**

Tumor samples were evaluated by multispectral immunofluorescent (mIF) microscopy, where NFATc2 was co-acquired along with DAPI. The latter stains nuclear chromatin and allows to delineate precisely the distribution of markers within or out of the nucleus surface. Nuclear NFAT localization was therefore inferred through colocalization with DAPI by a pathologist who manually counted the percentage of  $\text{CD8}^+$  cells in tumor and stroma with colocalized NFATc2 and DAPI in each annotated image.

#### **Laser capture microdissection**

Ovarian cancer specimens of interest were subjected to laser capture microdissection to procure pure tumor islets and adjacent stroma, according to the manufacturer's instructions using the  $\mu\text{CUT}$  Laser-MicroBeam System (SL Microtest, Jena, Germany) as previously described (Buckanovich et al., 2006; Zhang et al., 2003). Briefly, sections ( $8\ \mu\text{m}$ ) were sectioned with a cryostat, mounted on specialized slides, and fixed in 70% ethanol for 1 minute, before being quickly washed with water. After rapid hematoxylin staining, slides were dried and tumor stroma and islets delineated by a pathologist through manual circumferential marking of the islet borders on digital microscopic fields and circumferentially dissected by the automated laser beam of the LCM system. Tissue fragments were then catapulted into the lid of a 0.5 ml reaction tube containing RNA isolation buffer. RNA was isolated by Micro RNA Isolation kit (Fend et al., 1999); Stratagene, La Jolla, CA). In some experiments, RNA was isolated from microdissected tissue and subjected to real time PCR, as previously described (Buckanovich et al., 2006).

#### **Cyclic immunofluorescence in high-resolution imaging**

Whole section FFPE samples were stained with antibodies following the tissue based cyclic immunofluorescence tCycIF protocol described in Färkkilä et al. (2020) and scanned with RareCyte CyteFinder scanner (Lin et al., 2018). Scanned images were corrected using BaSiC, and stitched and registered using the ASHLAR (GitHub, 2018). Cell segmentation was performed by applying marker-controlled watershed segmentation to pixel probability maps generated with a UNet neural network (Ronneberger et al., 2015). Median fluorescence intensities were computed for each cell and each channel with HistoCAT v1.73 (Schapiro et al., 2017). Poor quality events were filtered out based on loss of signal across cycles, background signal from the initial cycle, and solidity metrics. The single-cell data matrices and cell type calls from 19 tCycIF images were used for analysis from Färkkilä et al. (2020).

Single cell data and cell type calls from 19 tCycIF images were obtained from Färkkilä et al. (2020). The cell segmentation masks were used to identify cellular neighbors within  $30\ \mu\text{m}$  (45pixels) between centers of the masks (ie, having the distance  $<30\ \mu\text{m}$  between the centers of two nuclei). The  $\text{CD8}^+\text{T}$  cells with at least one tumor neighbor were classified as intra-epithelial (ie $\text{CD8}^+$  T cells). Raw mean fluorescence intensities of the markers were  $\log_2$ -transformed for downstream analyses. The expressions of the other polyfunctional markers (x-axis) against CD45RO (y-axis) of the ie $\text{CD8}^+$  T cell of an extreme responder were plotted, and manual gates were assigned for double positive cells. The CD8 polyfunctionality score was defined as the median Z-score of the activation markers Ki-67, CD45RO, CD57, Cyclin A, pSTAT1. Statistical testing of functional marker expression for each pair of cell type A and neighbor cell type B was performed by applying a two-sided t-test (confidence level 95%) on a population of A cells, which have at least one B neighbor, against the population of cells A with no neighbors of class B. Samples with any cell population smaller than 50 cells on either of the pairs of cell types were removed from the analysis ( $n = 4$ ), and the data is presented on 15 HGSC.

For the high-resolution imaging, FFPE samples of 2 HGSC were stained with CD8a (50-0008-80, eBioscience), Cytokeratin 7 (ab209601, Abcam), CD11c (77882BC, Cell Signaling), CD11b (ab204271, Abcam), CD163 (ab218293, Abcam), pSTAT1 (8183S, Cell Signaling), Ki-67 (11882, Cell Signaling), PD-1 (43248, Cell Signaling), PD-L1 antibodies (13684, Cell Signaling), CD45RO (304212, BioLegend), CD57 (359612, BioLegend), Cyclin A (SC271682, Santa Cruz) following the tCycIF protocol. 5–10 representative fields with  $\text{CD8}^+\text{T}$ -cells were imaged from each sample. Z stacks of  $5\ \mu\text{m}$  tissue were acquired on a DeltaVision Elite (GE Life Sciences) using a  $60\times/1.42\text{NA}$  objective lens with oil matching for spherical aberration correction. Excitation channels were 632/22nm (peak emission/half-width; nominally Cy5), 542/27nm (TRITC), 475/28nm (FITC), and 390/18nm (DAPI) in that sequence on an Edge 5.5 sCMOS camera. Z stacks were deconvolved using the constrained iterative algorithm in SoftWorx, maximum intensity projected and cycles then registered with DAPI channel using MATLAB (version 2018b, The MathWorks, Inc., Natick, Massachusetts, United States).

### Choice of antigen specificity for the evaluation of ovarian cancer TIL (directed against tumor associated antigens)

We analyzed TIL specifically targeted against shared tumor antigens, in order to harmonize observations among patients. We chose tumor associated antigens (TAAs) based on previous literature supporting their involvement as tumor recognition or rejection antigens in HGSOV and other tumors. Tetramer analysis was conducted for most known shared TAAs as we have reviewed previously (Chu et al., 2008), when tetramers were available for known human leukocyte antigen (HLA) class I or II peptides. All functional experiments were conducted with HLA class I peptides, to assess CD8<sup>+</sup> TIL responses against well characterized TAAs, based on the literature. Briefly, clinical or preclinical studies of adoptive transfer of T cells directed against NY-ESO-1 (D'Angelo et al., 2018; Robbins et al., 2011) and against HER2/neu, or hTERT (Anderson et al., 2019; Hung et al., 2007; Miyazaki et al., 2013), have definitively demonstrated, for the former in clinical studies and for the other two in preclinical models, that these epitopes are *bona fide* tumor rejection antigens. Specifically, for NY-ESO-1, several clinical studies in melanoma, synovial sarcoma and multiple myeloma have demonstrated objective responses in many patients across all tumor types, without unexpected toxicities. Although these studies did not include ovarian cancer, they provided strong proof of principle. Complementary evidence came from vaccine studies, where the same antigens, or their HLA-restricted epitopes (including those used in this study), have been shown to elicit both T-cell and clinical responses; this includes also ovarian cancer patients (Chu et al., 2012; Gritzapis et al., 2006; Odunsi et al., 2007, 2012; Renard et al., 2003; Whittington et al., 2009; Yu et al., 2008). Finally, important corroborating evidence came from the study of tumor-infiltrating lymphocytes, where spontaneous specificity against TAAs and autologous tumor or tumor lines has been demonstrated in ovarian cancer and other tumors, along with expression of the target TAA (or their peptides) by the tumor (Matsuzaki et al., 2010; Redjimi et al., 2011).

### Flow cytometry

Cell suspensions from HGSOV digested tumor specimens were washed with phosphate-buffered saline supplemented with 0.1% bovine serum albumin (BSA) and 0.01% azide (FACS buffer), and stained with the following directly conjugated Abs:  $\alpha$ CD3 (UCHT1), CD4 (RPA-T4), CD8 (SK1), CD27 (M-T271), CD28 (CD28.2), CD38 (HIT2), CD45RA (HI100), CD127 (HIL-7R-M21), CCR7 (3D12), HLA-DR (G46-6), CTLA-4 (BNI3), from BD Biosciences, and PD-1 (EH12.2H7), CD137 (4B4-1), CD45 (HI30), CD28 (CD28.2), CD14 (M5E2), CD11b (ICRF44), PD-L1 (29E.2A3), HLA-I (W6/32), CD80 (2D10), CD86 (IT2.2), PD-L2 (24F.10C12) from BioLegend. CTLA-4 was evaluated by intracellular staining, after surface markers were acquired (protocol detailed in the next section). Samples were treated with GolgiStop (BD Biosciences) 4–5 hours before staining.

In some analyses, unstimulated TIL obtained directly from dissociated tumor specimens were first stained for surface markers as indicated above, and then permeabilized with a FACS permeabilization solution from BD Biosciences and incubated with  $\alpha$ -Ki-67 (B56), Bcl-2 (Bcl-2/100), T-bet (O4-46), and perforin ( $\delta$ G9), all from BD Biosciences, and granzyme B (GB12, ThermoFisher Scientific) according to the manufacturer's protocol. For TAA-specific TIL functional assay, TIL were stimulated *in vitro* for 6h (as described above) with tumor antigen-specific peptides in 96-well plates in the presence of brefeldin A (Protein Transport Inhibitor Cocktail, eBiosciences). After staining with  $\alpha$ CD3,  $\alpha$ CD8,  $\alpha$ CD4, cells were fixed and permeabilized, and stained  $\alpha$ IL-2 (5344.111),  $\alpha$ TNF $\alpha$  (6401.1111),  $\alpha$ IFN $\gamma$  (25723.11), all from BD biosciences. Positive control for T cell activation were performed with plate-bound  $\alpha$ CD3/ $\alpha$ CD28 antibodies, or PMA/ionomycin.

For tetramer staining, TIL were stained with MHC Class I or class II tetramers or unrelated control tetramers. APC-labeled MHC class I peptide tetramers specific for HER2/neu p369 (KIFGSLAFL), HER2/neu p689 (RLLQETELV), survivin (LMLGEFLKL), NY-ESO-1 (SLLMWITQC), mesothelin (VLPLTVAEV), hTERT (ILAKFLHWL), p53 (LLGRNSFEV), SP-17 (ILDSSEEDK), WT-1 (RMFPNAPYL) proteins, and class II tetramers specific for folate receptor (FR)-a 147 (RTSYTCKSNWHKGNWT), FR-a 56 (QCRPWRKNACCSTNT), hTERT E611 (EARPALLTSRLRFIPK), and NY-ESO-1 (SLLMWITQCFLPVF) were purchased from TCMetrix (Lausanne, Switzerland). After washing, cells were stained with the appropriate tetramer for 30 minutes at RT, then, without washing, surface antibodies were added for 20 minutes at 4°C. Cells were washed twice before FACS analysis. FACS analysis was carried out on LSRII-SORP (BD Biosciences), or CytoFlex LX (Beckman Coulter), and FCF file analysis was performed using FlowJo. Alternatively, for sorting, cells were stained following the same protocol using multimers (TCMetrix) and sorted using a FACSAria III (BD Biosciences).

To phenotype the myeloid compartment by FACS, cells were washed in FACS buffer and stained with  $\alpha$ -CD11b BV650 (ICRF44), CD11c A700 (Bu15), CD14 BV605 (63D3), CD80 FITC (2D10), CD83 BV421 (HB15e), CD86 APC (BU63), HLA-DR APC-Fire750 (L243), PD-L1 PerCP-Cy5.5 (10F.9G2), PD-L2 PE Cy7 (MIH18), and live/dead (Zombie Aqua), all from BioLegend.

### Time-of-flight mass cytometry (CyTOF)

#### Cell

For enzymatic digestion of solid tumors, specimen was diced into RPMI-1640, washed twice with PBS, centrifuged at 800 rpm for 5 minutes at 22°C, and resuspended in enzymatic digestion buffer (0.2 mg/mL collagenase and 30 units/mL DNase in RPMI-1640) before overnight rotation at room temperature. Dissociated tissue was then filtered through a 100  $\mu$ m nylon mesh, washed and viably cryopreserved at  $-150^{\circ}\text{C}$  in 10% DMSO (Sigma-Aldrich) and human serum (Valley Biomedical, Inc., Product #HS1017) for later use. Dissociated tumors with high red blood cell content were resuspended in ACK lysis buffer for 3 minutes and washed thrice with PBS.

#### CyTOF Staining process

Tumor samples from up to 22 ovarian cancer patient samples were thawed and rested in complete media composed of RPMI medium (Invitrogen Life Technologies) supplemented with 2 mmol/L glutamine (Mediatech, Inc.), 100 U/mL penicillin (Invitrogen Life

Technologies), 100  $\mu\text{g}/\text{mL}$  streptomycin (Invitrogen Life Technologies), 5% heat-inactivated human serum (Valley Biomedical, Inc), and 50ng/ml of IL-7 and IL-15 (PeproTech) overnight to recover. Cell identifier stain Iridium191/193 and live/dead identifier 127IdU and cisplatin 195 were obtained from Fluidigm. Dead cell stain maleimido-mono-amine-DOTA (mm-DOTA; MacroCyclics) and was kindly provided by the Wherry lab at the University of Pennsylvania. Mass cytometry antibodies were either used from Fluidigm as pre-conjugated metal tagged antibodies, or were conjugated in-house to isotope-loaded polymers using the Maxpar Antibody Labeling Kits. All antibodies were titrated to determine optimal concentrations for staining. For intracellular detection, samples were treated with GolgiStop (BD Biosciences) for 4–5 hours before staining. Single-cell sample suspensions were centrifuged and washed with Maxpar cell staining buffer (Fluidigm). For live/dead discrimination, cells were incubated with 127IdU (5-Iodo-2'-deoxyuridine) and with one of the commonly used stains – either mm-DOTA (MacroCyclics) or cisplatin 195 in PBS – for 10 minutes at room temperature. Cells were washed with staining buffer, and incubated with an antibody cocktail containing all surface antibodies for 30 min at room temperature. After incubation, cells were washed thrice in staining buffer. For intracellular detection, cells were fixed and permeabilized using the Maxpar Fixation/permeabilization buffer (Fluidigm), and incubated with intracellular staining cocktail for 1–2hrs at RT. After incubation, cells were washed thrice with 1x permeabilization buffer then fixed overnight at 4C in a 1.6% para-formaldehyde solution containing 125nM Iridium (191/193). After overnight fixation, cells were washed twice in PBS, then once in  $\text{dH}_2\text{O}$ . Data acquisition was performed on a CyTOF Helios (Fluidigm) by the CyTOF Mass Cytometer Core at the University of Pennsylvania. Bead based normalization was performed for all samples run.

### Mass cytometry biaxial, viSNE, and metaPhenoGraph analyses

Flowjo version 10 software was used to perform traditional biaxial analysis, on bead-normalized sample fcs files. Bead-based normalization was performed by the CyTOF Mass Cytometer Core at the University of Pennsylvania. To identify intact single cells, event-length and Iridium 191/193 were used. Next, live cells were identified according to 127IdU and mm-DOTA/cisplatin, where dead cells are positive for mm-DOTA/cisplatin. Positive expression of CD3 and CD45 was used to identify T-cells. Downstream gating analysis was subsequently performed for all analyzed markers. The resulting values were used to determine population frequencies. The Student's two-tailed, paired/unpaired t-test were run to determine statistical significance. Error bars are SEM.

The matlab tool *cyt* (R2015), which can be downloaded at (Pe'er, n.d.), was used to conduct high dimensional analysis such as viSNE (Amir et al., 2013) and PhenoGraph (Levine et al., 2015). viSNE, is a visualized dimensionality-reduction algorithm that uses the Barnes-Hut t-SNE (bh-SNE) implementation (Geng et al., 2015) of the t-SNE (t-Distributed Stochastic Neighbor Embedding) algorithm to map individual cells that share phenotypic similarities in a two-dimensional space. Colors are ascribed to each point that represents a cell, according to the cell's mean metal intensity (analogous to mean fluorescent intensity in flow cytometry). To create viSNE plots, singlet, live-gated  $\text{CD}3^+\text{CD}45^+\text{CD}4^+\text{CD}137^+$  and  $\text{CD}3^+\text{CD}45^+\text{CD}8^+\text{CD}137^+$  fcs data from five patients were imported into *cyt*, arcsinh5-transformed, and bh-SNE mapping was run as described by Amir et al. (2013). Next, PhenoGraph was performed, as described by Levine et al. (2015). Unlike viSNE which depicts a continuum of phenotypes, PhenoGraph partitions single-cell data into subpopulations. The Euclidean distance metric  $k = 30$ , a nearest neighbor input was used. The choice of  $k$ , ranging from  $k = 15$ –60 has been demonstrated to have virtually no effect when identifying populations (Geng et al., 2015). PhenoGraph was subsequently metaclustered, as described by Levine et al., using a  $k = 15$  as the Euclidean distance metric. Metaclustering analysis was performed as described by Levine et al., in order to better understand characteristics shared between all patient samples. All viSNE, and metaPhenoGraph plots were created using *cyt*.

Heatmap was generated using the package pheatmap (Kolde, 2019) and it shows the mean frequency of marker expression for  $\text{PD-1}^+\text{CTLA-4}^+\text{CD}137^+\text{CD}28^+$  and  $\text{PD-1}^+\text{CTLA-4}^+\text{CD}137^+\text{CD}28^-$  subsets of  $\text{CD}8^+$  TIL from up to 11 ovarian cancer patient samples.

### Tumor digest cultures and TIL stimulation

Freshly received solid tumor specimens from the operating room were diced in RPMI-1640 under sterile conditions, washed and centrifuged, resuspended in enzymatic digestion buffer (0.2 mg/ml collagenase I and IV and 30units/ml DNase, Roche, in RPMI-1640) and incubated 45 minutes at 37°C under continuous mild rotation. Cells were passed through a sieve and either cryopreserved, directly processed for FACS staining, or placed in culture with any further manipulation for functional tests. Ascites samples were washed and cryopreserved.

For tumor digest cultures, cells were adjusted to  $2 \times 10^6/\text{well}$  in 24-well plates and cultured for 3–5 days (according to the functional read-outs) at 37°C. For these experiments, tumors were chosen based on the documentation of TIL by immunofluorescent microscopy (as above), the detection of reactive  $\text{IFN}\gamma^+$  TIL at baseline or the detection of tumor associated antigen (TAA)-specific TIL by tetramer. Where indicated, cultures were supplemented with TAA-specific peptides at 1  $\mu\text{g}/\text{ml}$ : HER2/neu<sub>773-782</sub>, NY-ESO-1<sub>157-165</sub>, or hTERT<sub>324-332</sub>. All the *ex vivo* treatments with blocking antibodies were performed at 10  $\mu\text{g}/\text{ml}$ , with anti-human PD-1 (EH12-2H7, mouse IgG1, BioLegend),  $\alpha\text{PD-L1}$ ,  $\alpha\text{PD-L2}$  (kind gifts from Dr Gordon J Freeman, Dana Farber Cancer Institute) or  $\alpha\text{CTLA-4}$  (Ipilimumab; kind gift from Bristol-Myers-Squibb, Cambridge, MA), and the corresponding isotype control IgG2b or IgG1 antibodies (10  $\mu\text{g}/\text{ml}$ ). In some experiments, we used a CD40 ligand (human CD40-Ligand, Miltenyi Biotec) at a concentration of 1  $\mu\text{g}/\text{ml}$ . In some experiments, we used a peptide cocktail (PepTivator WT1, PepTivator TERT, PepTivator NY-ESO-1, each of them at 600 pmol/ $\mu\text{l}$ , all from Miltenyi Biotec) instead of TAA peptides to stimulate tumor-reactive TIL.

Following *ex vivo* culture as above on tumor digests and TIL stimulations, TIL were analyzed as detailed below. In some experiments  $\text{CD}8^+$  TIL from different conditions were sorted using HLA-A2 restricted TAA multimers (TCMetrix), which preserve high-affinity TCRs (Schmidt et al., 2011), their genomic DNAs isolated, and TCR $\beta$  CDR3 regions sequenced using Illumina Genome Analyzer as detailed below (Adaptive Biotechnologies, Seattle, USA).

### APC depletion and disruption of CD28 costimulation

In some experiments, myeloid antigen presenting cells (APC) were removed from the tumor digest cultures. Briefly, tumor was dissociated as above. A small aliquot of dissociated tumor material was used to phenotype APC by FACS as described above. Following the staining, myeloid cells were removed by positive magnetic selection with CD11b PE (D12), CD11c PE (S-HCL-3, both from BD Biosciences), CD14 PE (HCD14) and CD68 PE (Y1/B2A, both from BioLegend), followed by anti-PE magnetic beads (Miltenyi). Residual cells were stained with carboxy-fluorescein diacetate succinimidyl ester (CFSE, ThermoFischer Scientific) to later assess TIL proliferation (see below). Cultures were then either resupplied with the same amount of APC or left APC-free. Cultures were treated with PD-1, CTLA-4, control Ab as above, or predicted CD28 antagonist peptide p2TA (1  $\mu\text{g}/\text{ml}$ ) or p2TA scramble, synthesized at the Protein and Peptide Chemistry Facility of the University of Lausanne. After 3-4 days in culture, CD8 cells were analyzed by FACS to assess CFSE dilution, as described above.

### p2TA (AB103) peptide hypothetical mechanism of action

p2TA is an 8-amino-acid (SPMLVAYD; CD288–15) immunomodulating peptide, which is a mimetic of the second CD28 domain that partakes in the CD28 dimer interface, as predicted from alignment of the CD28 dimer with CTLA-4 dimers (Arad et al., 2011). In the available structure for CD28, p2TA overlaps with the dimer interface (Arad et al., 2011). P2TA thus binds to a CD28 molecule at the dimerization domain, thus disrupting the CD28 homodimer. We developed an *in silico* solution of these interactions, developed based on the published CTLA-4/CD86 dimerization complex resolution structure (Schwartz et al., 2001).

Activation of CD28 signaling in T cells requires CD28 dimerization and likely oligomerization (Greene et al., 1996; Sørensen et al., 2004). Furthermore, physiologically CD28 dimerization is triggered by TCR engagement through inside-out signaling, and is at the base of increased CD28 valency, enhanced avidity for its ligands, and CD28 signaling (Sanchez-Lockhart et al., 2014). Indeed, molecular dynamic simulations and site directed mutagenesis experiments have unveiled a model whereby inside-out signaling from the TCR can induce a change in the CD28 dimer interface, which allows for bivalent ligand binding. This ultimately strengthens CD28 ligand interactions and the transduction of CD28 costimulatory signals that are physiologically required for T cell activation (Sanchez-Lockhart et al., 2014).

Thus, disrupting of the CD28 dimerization by p2TA attenuates CD28 signaling. In fact, at the base of CD28 signaling could be a process of oligomerization upon engagement of CD86, which also dimerizes, as CD28 dimers. Assembling with CD86 dimers could be expected to oligomerize as a ‘skewed zipper’, thus reinforcing CD28 signaling. Dimerization of CD28 is disrupted by the CD28 mimetic antagonist p2TA. Although in this state CD28 monomers can bind to CD86, lack of dimerization of CD28 leads to disruption of the skewed zipper, likely to attenuate CD28 signaling, as oligomerization is required for proper CD28 signaling (Greene et al., 1996; Sørensen et al., 2004). Thus, p2TA allosterically attenuates CD28 signaling (Kaempfer et al., 2017; Levy et al., 2016) without directly interfering with CD28 binding to CD86 (Shirvan et al., 2018).

Although p2TA is a mimetic of the CD28 homodimer interface domain and although it binds superantigens and efficiently disrupts their binding to CD28 (at the homodimer interface domain), there is no experimental evidence that it binds to CD28 itself. To increase our level of confidence regarding this specific issue, we performed additional *in silico* analyses with molecular modelling. Using the CD28 homodimer coordinates obtained from the recent structure of CD28 in complex with the anti-CD28xCD3 CODV Fab Light chain (PDB ID 6O8D) (Wu et al., 2020a), we applied the FoldX program (Schymkowitz et al., 2005) to estimate quantitatively the contribution of each residue of CD28 to the formation of the CD28 homodimer. The following table lists all residues providing a favorable contribution to the dimerization free energy,  $\Delta G_{\text{bind}}$ , of at least  $-0.10$  kcal/mol. Of note, among the 114 residues of each CD28 monomer present in the experimental structure, only the 13 residues reported in the Table below are predicted by FoldX to make a noticeable contribution to the homodimerization. Importantly, four residues among the top 10 contributors to the homodimerization belong to CD28<sub>8-15</sub> (i.e. to p2TA). They are displayed in bold in the table below. These results suggest that residues CD28<sub>8-15</sub> make an important contribution to CD28 homodimerization, supporting the hypothesis that p2TA can bind CD28 at the dimerization interface.

CD28 Residue	Residue contribution to $\Delta G_{\text{bind}}$ (in kcal/mol)
Ile114	-1.96
His116	-1.88
Thr89	-1.61
Ile91	-1.08
<b>Leu11</b>	-0.50
<b>Pro9</b>	-0.49
Asp90	-0.39
Lys39	-0.31
<b>Met10</b>	-0.24
<b>Val12</b>	-0.21
Lys6	-0.20
Val86	-0.14
Lys109	-0.13

### Functional analysis of fresh TIL or TIL from tumor digest cultures

For proliferation assays, digested ovarian tumors were labeled with 1  $\mu$ M CFSE (ThermoFischer Scientific) in PBS for 7 min at 37°C. Following incubation, cold fetal calf serum was added for 10 minutes at room temperature (RT), and cells were washed thoroughly with complete RPMI-1640 medium, before plating them as described above. After 3–5 days in culture in the presence of TAA-specific peptides and/or  $\alpha$ PD-1,  $\alpha$ CTLA-4, or isotype control, cells were harvested and CFSE dilution was measured by FACS.

For chromium release assay, briefly, we used autologous tumor cell lines (expressing NY-ESO-1), T2 pulsed (with NY-ESO-1 or unrelated peptide, and unpulsed cells), or compatible NY-ESO-1<sup>-</sup> cells as target cells, and NY-ESO-1-specific TIL as effector cells. Target cells were labeled with 100  $\mu$ Ci <sup>51</sup>Cr at 37°C for 1.5 hours. Target cells were dispensed in 96-well plate in the presence of effector cells at different ratios (E:T ratio 1:1, 2.5:1, 5:1). After 5h of incubation at 37°C, the supernatants were harvested, transferred to a luma-plate (Perkin-Elmer) and radiation was counted using a TopCount NXT Scintillation Counter (Perkin-Elmer). Spontaneous <sup>51</sup>Cr release was evaluated in target cells incubated with medium alone. Maximal <sup>51</sup>Cr release was measured in target cells incubated with 0.1N HCl. Percent of specific lysis was calculated as (experimental - spontaneous lysis/maximal - spontaneous lysis)  $\times$  100.

In some experiments, after 3 to 4 days in culture with the corresponding treatment, culture supernatants were analyzed by cytokine bead array (CBA) for granzyme A and granzyme B, and by enhanced CBA for IL-2, IFN $\gamma$  and TNF $\alpha$  (all from BD Biosciences). Cytokines concentration (ng/mL) was normalized to 10,000 live cells. Effect of each treatment was calculated as fold-change increase for each parameter relative to the untreated condition. Parameters that showed a fold-change increase > 1.2 were considered as positive. TIL that showed proliferation together with at least two more functions after each treatment were considered as responsive to the treatment.

In Herlev cohort, Tumor reactivity was evaluated *ex vivo* using bulk TIL that were expanded with high dose IL-2 from the same tumors. TIL were incubated with autologous tumor cell line or tumor-digests as available (Westergaard et al., 2019). Tumor specificity was measured by IFN $\gamma$  and confirmed by abrogating it via HLA blocking antibodies.

### Kinetic of expression of CD28 and phosphorylated ERK

HGSOC tumor specimen (n = 10–22) were dissociated and aliquoted in FACS V tubes with R-10 supplemented with  $\alpha$ PD-1 antibody, in the presence or absence of p2TA peptide (as described above). After a quick spin, tubes were incubated in thermal bath at 37°C for 30, 45 and 60 minutes. At each time point, cells were immediately fixed with paraformaldehyde (PFA, Sigma-Aldrich) for 15 minutes at RT, then washed and permeabilized with 1 mL Permeabilization buffer III (BD Biosciences), for 30 minutes on ice. After 2 washes with FACS buffer and Fc blocking, cells were stained with phosphor-ERK-specific antibodies (20A, BD Biosciences) for 1h at RT. After washing, cells were stained for phenotype markers CD45, CD3, CD8, CD28 (antibodies as reported above), and analyzed by FACS (Gallios, Beckman Coulter).

### TCR sequencing and analysis

Genomic DNA from microdissected stroma and adjacent islets, from sorted T cells from the same tumors (as described above), or from patient derived xenograft tumors grown in NSG mouse and treated with autologous TIL (see below) were isolated using DNeasy kit from Qiagen according to manufacturer instructions. TCR sequencing was performed by Adaptive Biotechnology and TCRV $\beta$  sequences were further processed using *ad hoc* Perl scripts to: (i) pool all the TCR sequences coding for the same protein sequence; (ii) filter out out-frame sequences; (iii) determine the abundance of each distinct TCR sequence. To evaluate the clonally expanded TCRs we calculated the median frequency of all the TCRs' populations. A TCR was considered as clonally expanded if its own frequency exceeded 5 times the median. To reduce bias introduced by culture heterogeneity in the  $\alpha$ CTLA-4/ $\alpha$ PD-1 experiment, only the clonotypes present in each culture condition were considered to evaluate the impact of  $\alpha$ CTLA-4 and  $\alpha$ PD-1 on TCR proliferation.

### Single cell (sc)RNAseq

#### Isolation of TIL from tumor digest cultures

Cells from tumor digested specimens were adjusted to 2  $\times$  10<sup>6</sup>/well in 24-well plates and cultured overnight with WT1, hTERT and NY-ESO-1 PepTivator (by Miltenyi). The next day, the cells were collected and washed in wash solution prepared with 0.09% NaCl solution (Bichsel AG), with Fish Gelatin 1% (Sigma Aldrich) and RNasin 0.1% (Promega). After wash, the cells were resuspended in wash solution in the presence of human Fc Block (Miltenyi Biotech), 50nM Calcein AM (ThermoFisher) and Zombie UV Fixable Viability Kit (BioLegend). After incubation, cells were stained in wash solution in the presence of CD45 PerCP Cy5.5 (clone 2D1), CD3 BV711 (clone UCHT1), and CD8 BV650 (clone SK1) (all the Abs are from BioLegend). Cells belonging to the same tumor specimen were pooled together and sorted on a MoFlo Astrios (Beckman Coulter). Sorted cells were collected in 0.2mL PCR tubes with 10  $\mu$ L PBS with 0.4% BSA (Sigma Aldrich) and RNasin 0.1%. Live cells were gated as Calcein AM positive and Zombie UV negative and further gated for CD45+CD3+CD8+ markers. Collected cells were then immediately encapsulated using 10 $\times$  protocol.

#### Encapsulation and library construction

Single-cell RNA libraries were generated using the 10x Chromium Single Cell 5' Gel beads and Library kit, according to the manufacturer's instructions (10X Genomics). Briefly, after FACS sorting, cells were manually counted with hemacytometer and viability was also checked using Trypan blue exclusion. For each sample, 1,000–10,000 cells were loaded into the Chromium machine with the aimed recovery of 600–8,000 cells. Single cells were encapsulated into droplets with reagents and gel bead containing a unique molecular identifier (UMI). cDNAs obtained after droplets break were purified with Dynabeads MyOne SILANE and amplified by 16 cycles of PCR (98°C for 45 s; [98°C for 20 s, 67°C for 30 s, 72°C for 1 min]  $\times$  16; 72°C for 1 min). Resulting amplified cDNAs were used for both

5' Gene Expression Library construction and V(D)J enriched libraries (TCR enrichment). Quantification of the resulting libraries was performed with the Qubit HS dsDNA assay kit and quality control was performed with the Fragment Analyzer (Agilent).

#### Sequencing and pre-processing of scRNAseq profiles

The V(D)J + 5' Gene Expression libraries were sequenced using Illumina HiSeq 4000 targeting the recommended by 10x Genomics read length and depth (for the 5' Gene Expression Library, Read 1: 26 cycles, i7 index: 8 cycles, i5 index: 0 cycles, Read 2: 98 cycles and a sequencing depth of 25 000 read pairs per cell; for the V(D)J enriched libraries, Read 1: 150 cycles, i7 index: 8 cycles, i5 index: 0 cycles, Read 2: 150 cycles a sequencing depth of 5000 read pairs per cell).

The fastq files were generated and demultiplexed either by cellranger mkfastq from 10x Genomics (version 3.0.2) or by BaseCalling in Illumina RTA 1.18.66.3 and post processed via Illumina pipeline 2.19.1. The quality control of sequencing was confirmed by FastQC software (Andrews, 2010). Alignment, filtering, barcode and UMI counting was performed using GRCh38-3.1.0 reference genome and cellranger count from 10x Genomics, version 3.1.0. Multiple gene expression libraries were combined and normalized to the same sequencing depth (post-normalization mean reads per cell 28,950) using cellranger aggr. Two libraries were excluded from normalization step and were added to the analysis using their total reads per cell of 18,600 and 2,100, respectively. For all of the downstream analysis, filtered feature-barcode matrix containing gene expression data for only detected cellular barcodes was used. The single-cell V(D)J sequences and annotations were generated using cellranger vdj and vdj\_GRCh38\_alts\_ensembl-3.1.0 reference genome. On average, 64.3% of reads were mapped to any V(D)J gene and only full length and productive TCRs (79.1% of total mapped) were considered for the analysis.

#### Analysis of the scRNAseq data

The downstream analysis was performed using Seurat (version 3.1.0; (Butler et al., 2018; Stuart et al., 2019) package in R language for statistical computing (R Core Team, 2020). Starting from the initial 44,718 cells, we filtered out potential doublets and debris by keeping only the cells with the number of genes between 300 and 5000 and whose UMI count ranged between 500 and 8000. By the same reasoning, we subsetted to the cells with mitochondrial content less than 15% and ribosomal content between 15% and 50%. This reduced the total number of cells by 15%. We then further filtered the remaining 37,658 cells to CD8<sup>+</sup> population based on the expression of the known markers. Namely, cells had to have positive expression (> 0) of *CD8A* and/or *CD8B*, and to have minimal expression (< 1) of the non-T-cell markers – *SLAMF7*, *PECAM1*, *KLRC3*, *KLRC1*, *TYROBP*, *CD4*, *SPI1*, *VWF*, *FCER1G*, *FOXP3*, *CD19*, *CD79A*, *IGKC*, *FCGR2A*, *CSF1R*, *FLT3*, *CLEC4C*, *COL1A2*, *MCAM*, *MYLK*, *FAP*, *PDPN*, *EPCAM*, *TP63*. This further reduced the number of cells by 39% to a total of 22,963.

Next, for each individual TME library, variable genes from the log-normalized counts were found using vst method and then the libraries were integrated using the anchoring technique described in Stuart et al. (2019), with dimensionality of 10 and with 700 anchors. Integrated data was scaled and passed to the principal component analysis, PCA. The first 10 principal components were used to calculate t-Distributed Stochastic Neighbor Embedding, t-SNE, (with the perplexity of 30) and to find shared nearest neighbors, SNN, (k = 30) for identifying clusters (with resolution = 0.3). In the clonal expansion analysis, 91.6% of cells were annotated with the known TCR sequence. Since bigger number of reads was assigned to TRB (58%) as compared to TRA (42%), only the beta chain receptors were analyzed in the downstream analysis. PCA, t-SNE and clustering of the clonally expanded cell subset and was performed as described above.

For differential expression analysis, genes were identified using a hurdle model tailored to scRNA-seq data (MAST method). Only genes showing a minimum of 0.1 difference in the fraction of detection between the groups were tested. Differentially expressed genes between TIL in high exhaustion/high CD28-costimulation state and TIL in high exhaustion/low CD28-costimulation for all CD8<sup>+</sup> T cells and for clonally expanded CD8<sup>+</sup> T cells ( $\geq 10$  cells/TCR) are provided in Tables S3 and S4, respectively.

Finally, the signature scores were calculated for each cell using the AUC metric, which represents the fraction of genes within the top of the ranked list that is observed in the signature.

The images were produced either by the built-in functions from Seurat package or by ggplot2 (Wickham, 2016) and pheatmap (Kolde, 2019) packages.

The raw and processed single cell sequencing data can be accessed at the GEO database: GSE178245.

#### Regulon activity analysis

Regulons were inferred using the SCENIC pipeline, which integrates three algorithms: grnBoost2, RcisTarget and AUCell (Aibar et al., 2017). First, gene regulatory network (GRN) was inferred using grnBoost2 (a faster implementation of the original Genie3 algorithm) (Huynh-Thu et al., 2010) and scRNA-seq transcriptomics data as an input. The prediction of the regulatory network between  $n$  given genes was split into  $n$  different regression problems and expression of a given target gene was predicted from the expression patterns of all the transcription factors using tree-based ensemble methods, Random Forests or Extra-Trees. The importance of each transcription factor in the prediction of the target gene expression pattern was taken as an indication of a putative regulatory event which was then aggregated over all genes to provide, for each target gene, a ranking of incoming regulatory interactions from which the whole network was reconstructed. Next, co-expression modules (raw putative regulons, i.e. sets of genes regulated by the same transcription factor) were refined by pruning indirect targets using transcription factor motif analysis: for a given transcription factor, only targets with transcription factor binding sites compatible with the DNA-binding domain of the transcription factor were retained. As the input for each transcription factor, this step took a list of the top targets (with the strongest regulation according to the GRN) and a cis-regulatory motif database (Herrmann et al., 2012; Imrichová et al., 2015). The motif database includes a score for each pair motif-gene, so that a motif-gene ranking can be derived. A motif enrichment score was then calculated for the list of transcription factor selected targets by calculating the Area Under the recovery Curve (AUC) on the motif-gene ranking (Aibar et al., 2017) using

the RcisTarget R package. If a motif was enriched among the list of transcription factor targets, a regulon was derived including the target genes with a high motif-gene score. Finally, AUCell was used to quantify the regulon activity in each individual cell.

### Gene signatures

The exact genes for all signatures are provided in [Table S2](#).

Exhaustion signature was derived by a careful curation of the observed markers in human CD8<sup>+</sup> T cells ([van der Leun et al., 2020](#)). It is worth noting that since cells in exhausted state are normally former activated cells, exhaustion signatures reported in the literature are often highly overlapping with the activation signatures. The two states are deeply intertwined and it is hard to decouple them. However, while many of the CD8<sup>+</sup> cells analyzed by scRNAseq shared important characteristics with the cytolytic, activated, and cytotoxic states, only the cells with high scores of our curated exhaustion signature displayed dysfunctional ([Jerby-Arnon et al., 2018](#)) and terminal differentiation ([Azizi et al., 2018](#)) phenotypes.

Costimulation by the CD28 family (or CD28-costimulation signature) was taken from the REACTOME database ([Garapati, 2008](#)). CD137<sup>+</sup> coexpression, PD1R, and MegaClust myeloid signatures were derived as described in the text. The T cells and APC (iDC) signatures in [Figures 5B, S6C, S7E, and S7K](#) were compiled based on the signatures reported by [Bindea et al. \(2013\)](#).

### Survival and gene expression analyses

Survival analyses were performed using the curatedOvarianData R package ([Ganzfried et al., 2013](#)), a collection of different available datasets, which collected data and eliminated duplicates from 16 sources. To improve commensurability across all samples we performed sample-wise centering and gene-wise centering and rescaling to unit standard deviation in each of the 16 studies. We obtained 1,476 cases selected to have patient survival available with positive survival times and expression data for the *CD8A* and *GZMB* genes (corresponding to 10 datasets out of 16 identified as follows: E-MTAB-386, GSE13876, GSE17260, GSE18520, GSE26193, GSE30161, GSE32062, GSE49997, GSE9891, TCGA-RNASeqV2). Of note, the analyses involving *PDCD1* and *CD274* were performed by removing the E-MTAB-386 dataset due to lack of expression data, which resulted in a final cohort size of 1,348 patients. Survival analyses were done on overall survival by Cox regression analysis after a right-censoring of 5 years. Gene expression was either categorized using a cutoff of 0.8 or used as signature computed as the average expression of the genes involved.

Gene expression correlation and molecular subtype analyses were performed on TCGA RNA sequencing data obtained from the GDAC firehose platform ([Broad Institute of MIT and Harvard, 2016](#)). RSEM gene expression values were log2 transformed after the sum with a pseudo-count of 1. We extracted the genes specific for Tothill et al. molecular subtypes ([Tothill et al., 2008](#)), together with their coefficient and selected the 100 most upregulated and 100 most downregulated for each subtype. In TCGA data, we then subtracted the average expression of the 100 upregulated by the average expression of the 100 downregulated genes, which generated a score for each patient and each subtype. These scores were interquartile range normalized and patients were classified according to the subtype with highest score. Early stages subtypes (C3 and C6) were removed from the analysis, keeping only mesenchymal (C1), immunoreactive (C2), differentiated (C4) and proliferative (C5). Statistical significance was computed by ANOVA followed by post-hoc Tukey test for multiple testing adjustment.

### Public gene expression data correlation with response to $\alpha$ PD-1 treatment

To understand what are the transcriptomics features of response to  $\alpha$ PD-1 treatment, we underwent differential expression analyses in public cancer cohorts with both gene expression profiling and clinical response to  $\alpha$ PD-1 treatment (see table below).

Dataset	Publication	Cancer Type	Drug	Previous $\alpha$ CTLA-4	Sample Number	GEX Platform	Accession #
1	<a href="#">Prat et al. (2017)</a>	HNSCC; NSCLC; Mel	Pembro & Nivo	yes for some Mel	65	Nanostring Pancancer	GSE93157
2	<a href="#">Hugo et al. (2016)</a>	Mel	Pembro & Nivo	no	28	RNAseq	GSE78220
3	<a href="#">Lee et al. (2018)</a>	Mesothelioma	Nivo	no	10	BeadChip	GSE99070
4	<a href="#">Ascierto et al. (2017)</a>	Mel	Nivo	no	1 (10 mets)	Microarray	GSE79691
5	<a href="#">Roh et al. (2017)</a>	Mel	Pembro	yes	54	Nanostring Custom	Supplementary table
6	<a href="#">Chen et al. (2016)</a>	Mel	Pembro	yes	53	Nanostring Custom	Supplementary table

We then performed differential gene expression analyses between  $\alpha$ PD-1 non-responders (PD: progressive disease) and  $\alpha$ PD-1 responders (union of SD (stable disease), PR (partial response) and CR (complete response)) in individual cohort and also in a merge cohort using the *limFit* function of the *limma* R package. Samples taken from biopsies during or after  $\alpha$ PD-1 therapies were removed from the analysis (only from the cohort of [Chen et al. \(2016\)](#)). The merged dataset comprises 332 genes and 179 patients (95 responders to  $\alpha$ PD-1, 84 non-responders). For the differential gene expression analysis of the merge cohort and those with multiple

cancer types, both cancer type origin and cohort (only for the merged analysis) were included as covariates. Enrichment plots for every gene signature and cohort were performed using the *barcodeplot* function of the *limma* R package.

Correlation between objective response rate to  $\alpha$ PD-1/ $\alpha$ PD-L1 as reported by Yarchoan et al. (2017) and CD28-costimulation, PD1R, or MegaClust myeloid signatures levels in the pan-cancer TCGA dataset (taken from the official pan-cancer atlas repository (<https://gdc.cancer.gov/about-data/publications/pancanatlas>)) was performed followed by univariate and multivariate analysis. Enrichment analysis of signatures in melanoma samples before neoadjuvant  $\alpha$ PD-1 treatment (Huang et al., 2019) was performed using GSVA package (Hänzelmann et al., 2013) and a single sample GSEA method.

### MegaClust analysis

FACS results from 28 parameters were collected in two separate panels (myeloid and lymphoid) for 12 different patients, selecting tumors with TIL responding in culture to at least single  $\alpha$ PD-1 ( $n = 2$ ), or to triple  $\alpha$ PD-1/ $\alpha$ CTLA-4/CD40L treatment ( $n = 5$ ), or no treatment ( $n = 5$ ). The resulting 26 files were preprocessed as follows: first, each file was compensated using its own compensation matrix. After this, the default bi-exponential transformation “estimateLogicle” from the “flowCore” library, was applied. The resulting dataset was then filtered to remove outliers, aggregates, and debris.

Four main gates were applied to all the data. The first gate was a rectangular that used the channels “FSC-H” and “SSC-A”. To define a rectangular, the lower-left point (30000, 0) and the upper-right point ( $2.5 \times 10^5$ ,  $2.5 \times 10^5$ ) were used. These values have been estimated to remove the majority of the debris (objects with an FSC-H smaller than 30000) and the aggregate (objects with an FSC-H larger than  $2.5 \times 10^5$ ). The second gate used the channels “FSC-A” and “FSC-H” with a rectangular at (0,0) and ( $2.5 \times 10^5$ ,  $2.5 \times 10^5$ ). These two channels were also used to identify the singles, though during an early inspection of these graphs, aggregates on the right end were found. The third gate selected the singlets with the function “singleGate” from the package “flowStats”. This gate (with the parameters `maxit = 50` and `wider gate = TRUE`) worked on the channels “FSC-A” and “FSC-H” and automatically identified the singlets population. Finally, a polygonal gate, based on the channels “Id” and “SSC-A”, was applied to all the data to select the live cells. Such a gate was estimated to remove as much as possible dead cells but still to be large enough to not remove live cells that present a high “Id” signal.

After gating, 25,000 events (cells) were randomly sampled from each sample, as the input for MegaClust (Faget et al., 2017) should be balanced in number of points coming from the different samples. For the lymphoid panel, the following channels were used: CD4, CD8, CD3, ICOS, CD28, OX40, CD103. In the myeloid panel, three different markers (CD19, CD53, and CD3) have been recorded on the same channel (labeled in figures as CD19/CD53/CD3) and for the clustering the following channels were used: “CD19/CD53/CD3”, “CD45”, “CD14”, “CD11b”, “HLADR”, “CD80”, “CD86”, “CD40”.

The output of MegaClust was summarized in a heatmap (see Figures 8B and S8C) showing the median fluorescence intensity (MFI) for a specific group of cells falling in a specific cluster for each channel (Nowicka et al., 2017). In addition, we could interrogate the results of MegaClust to extract the relative frequency of cells for each cluster for each sample (see Figure S8C). These frequencies were further analyzed with the Orthogonal Projections to Latent Structures Discriminant Analysis (OPLS-DA).

The discriminant analysis was carried out by Orthogonal Projections to Latent Structures Discriminant Analysis (OPLS-DA), and, more specifically, the implementation of the *ropls* R package (Thévenot et al., 2015). The OPLS-DA took as the input the matrix of relative frequency of cells for each cluster and sample out of the MegaClust analysis. The data was preprocessed by mean-centering and unit variance scaling. The relative importance of each cluster or responsiveness discriminant score coincide with the  $\text{vip}_n$  value or VIP (Variable Importance for Prediction) (Galindo-Prieto et al., 2014).

### Graphical illustrations

Graphical illustrations were created with the help of Smart Servier Medical Art (<https://smart.servier.com>).

## QUANTIFICATION AND STATISTICAL ANALYSES

Comparison between groups ( $p$ -value) was calculated using Wilcoxon’s  $t$ -test,  $t$ -test, two-proportions  $z$ -test unless otherwise stated in the text. Survival was analyzed using Log-rank test, and correlation was evaluated by Spearman test or Pearson. All statistical analyses were performed with GraphPad Prism or R language for statistical computing.